



## 저작자표시-비영리-변경금지 2.0 대한민국

이용자는 아래의 조건을 따르는 경우에 한하여 자유롭게

- 이 저작물을 복제, 배포, 전송, 전시, 공연 및 방송할 수 있습니다.

다음과 같은 조건을 따라야 합니다:



저작자표시. 귀하는 원저작자를 표시하여야 합니다.



비영리. 귀하는 이 저작물을 영리 목적으로 이용할 수 없습니다.



변경금지. 귀하는 이 저작물을 개작, 변형 또는 가공할 수 없습니다.

- 귀하는, 이 저작물의 재이용이나 배포의 경우, 이 저작물에 적용된 이용허락조건을 명확하게 나타내어야 합니다.
- 저작권자로부터 별도의 허가를 받으면 이러한 조건들은 적용되지 않습니다.

저작권법에 따른 이용자의 권리는 위의 내용에 의하여 영향을 받지 않습니다.

이것은 [이용허락규약\(Legal Code\)](#)을 이해하기 쉽게 요약한 것입니다.

[Disclaimer](#)



Ph.D. Dissertation of Engineering in Material Science  
and Engineering

# Overcoming the Lifetime Limitations of Metal Halide Perovskite Light-Emitting Diodes

금속 할라이드 페로브스카이트 발광 다이오드의  
수명 한계 극복

February 2023

Graduate School of Engineering  
Seoul National University  
Material Science and Engineering

Joo Sung Kim



# Overcoming the Lifetime Limitations of Metal Halide Perovskite Light-Emitting Diodes

Advisor: Tae-Woo Lee

Submitting a Ph.D. Dissertation of Engineering

December 2022

Graduate School of Engineering  
Seoul National University  
Material Science and Engineering

Joo Sung Kim

Confirming the Ph.D. Dissertation written by

Joo Sung Kim

December 2022

Chair	<u>Byungwoo Park</u>	(Seal)
Vice Chair	<u>Tae-Woo Lee</u>	(Seal)
Examiner	<u>Jin Young Kim</u>	(Seal)
Examiner	<u>Jaesang Lee</u>	(Seal)
Examiner	<u>Himchan Cho</u>	(Seal)



# Abstract

## Overcoming the Lifetime Limitations of Metal Halide Perovskite Light-Emitting Diodes

Joo Sung Kim

Department of Materials Science and Engineering

The Graduate School

Seoul National University

Metal halide perovskites (MHPs) have been studied as promising candidates for light emitters because of their narrow emission spectra (full-width at half-maximum  $\approx 20$  nm), easy color tunability, excellent charge-transport properties and low-cost solution processability. As such, they are promising candidates for use in next generation light-emitting diode (LED) displays that could overcome the color quality limitations of current commercial LEDs made with organic materials. Perovskite LEDs (PeLEDs) have been developed containing films of MHPs in the form of relatively large polycrystalline grains or colloidal nanocrystals. However, PeLEDs suffers from very short lifetime of less than several tens of hours and unstable device behavior due to the soft ionic crystal structure. MHPs are fundamentally easily degraded by heat, moisture, and electric field during the device operation. Due to the intrinsic limitation on stability, PeLEDs has been considered



only the laboratory-scale material that cannot be commercialized. In this research, strategies to overcome the lifetime limitations of PeLEDs were developed.

In chapter 2, 3D-2D core/shell structures of perovskite light emitters using stable 2D perovskite structures were developed. By facilitating the proton transfer reaction in the perovskite precursor solution, a stable two-dimensional perovskite structure is synthesized, and by forming a mixed structure surrounding the three-dimensional perovskite in the crystallization step, the three-dimensional perovskite Defects located on the surface of the crystal could be suppressed. Existing three-dimensional perovskite structures have disadvantages in that they exhibit low luminous efficiency due to charge loss occurring at defects on the crystal surface and very low stability due to ion migration occurring at defects. This limitation was solved by stabilizing the surface with a two-dimensional perovskite structure, so that a perovskite light emitting diode with higher luminous efficiency and excellent drive lifespan could be realized. In addition, it was proved that the cause of the unstable electrical behavior of the device when driving the light emitting diode was due to ion movement.

In chapter 3, in situ synthesis of core/shell perovskite nanocrystal are introduced. Previously reported 3-dimensional and colloiddally synthesized nanoparticle perovskite structures had limitations in that they can't simultaneously satisfy high charge mobility and strong charge confinement. In this study, post-treatment process of short acidic ligand was introduced on the surface of a 3-dimensional polycrystalline perovskite thin film, resulting in a core/shell structure surrounded by short ligands while large crystals were split by ligands to form nanoparticles. This in situ core/shell structure not only maintained the high charge



mobility of the 3-dimensional structure, but also exhibited efficient light emission characteristics with strong charge confinement effects of nanocrystals. As a result, when fabricated as a perovskite light emitting diodes, an excellent device characteristics with maximum luminance of more than 400,000 nits, maximum external quantum efficiency of 28.9%, and estimated operational lifetime of more than 30,000 hours at 100 nits of luminance were achieved.

In chapter 4, the effect of ionic movement on the catastrophic failure phenomenon in operational lifetime decay process of perovskite light emitting devices and the underlying degradation mechanism were studied. Using the stable core/shell nanocrystal perovskite and 3-dimensional polycrystalline perovskite-based light emitting diodes discussed in Chapter 3, we comprehensively analyzed the electrical, optical, and chemical characteristics of each degradation stage to unravel the cause of catastrophic failure. In particular, the existence of a unique degradation mechanism accelerated by the positive feedback of ion diffusion toward electrode, corrosion of metal electrode by ion, increase in driving voltage, and subsequent Joule heating was identified.

**Keyword :** Metal halide perovskite, light-emitting diode, core/shell structure, ion migration, stability, degradation mechanism

**Student Number :** 2017-27320



# Table of Contents

Abstract.....	i
Table of Contents .....	iv
List of Tables.....	vi
List of Figures .....	vii
Chapter 1. Introduction .....	1
1–1. Megatrend of display .....	1
1–2. Challenges for realizing stable perovskite LEDs.....	5
1–3. Outline of the thesis.....	8
Chapter 2. Proton–Transfer–Induced 3D/2D Hybrid Core/Shell Perovskite LEDs with Suppressed Ion Migration and Luminance Overshoot.....	9
2–1. Introduction .....	9
2–2. Experimental .....	12
2–3. Result and discussion.....	17
2–4. Conclusion.....	64



Chapter 3. <i>In situ</i> Formed Core/Shell Perovskites for Simultaneously Ultra-Bright, Efficient, and Stable Perovskite LEDs .....	65
3-1. Introduction .....	65
3-2. Experimental .....	68
3-3. Result and discussion.....	73
3-4. Conclusion.....	105
Chapter 4. Unravelling the Origin of Catastrophic Failure in Perovskite LEDs.....	106
4-1. Introduction .....	106
4-2. Experimental .....	110
4-3. Result and discussion.....	114
4-4. Conclusion.....	133
Chapter 5. Conclusion .....	134
Bibliography .....	137
Abstract in Korean.....	146
Curriculum Vitae.....	149
Acknowledgement .....	163



# List of Tables

<b>Table 2.1</b> Bi-exponential decay function, $y = A_1e^{-t/\tau^1} + A_2e^{-t/\tau^2}$ fitted results of PL lifetime curves of pristine, 2.4 mol% ANI-added, and 2.4 mol% BnA-added MAPbBr <sub>3</sub> films on Quartz/Buf-HIL substrates. .....	30
<b>Table 2.2</b> A summary of published luminance overshoot of PeLEDs with visible emission.....	59
<b>Table 3.1</b> Summarized electrical and luminance characteristics of PeLEDs.....	94
<b>Table 3.2</b> Summarized EQE at high-brightness operation of PeLEDs. .....	96
<b>Table 3.3</b> Summary of the reported PeLEDs characteristics based on maximum EQE, maximum luminance, and half-lifetime.....	104



## List of Figures

<b>Figure 1.1</b> Maximum EQE vs year and emission characteristics of organic LED, inorganic QD LED, and perovskite LEDs.....	3
<b>Figure 1.2</b> Crystal structure of metal halide ABX <sub>3</sub> perovskites (left) and FWHM vs molecular dimension of organic emitter, inorganic QDs, and metal halide perovskite materials. ....	4
<b>Figure 1.3</b> EQE and operational lifetime trend over time of PeLEDs since 2014. Opened square in EQE curve indicates Lambertian assumption of angle-dependent emission profile, and opened circle in lifetime curve indicates estimated value of lifetime from accelerated lifetime test.. ....	6
<b>Figure 1.4</b> Schematic illustration of 3D, quasi-2D, nanoparticle structure perovskite materials showing each type of material' s advantages and disadvantages.....	7
<b>Figure 1.5</b> Strategies to overcome lifetime limitation of perovskite emitters.....	8
<b>Figure 2.1</b> Principal scheme of our study. The neutral reagent, benzylamine (BnA) leads to the formation of 3D/2D hybrid perovskites while aniline (ANI) does not induce the formation of 2D	



perovskites.....	20
<b>Figure 2.2</b> Proton–transfer induced 2D perovskite formation with BnA. <b>a</b> $^1\text{H}$ NMR spectra of $\text{MAPbBr}_3$ precursor solutions in $\text{DMSO}-d_6$ according after addition of additives. Pristine $\text{MAPbBr}_3$ (black), $\text{MAPbBr}_3$ with 2.4 mol% of ANI (black) and $\text{MAPbBr}_3$ with 2.4 mol% of BnA (green). <b>b, c</b> $^1\text{H}$ NMR spectra according to the different amount of BnA and ANI addition. <b>d</b> Electron density contour plots of BnA (bottom) and ANI (top) with an iso–surface of $0.03 \text{ e}\cdot\text{\AA}^{-3}$ . <b>e</b> Integrated electron density profile for BnA (green) and ANI (red) along with $b$ –axis in <b>d</b> . <b>f, g</b> Absorption spectra of $\text{MAPbBr}_3$ thin film according to the addition of BnA and ANI. <b>h</b> Proton–transfer reaction between MA and BnA.....	
	21
<b>Figure 2.3</b> $^1\text{H}$ NMR spectra of $\text{MAPbBr}_3$ solution (a) without additive, (b) with BnA 100 mol%, and (c) ANI 100 mol%.....	
	22
<b>Figure 2.4</b> Fluctuations of total energy as the evolution of simulation time and the snapshots of atomic configurations after the first–principles molecular dynamics (MD) simulations (3.5 ps) with a time step of 1.2 fs at the temperature of 300 K. <b>a</b> and <b>b</b> for the 2D perovskites formed by protonated BnA ( $\text{BnA}^+$ ) and unprotonated BnA, respectively. ....	
	23
<b>Figure 2.5</b> The $^1\text{H}$ MAS NMR spectra for the solid–state perovskites	



with varying **a** BnA concentration (0, 2.4, 30, 50 and 100%) and **b** ANI concentration (0, 2.4, and 100%) under a fast spinning speed of 40 kHz at 14.1 T. .... 24

**Figure 2.6** Crystal structure and morphology of MAPbBr<sub>3</sub> according to the addition of ANI or BnA. **a–c** 2D GIXD patterns of pristine MAPbBr<sub>3</sub>, MAPbBr<sub>3</sub> with 2.4 mol% ANI, and 2.4 mol% BnA. **d** Cross-sectional SEM images of pristine MAPbBr<sub>3</sub> (top), MAPbBr<sub>3</sub> with 2.4 mol% ANI (middle) and 2.4 mol% BnA (bottom)..... 27

**Figure 2.7** 2D GIXD patterns of **a**, pristine MAPbBr<sub>3</sub> film, **b**, with ANI 2.4 mol% , **c**, ANI 15 mol% , **d**, ANI 30 mol%, **e**, BnA 2.4 mol%, **f**, BnA 15 mol%, and **g**, BnA 30 mol%. **h**, 1D XRD profiles of pristine MAPbBr<sub>3</sub> film, MAPbBr<sub>3</sub> with ANI 2.4 mol% and BnA 2.4 mol%. 1D XRD profiles of MAPbBr<sub>3</sub> with different amounts of **i**, ANI and **j**, BnA. .... 28

**Figure 2.8** Scanning electron microscopic images (SEM) of MAPbBr<sub>3</sub> perovskite films. **a**, Top-view and **b**, cross-sectional view of pristine MAPbBr<sub>3</sub>, **c–e**, top-view and **f–h**, cross-sectional view with different amount of ANI, **i–k**, top-view, and **l–n**, cross-sectional view with different amounts of BnA. .... 29

**Figure 2.9** PL characteristics of perovskites and the trap passivation. **a**, PL spectrum of pristine MAPbBr<sub>3</sub> film (black), film with 2.4 mol%



of ANI (red), and 2.4 mol% of BnA (green)mol%. **b**, PL lifetime curves of pristine MAPbBr<sub>3</sub> film (black), film with 2.4 mol% of ANI (red), and 2.4 mol% of BnA (green). **c**, PL spectra of MAPbBr<sub>3</sub> film with different amount of BnA and magnified PL spectra at low wavelength region (inset). **d**, Normalized PL spectra of MAPbBr<sub>3</sub> film with different amount of BnA. .... 33

**Figure 2.10** PLQE of MAPbBr<sub>3</sub> film according to the amount of BnA addition. The films were excited with a continuous-wave 405 nm laser diode (2.5 mW cm<sup>-2</sup>). .... 34

**Figure 2.11 a**, Steady-state PL spectra and **b**, normalized PL spectra of MAPbBr<sub>3</sub> film with different amounts of ANI..... 35

**Figure 2.12 a-b**, UPS spectra of 3D MAPbBr<sub>3</sub> and **c-d**, 2D BnA<sub>2</sub>PbBr<sub>4</sub> films showing secondary cut-off (left column) and onset (right column) ..... 36

**Figure 2.13** Energy band structure of 3D and 3D/2D hybrid perovskites based on UPS result showing recombination behaviour (top) based on the configurations of grain and GB of each perovskite. .... 37

**Figure 2.14** Integrated PL as a function of the excitation density of 3D and 3D/2D hybrid perovskites..... 38

**Figure 2.15** Photo-physical analyses to investigate recombination



kinetics and trap states of perovskites. **a** Temperature–dependent PL of 3D perovskite and **b** Ratio between integrated PL of band emission and trap–mediated emission of 3D perovskite as a function of temperature and its fitted curve according to Boltzmann distribution function. **c** Temperature–dependent PL of 3D/2D hybrid perovskite. **d** Excited charge carrier density–dependent PL lifetimes of the perovskites. **e** Schematic of charge carrier recombination dynamics of the perovskites. **f**  $I$ – $V$  curves of hole–only devices with 3D perovskite and 3D/2D hybrid perovskite..... 43

**Figure 2.16** PL emission of 3D perovskite, MAPbBr<sub>3</sub> according to temperature from 70 K to 100 K. The peaks were deconvoluted into band–edge emission and trap–mediated emission..... 44

**Figure 2.17 a**, TCSPC curves of 3D perovskite and **b**, 3D/2D hybrid perovskite as a function of excited carrier density..... 45

**Figure 2.18** EL characteristics of PeLEDs. **a** Device structure of PeLEDs. **b** Current density of PeLEDs as a function of applied voltage. **c** Luminance of PeLEDs as a function of applied voltage. **d** External quantum efficiency (EQE) of PeLED as a function of applied voltage. **e** Current efficiency (CE) of PeLEDs as a function of applied voltage. **f** Normalized EL spectra of PeLEDs..... 47

**Figure 2.19** Current–voltage–luminance characteristics of PeLEDs



with various mol. % of BnA molecules. **a**, Current density, **b**, Luminance, **c**, current efficiency, **d**, external quantum efficiency (EQE), **e**, power efficiency of PeLEDs as a function of voltage. **f**, Current efficiency, **g**, EQE, **h**, luminance of PeLEDs as a function of current density. **i**, Normalized PL spectra of PeLEDs with various mol% of BnA..... 48

**Figure 2.20** EL characteristics of PeLEDs using pristine MAPbBr<sub>3</sub> emitter (red) and 2.4 mol % ANI added MAPbBr<sub>3</sub> emitter (blue). **a**, Current density of PeLEDs as a function of the applied voltage. **b**, Luminance of PeLEDs as a function of the applied voltage. **c**, External quantum efficiency (EQE) of PeLED as a function of the applied voltage. **d**, Current efficiency (CE) of PeLEDs as a function of the applied voltage..... 49

**Figure 2.21** Influence of ion migration in perovskites on PeLEDs. **a** Current behaviour of PeLEDs as a function of time under constant voltage of 3.5 V. **b** Voltage behaviour of PeLEDs under increasing step constant current of 0.16, 0.22, 0.44, 1.11, 2.22 mA·cm<sup>-2</sup> from the left column to the right in a sequence. **c** Magnified version of one step showing the discrepancy in the voltage behaviour between 3D PeLED and 3D/2D hybrid PeLED. **d** Capacitance–frequency curve of PeLEDs. **e** Schematic of possible ion migration pathways in 3D and



3D/2D hybrid perovskites and efficient restriction of ion migration owing to the BnA which has retardation effect of reorientation.  
 .....53

**Figure 2.22** Schematic showing ion migration pathway in 3D (left) and 3D/2D hybrid (right) perovskite.....i

**Figure 2.23 a**, HAADF scanning TEM image of a 3D/2D hybrid perovskite grain. **b**, High-resolution image of the grain framed with the yellow box in **a** showing the 2D perovskite ( $n = 1$ ) with  $d$ -spacing of 1.15 nm. It is worth noting that the smaller  $d$ -spacing (1.15 nm) than that obtained by grazing-incident X-ray diffraction (GIXD) analysis (1.66 nm) can be attributed to transient lattice contraction due to the highly strong beam intensity. Interestingly, the highly periodic 2D perovskite was only observable at the shell region of the grain. Because the 2D perovskite has lower surface energy than the 3D perovskite due to its fewer surface dangling bonds and surface relaxation, growth of the 2D perovskite most possibly occurs on the 3D perovskite grains and it also makes an interface with grain boundary which has the highest surface energy, thereby lowering the total potential energy of the system. Therefore, the mounted 2D perovskite on the 3D perovskite can effectively passivate the traps and block ion migration. **c**, A lower magnification HAADF scanning



TEM image of the 3D/2D hybrid perovskite grain shown in **a**, corresponding EDXS elemental maps of **d**, Pb and **e**, Br, and **f**, integrated EDX spectrum of the acquired dataset. HAADF-STEM images and corresponding EDXS elemental maps indicate that the grain is composed of Pb and Br elements. .... 55

**Figure 2.24** Reliability and long-term stability of PeLEDs. **a**,  $J-V$  and **b**,  $L-V$  curves of 3D PeLEDs with a repetition of voltage sweep and **c-d**, those of 3D/2D hybrid PeLED. **e**, Relative luminance of 3D/2D hybrid PeLED (green) and of 3D PeLED (red) over time. **f**, Magnified version of relative luminance of PeLEDs showing an extremely reduced overshoot of luminance. **g**, Voltage curves of 3D/2D hybrid PeLED (green) and 3D PeLED (red) over time under constant current to make PeLEDs have an emission of  $100 \text{ cd m}^{-2}$ . .... 60

**Figure 2.25** Current-voltage hysteresis on forward-backward sweep of **a**, 3D PeLED and **b**, 3D/2D hybrid PeLED..... 61

**Figure 2.26** Relative luminance of PeLEDs using pristine MAPbBr<sub>3</sub> emitter and 2.4 mol % ANI-added MAPbBr<sub>3</sub> emitter over time. .... 62

**Figure 2.27** A summary of reported luminance overshoot ratio versus half lifetime of PeLEDs with green emission on table 2.2 ( $L_{\text{max}}$ : maximum luminance,  $L_0$ : initial luminance). .... 63



**Figure 3.1 a**, Schematic illustration of the transformation process of 3D (left) into *in situ* particle (middle) and *in situ* core/shell (right) structure by BPA treatment. TEM image of perovskite nanograins during *in situ* core/shell synthesis process with reaction time of **b**, 1 s, **c**, 10 s, **d**, 20 s, **e**, 30 s. (insets: low-magnification TEM images). **f–h**, High-resolution TEM images of the boxed regions in **b–d**. (insets: FFT-diffractograms showing the cubic lattice structure) **i**, High-resolution HAADF-STEM image of the single *in situ* core/shell NP taken from the boxed region in **e**, showing a flat interface between the perovskite core and the BPA shell. **j**, Atomically resolved HAADF-STEM image of the core region taken from the *in situ* core/shell perovskite NP with atomic structure model, showing the perfect 3D perovskite crystal structure. **k**, High-resolution STEM image focusing on surface region of *in situ* core/shell. **l**, the EEL spectra acquired from the positions A and B highlighted in **k**. The Si peak is a background signal from the silicon nitride TEM window grid.

..... 75

**Figure 3.2** SEM image of perovskite thin films made of 1.2M precursor solution with **a**, 0 % (3D), **b**, 2.5 %, **c**, 5 %, **d**, 10 % (*in situ* particle) molar ratio of BPA molecule relative to PbBr<sub>2</sub>..... 76

**Figure 3.3 a**, HAADF-STEM image and EDS elemental maps of P



(green), Br (yellow), and Pb (red), respectively. **b**, HAADF–STEM image and EDS elemental maps of a single perovskite grain showing the uniform dispersion of P (green), Br (yellow), and Pb (red) on the grain..... 77

**Figure 3.4 a**, SEM image of a perovskite thin film (after 1 s of reaction time with BPA–THF solution) showing small grains cracked out from large 3D grain. **b**, STEM image of 50–nm–size perovskite crystal during *in situ* core/shell synthesis process. Yellow arrows indicate the defective perovskite surfaces that can be bound with BPA. **c**, HR–TEM image of another perovskite crystal showing ultra–small nanocrystals segregated during *in situ* core/shell synthesis process. Insets: Magnified HR–TEM images of ultra–small nanocrystals taken from the white–boxed regions labelled C1 and C2. **d–e**, High–resolution HAADF–STEM images of single perovskite nanograins with decreasing grain size. Magnified HAADF–STEM images of the grain surfaces (D1, D2, E1, E2, F1, F2, G1, G2) demonstrate that the BPA shell coverages on the grain surfaces gradually increase and the defective surface regions decrease as the grain size decreases. 78

**Figure 3.5 a**, High–resolution HAADF–STEM image of single perovskite grain formed during *in situ* core/shell synthesis process. **b, c**, Atomic–scale HAADF–STEM (**b**) and ABF–STEM (**c**) images



of the boxed area denoted in **a**. **d,e**, Magnified HAADF–STEM (**d**) and ABF–STEM (**e**) images of the boxed area shown in **b** and **c** to indicate the positions of EELS acquisition. **f**, EEL spectra acquired at the atomic positions labelled A, B, and C in **d**, **e**. **g**, EEL spectrum in the energy–loss range of the N–K and O–K edges acquired at the position labelled C. The O–K peak indicates the presence of BPA shells, but N–K peak is simply a background signal from the silicon nitride TEM window grid. .... 79

**Figure 3.6** **a**, 3D perovskite without reaction, **b**, 1 s, **c**, 15 s, **d**, 30 s of exposure time to BPA–THF solution before spin–drying. Colored regions indicate *in situ* particle perovskites (red) and *in situ* core/shell perovskites (green). **e**, Schematic illustration of the growth process of BPA macroparticle domain and perovskite crystal forming *in situ* core/shell structure. .... 80

**Figure 3.7** **a**, TEM image and **b**, **c**, magnified HAADF–STEM images of *in situ* core/shell thin films. **d**, HAADF–STEM image of *in situ* core/shell grains and EDS elemental maps of P (red), Pb (yellow), and Br (green), respectively. The EDS maps clearly show the uniform dispersion of P (red) over macrograins. **e**, HAADF–STEM image of single macrograins consists of *in situ* core/shell NPs. **f**, EDS spectrum acquired at the location of the red circled region in **e**.



.....	81
<b>Figure 3.8</b> Top SEM image and corresponding grain size analysis of <b>a</b> , 3D, <b>b</b> , <i>in situ</i> particle, and <b>c</b> , <i>in situ</i> core/shell (inset: magnified view of STEM image in macroparticle showing each <i>in situ</i> core/shell grain) perovskite thin films with concentration of 1.2M.....	82
<b>Figure 3.9</b> <b>a</b> , P 2p, <b>b</b> , O 1s, <b>c</b> , Pb 4f, <b>d</b> , Br 3d XPS core level spectra of 3D, <i>in situ</i> particle, <i>in situ</i> core/shell structure perovskite thin films. The lowered proportion of the O 1s spectra at 531.0 eV in the <i>in situ</i> core/shell structure than that in the <i>in situ</i> particle structure can be understood as the presence of BPA molecules that cannot bind to the perovskite surface and can self-assemble to form macroparticles. ....	85
<b>Figure 3.10</b> <b>a–c</b> , O 1s XPS core-level spectra of <b>a</b> , BPA, <b>b</b> , <i>in situ</i> particle perovskite, <b>c</b> , <i>in situ</i> core/shell perovskite. <b>d</b> , <sup>1</sup> H NMR spectra of BPA and BPA–PbBr <sub>2</sub> solution in DMSO d <sub>6</sub> with different temperature. <b>e</b> , <sup>1</sup> H NMR spectra of BPA in DMSO d <sub>6</sub> . <b>f</b> , Energy level diagram of the pristine 3D, <i>in situ</i> particle, <i>in situ</i> core/shell perovskites obtained from parameters derived from UPS spectra. ....	86
<b>Figure 3.11</b> UPS spectra of 3D, <i>in situ</i> particle, <i>in situ</i> core/shell perovskite films showing <b>a</b> , secondary cut-off and <b>b</b> , onset.....	87



**Figure 3.12 a**, PL spectrum of 3D, *in situ* particle, and *in situ* core/shell perovskite films. **b**, PL lifetime curves of 3D, *in situ* particle, and *in situ* core/shell perovskite films. **c–e**, Two-dimensional (2D) map of temperature-dependent PL spectra of 3D, *in situ* particle, *in situ* core/shell perovskite film respectively (normalized to peak value)..... 90

**Figure 3.13** External PLQE vs internal radiation efficiency ( $\eta_{\text{rad}}$ ) of perovskite film calculated considering the influence of perovskite reabsorption<sup>55,56</sup>. 3D, *in situ* particle, and *in situ* core/shell perovskite thin films exhibit the external PLQEs of 4.4 %, 4.8 %, and 46 %, which correspond to  $\eta_{\text{rad}}$  of 30 %, 32 %, 89 %, respectively. .... 91

**Figure 3.14** Temperature-dependent PL spectrum and corresponding integrated PL intensity with calculated activation energy of **a,d**, 3D, **b,e**, *in situ* particle, **c,f**, *in situ* core/shell perovskite thin films..... 92

**Figure 3.15** Current density vs voltage for HODs under dark conditions. Inset: Device structure. SCLC fitting (dashed lines) shows the trap-filling limit voltage ( $V_{\text{TFL}}$ ), showing reduced trap densities of *in situ* particle structure and *in situ* core/shell structure. .... 93



**Figure 3.16** **a**, schematics of energy diagram of PeLEDs. **b**, luminance vs voltage, **c**, EQE vs luminance, and **d**, EQE histogram of PeLEDs. **e**, photograph of operating large–area device. (pixel size: 120 mm<sup>2</sup>) **f**, Summary of the reported green PeLEDs characteristics based on maximum EQE and luminance. **g**, Luminance vs time of PeLEDs based on *in situ* core/shell perovskites at various initial brightness. **h**, half–lifetime vs brightness from accelerated lifetime test of *in situ* core/shell structure PeLEDs. **i**, Summary of the reported PeLEDs characteristics based on maximum EQE and estimated or measured half–lifetime at 100 cd m<sup>−2</sup>..... 98

**Figure 3.17** Schematic illustration of device efficiency characterization setup for current–voltage–luminance measurement and goniometric measurement..... 99

**Figure 3.18** **a**, Imaginary part of refractive index ( $k$ ) and internal radiation spectrum used for the simulation.  $n = 2.3$  is assumed for perovskite. **b**, Calculated maximum EQE (EQE<sub>max</sub>) considering the effect of photon recycling as a function of perovskite thickness in our device. Background colors represent the fractions of outcoupling, waveguide, substrate, and plasmon modes per each condition. Non–outcoupled photons are reabsorbed by either perovskite ( $A_{act}$ ) or parasitic layers ( $A_{para}$ )..... 100



**Figure 3.19** **a**, Current density vs voltage; **b**, luminance vs current density; **c**, Normalized EL spectra; **d**, power efficiency vs luminance; **e**, current efficiency luminance of PeLEDs based on 3D, *in situ* particle, *in situ* core/shell structure. **f**, luminance histogram; **g**, Angle-dependent EL intensity of PeLEDs based on *in situ* core/shell structure. **h**, EQE versus vs density of OLEDs measured in our lab at Seoul National University (SNU) and at the Cavendish group at University of Cambridge. **i**, EQE histogram of the PeLEDs based on *in situ* core/shell structure with different processing condition. As the temperature of the glove box increases or the A-NCP process is delayed, the grain size of the spin-coated perovskite thin film increases, and this increase slows the penetration of the BPA solution into perovskite crystal and impedes their full conversion into the *in situ* core/shell structure.....101

**Figure 3.20** **a**, luminance vs voltage, **b**, EQE vs current density of large-area devices based on *in situ* core/shell perovskites. Photographs of large-area devices (Pixel size: 120 mm<sup>2</sup>) operating at **c**, <10 cd m<sup>-2</sup>, **d**, 1,000 cd m<sup>-2</sup>, **e**, 100,000 cd m<sup>-2</sup>, and **f**, 100,000 cd m<sup>-2</sup> under daylight, showing uniform emission over the pixel. ....102

**Figure 3.21** **a**, Luminance vs time of PeLEDs based on 3D, *in situ*



particle, and *in situ* core/shell perovskite at initial brightness of 10,000 cd m<sup>-2</sup> and **b**, corresponding driving voltage vs operation time.

.....103

**Figure 4.1 a**, luminance vs voltage of practical PeLEDs and OLEDs.

Red boxed region indicates catastrophic failure occurring only in PeLEDs. **b**, Simplified scheme of ion diffusion from perovskite layer toward metallic electrode resulting in electrochemical corrosion of electrode. **c**, Ion-induced failure cycle as a working mechanism of catastrophic failure in PeLEDs.....108

**Figure 4.2** Comprehensive degradation analysis procedure for step-by-step degradation stage of *in situ* particle with catastrophic failure and *in situ* core/shell PeLEDs without catastrophic failure. ....109

**Figure 4.3** ToF-SIMS ionic depth profiles for fresh and *L*<sub>50</sub> devices of **a**, *in situ* particle PeLEDs and **b**, *in situ* core/shell PeLEDs, respectively. ....116

**Figure 4.4** OM image of the Al cathode before and after 50% of degradation of **a-b**, *in situ* particle PeLEDs, and **c-d**, *in situ* core/shell PeLEDs. **e**, top-view, **f-g**, cross-sectional view of Al cathode from *in situ* particle PeLEDs after device degradation.....

.....117

**Figure 4.5** Individual XPS spectra obtained at the delaminated Al



cathode after operation of **a**, in situ particle and **b**, in situ core/shell PeLEDs during each step-by-step degradation process..... 119

**Figure 4.6** Capacitance–voltage characteristics of **a**, in situ particle PeLEDs and **b**, in situ core/shell PeLEDs during each step of degradation processes. **c**, Normalized Vmax of PeLEDs with each step of degradation processes. **d**, Normalized EL spectra of in situ particle PeLEDs during each step of degradation processes. **e**, Schematic diagram on energy level of PeLEDs and carrier injection. .... 122

**Figure 4.7** Luminance, voltage, temperature vs time of in situ particle, in situ core/shell PeLEDs operated at constant current of 2 mA. Inset at the bottom shows magnified view of temperature vs time curve of in situ particle PeLEDs. .... 126

**Figure 4.8** Temperature–dependent ion conductivity of the in situ particle perovskite film. .... 127

**Figure 4.9** **a**, luminance vs time of in situ particle PeLEDs under various brightness at room temperature and controlled low temperature..... 128

**Figure 4.10** Steady–state PL spectra of PeLEDs at each degradation stage based on **a**, *in situ* particle and **b**, in situ core/shell perovskites. **c**, Normalized PL intensity from **a,b**. .... 130



<b>Figure 4.11</b> Summarized graph of catastrophic failure process with ion diffusion in PeLEDs.....	132
<b>Figure 5.1</b> Strategies to overcome the lifetime limitation of PeLEDs. .....	136



# Chapter 1. Introduction

## 1.1. Megatrend of Display

The development of displays has been considered very important in that more than 70% of human information recognition is achieved through vision. In particular, the importance of a vivid display that makes the screen feel like reality, is increasingly emerging for realization of ultra-high-definition television (UHD-TV) and artificial reality (AR) displays. From this point of view, the currently most widely used self-emitting OLED has the disadvantage of having a very large full-width at half maximum (FWHM) that can measure the color purity of the luminous color compared to high-efficiency and high-resolution. Thus, new luminous materials such as inorganic quantum dot and perovskite that can replace it are being studied (Figure 1.1).

From this perspective, metal halide perovskites (MHPs), an ionic  $ABX_3$  structure (A: organic or inorganic cation, B: center metal, X: halide anion), are attracting great attention for its excellent light emission property with vivid and highly-pure emission color ( $FWHM \approx 20$  nm); they are promising candidates for use in next-generation displays to overcome the colour limitations of displays using commercial organic light-emitting diodes (Figure 1.2)<sup>1-3</sup>. The broad range of color gamut for REC. 2020 color standard, which is essential for vivid UHD-TV and AR display application, cannot be implemented with emitting system having wide FWHM such as a conventional organic light emitting material ( $FWHM \sim 50$ nm) or



quantum dot (FWHM  $\sim 30\text{nm}$ ), and can be implemented only with a perovskite emitter having a very narrow emission spectra (FWHM  $\sim 20\text{nm}$ ).







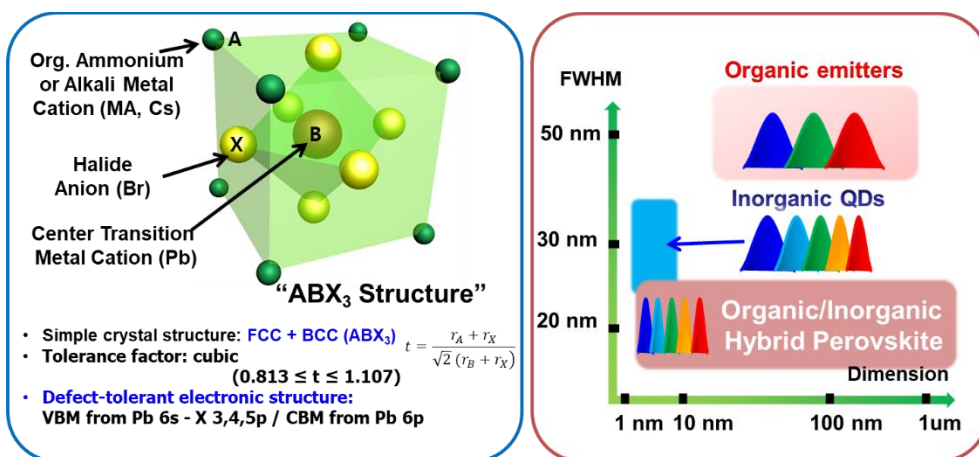


**Figure 1.2** Crystal structure of metal halide ABX<sub>3</sub> perovskites (left) and FWHM vs molecular dimension of organic emitter, inorganic QDs, and metal halide perovskite materials.



## 1.2. Challenges for realizing stable perovskite LEDs

Because of the advantages mentioned above, numerous research has been conducted to achieve efficient perovskite light-emitting diodes (PeLEDs). By introducing perovskite nanocrystal structure, high external quantum efficiency (EQE) of 23.4 % could be achieved due to strong carrier confinement and compressive suppression of defect states<sup>2,4-11</sup>. Still, the operational lifetime of PeLEDs are still in order of hundreds to thousands of hours, which is far behind than that of the commercial OLED and QD LEDs with half-lifetime over 1,000,000 h normally (Figure 1.3).

These perovskite nanocrystal (NC) emitters suffer from the insulating characteristics of long alkyl ligands that impedes charge injection and transport, limiting the brightness and operational lifetime (Figure 1.4)<sup>12-15</sup>. In contrast, 3D polycrystalline perovskite thin film showed fast charge transport and relatively long operational lifetime (maximum luminance  $>100,000 \text{ cd m}^{-2}$ , device half-lifetime ( $T_{50}$ )  $> 200 \text{ h}$  at initial brightness =  $100 \text{ cd m}^{-2}$ ), but suffers from low EQE because the charge confinement was too low in large grains and non-radiative recombination easily occur at the grain boundary<sup>16-20</sup>. Despite of improvements on both NC and 3D structure enabled advances in EQE of PeLEDs, the inevitable trade-off between charge confinement and charge transport limited the ideal device behavior of state-of-the-art PeLEDs with maximum EQE  $>20 \%$ , showing low brightness ( $\sim 10,000 \text{ cd m}^{-2}$ )<sup>5,8,14</sup> and short  $T_{50}$  ( $< 100 \text{ h}$  at initial brightness =  $100 \text{ cd m}^{-2}$ )<sup>5</sup>. Therefore, ideal material system for high brightness, high efficiency and long operational lifetime is of great importance at the current stage of research on PeLEDs.



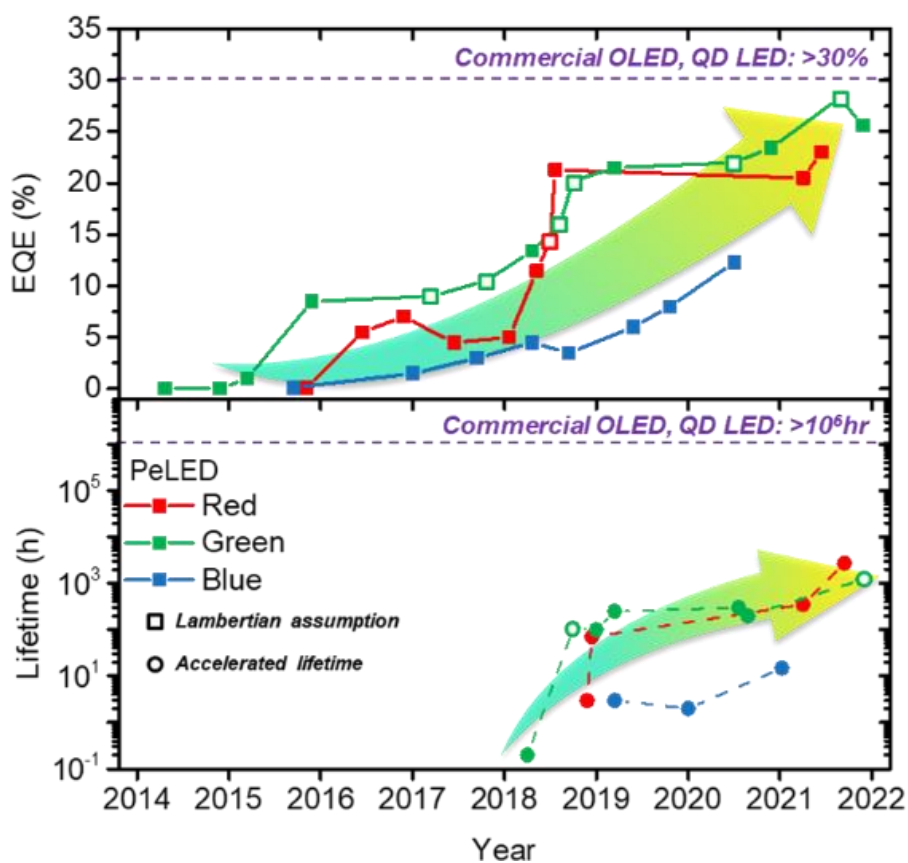


**Figure 1.3** EQE and operational lifetime trend over time of PeLEDs since 2014. Opened square in EQE curve indicates Lambertian assumption of angle-dependent emission profile, and opened circle in lifetime curve indicates estimated value of lifetime from accelerated lifetime test.



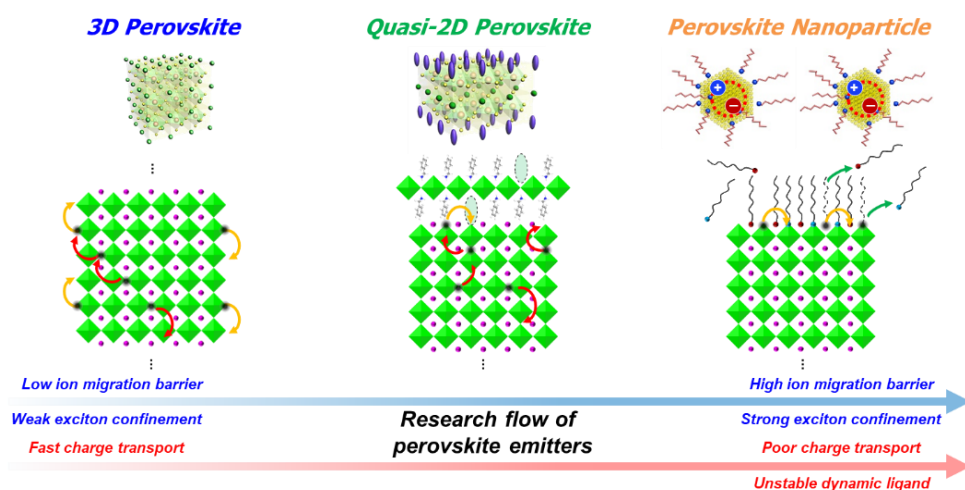


**Figure 1.4** Schematic illustration of 3D, quasi-2D, nanoparticle structure perovskite materials showing each type of material's advantages and disadvantages.



### 1.3. Outline of the thesis

In this thesis, strategies toward realization of long-term stable PeLEDs by incorporation of various core/shell structure emitter system will be presented. Operational stability and efficiency of PeLEDs were improved by utilizing 1) grain size reduction, 2) emitter system with suppressed surface trap states, and 3) stable crystal surface of perovskite grains by ideal shell molecules (Figure 1.5). Also, the origin of instability in perovskite emitter and light-emitting devices were studied.

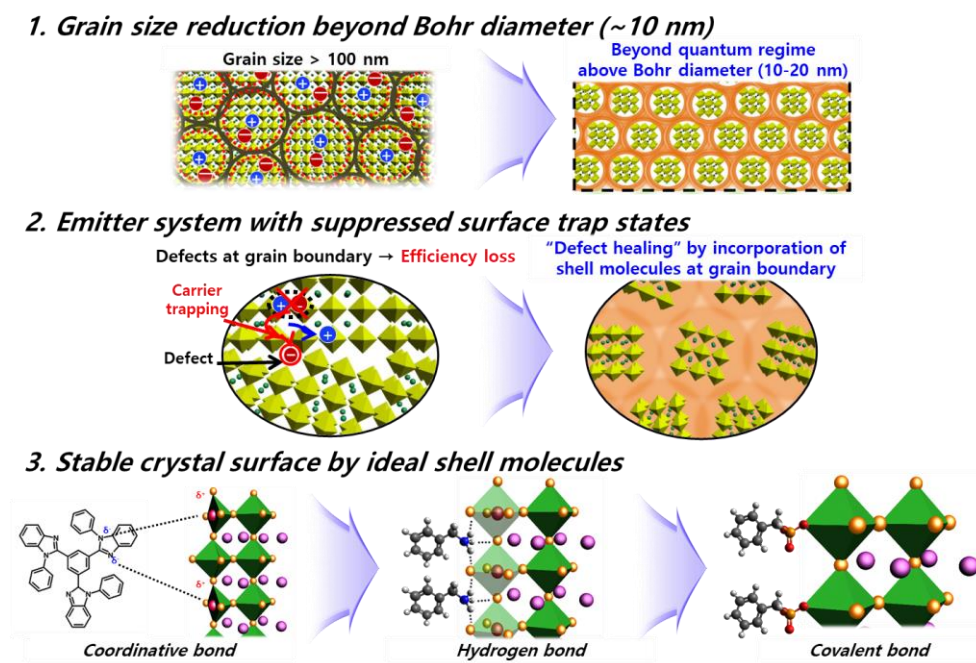


**Figure 1.5** Strategies to overcome lifetime limitation of perovskite emitters.



# **Chapter 2. Proton-Transfer-Induced 3D/2D Hybrid Core/Shell Perovskite LEDs with Suppressed Ion Migration and Luminance Overshoot**

## **2.1. Introduction**

In the early days of the research on perovskites light-emitting diodes (PeLEDs), three-dimensional (3D) polycrystalline perovskites have been employed as a light-emitter based on the advantages such as a high colour purity, facile tuning of emission colour, low material cost and low-temperature processibility.<sup>1,221</sup> Extensive research has contributed to rapid increase of luminous efficiency in PeLEDs by various approaches such as an introduction of nanocrystal pinning (NCP) process, a management of compositional distribution, an incorporation of polymer into perovskite and an enhancement in light outcoupling.<sup>2,5,7,22</sup> However, 3D polycrystalline perovskite emitters have fundamental limitations in achieving efficient radiative recombination due to small exciton binding energy and long electron-hole diffusion length. In addition, PeLEDs have a very short operating lifetime, primarily as a result of ion migration in 3D polycrystalline perovskite; this problem must be overcome before they can be practically used for lighting and displays.



There have been many reports on PeLEDs regarding overshoot of luminance during the initial stage of operation.<sup>5,22–24</sup> However, the mechanism of this phenomenon has not been identified. Furthermore, the ion migration can much negatively influence on device stability because the PeLEDs operate under much higher applied electric field compared with perovskite solar cells. Therefore, to improve the device lifetime of PeLEDs, ion migration must be suppressed.<sup>23,25–28</sup> Especially, the ion migration mostly occurs on grain boundaries (GBs), thus blocking possible migration pathways along the GB can be an effective strategy to suppress it.<sup>29</sup>

In this study, we developed a 3D/2D hybrid perovskite emitter that can be an ideal configuration to suppress ion migration and improve the operational stability of PeLEDs with significantly reduced overshoot of luminance during the initial stage. In a conventional way to develop the 2D perovskite in the bulk 3D perovskite, an ammonium halide salt with a bulky backbone (e.g. phenethylammonium halide (PEAX), or *n*-butylammonium halide (*n*-BAX)) and the salts of a 3D perovskite (e.g. methylammonium halide (MAX) and lead halide ( $\text{PbX}_2$ )) have been dissolved together in a solvent or mixed solvents as a precursor of the quasi-2D perovskite.<sup>24,30–33</sup> Here, unlike the conventional way, we only incorporated small amount of a liquid-form neutral reagent, benzylamine (BnA) into the methylammonium lead bromide ( $\text{MAPbBr}_3$ ) precursor to induce proton transfer from  $\text{MA}^+$  to BnA; as a result, a 3D/2D hybrid structure formed. Therefore, the synthetic procedure which requires strong hydrohalic acid reagents to obtain the organic ammonium halide salt for 2D perovskites becomes unnecessary. In contrast, the addition of aniline (ANI) does not make the structural change maintaining the 3D phase of perovskite as the case



without an additive.  $^1\text{H}$  nuclear magnetic resonance (NMR) spectroscopy revealed that the strongly-basic BnA participates in crystallization of 2D perovskite by being transformed into  $\text{BnA}^+$  by proton-transfer from  $\text{MA}^+$  in the precursor. Grazing-incident x-ray diffraction (GIXD) technique confirmed the formation of 2D  $\text{BnA}_2\text{PbBr}_4$ , dominantly with  $n = 1$ , while retaining the 3D  $\text{MAPbBr}_3$  phase. In contrast, ANI which has the similar molecular structure with BnA does not work as a reagent because it is weakly basic, so cannot induce the formation of additional 2D perovskite. The 3D/2D hybrid perovskite film showed a significant improvement in photoluminescence (PL) characteristics compared to the 3D perovskite film because the 2D perovskite can passivate trap sites in 3D perovskite, and thereby leading to an efficient radiative recombination. Therefore, PeLEDs with the 3D/2D hybrid perovskite emitter had highly improved electroluminescence (EL) efficiency. More importantly, the 3D/2D hybrid PeLEDs also showed a dramatic enhancement in the long-term stability owing to the suppressed ion migration which led to an extremely reduced initial luminance overshoot compared to the 3D PeLEDs. The 3D/2D hybrid PeLED had  $> 21$  times longer operational lifetime ( $T_{40} = 810$  min) than 3D PeLEDs ( $T_{40} = 38$  min). We cohesively linked the suppression of ion migration to the retardation effect of BnA reorientation based on their  $\pi$ - $\pi$  interaction.



## 2.2. Experimental

**Materials** TPBi was purchased from OSM and Methylammonium bromide (MABr) was purchased from Greatcell Solar. Lead bromide ( $\text{PbBr}_2$ ) (99.999%), Aniline (ANI) (ACS Reagent, 99.5%), Benzylamine (BnA) (ReagentPlus, 99%), Lithium Fluoride (99.99%, trace metal basis), Dimethyl sulfoxide (DMSO) (99.8%, anhydrous) were purchased from Sigma-Aldrich. All chemicals were used as received.

**Preparation of perovskite precursor solution**  $\text{MAPbBr}_3$  precursor solutions (35.0 wt. %) were prepared by dissolving MABr and  $\text{PbBr}_2$  in DMSO with a molar ratio of 1.06:1 (MABr :  $\text{PbBr}_2$ ), and then stirred overnight. Before spin-coating the solution, the neutral amine additive (ANI or BnA) was added into the  $\text{MAPbBr}_3$  precursor solution.

**Device fabrication** For PeLEDs, the Buf-HIL layer was spin-coated on a cleaned FTO-coated glass at 3000 rpm for 90 s, and samples were annealed on a hot plate for 30 min at 150 °C in air. Buf-HIL solution was composed of PEDOT:PSS (Clevios P VP AI4083) and tetrafluoroethylene-perfluoro-3,6-dioxo-4-methyl-7-octene-sulfonic acid copolymer (PFI) (Sigma-Aldrich) (1:1 wt:wt). On the prepared substrate, the prepared perovskite precursor solution was spin-coated at 3000 rpm, followed by the additive-based nanocrystal-pinning process to induce immediate crystallization of perovskite by using TPBi solution in chloroform<sup>2</sup>. The deposited perovskite film was annealed on a hot plate at 90 °C for 10 min. Subsequently, 50 nm of TPBi, 1 nm of LiF, and 100 nm of Al were thermally evaporated in sequence in a high-vacuum chamber to complete the device. For HODs, 30 nm of molybdenum



oxide ( $\text{MoO}_3$ ) and 50 nm of Au were thermally deposited on top of  $\text{MAPbBr}_3$  to make a structure of glass/FTO/BuF-HIL/ $\text{MAPbBr}_3$ / $\text{MoO}_3$ /Au in the high-vacuum chamber. The devices were encapsulated in  $\text{N}_2$  atmosphere and the pixel area of a device was  $4.8 \text{ mm}^2$ .

**$^1\text{H}$  NMR measurement** The  $^1\text{H}$  NMR spectra were obtained using a high-resolution NMR spectrometer (Bruker Advance 600 MHz). For the measurement, the perovskite precursor solution was prepared as mentioned above, except that the precursors were dissolved in  $\text{DMSO-}d_6$  (1 mL). For additive-mixed solutions, different amounts of BnA or ANI were added to the precursor solution as the experimental sample. The samples were prepared at room temperature in  $\text{N}_2$  atmosphere, and their characteristics were measured at room temperature.

**$^1\text{H}$  MAS NMR spectroscopy**  $^1\text{H}$  MAS NMR spectra of the samples were collected at room temperature on a Bruker NMR system (14.1 T) at Larmor frequency of 600.41 MHz with a 1.9-mm triple-resonance Bruker NMR probe using a spin-echo pulse sequence at a spinning speed of 40 kHz. Fast sample spinning speed of 40 kHz yielded high-resolution  $^1\text{H}$  MAS NMR spectra. The spin-echo pulse sequence ( $\pi/2-t-\pi-t$ ) was used to suppress  $^1\text{H}$  background signals from the probe. The  $\pi/2$  pulse length of  $2 \mu\text{s}$  was applied for the samples and a recycle delay time of 10 s was used. Approximately 0.5–6 mg of perovskite powder after being scraped off the film was used. To improve the signal-to-noise ratio, around 16 to 256 scans were averaged in the  $^1\text{H}$  MAS NMR spectra. The  $^1\text{H}$  NMR spectra were referenced externally using tetramethylsilane (TMS) solution.

**Characterizations of perovskite films** The absorbance of the perovskite film was measured using UV-vis absorption spectrophotometer (Cary-5000). Steady-state PL



of the film was measured using a spectrofluorometer (JASCO FP6500). Xenon arc lamp with continuous output power of 150 W was used as an excitation source, and the excitation wavelength was 365 nm. The light was incident from the glass side. XRD analysis was carried out using X-ray diffractometer (PANalytical) with Cu  $\alpha$  radiation at a scan rate of 4°/min. GIXD was performed on the perovskite film at the 6D and 9A beamlines at the Pohang Accelerator Laboratory, Korea. Top-view and cross-sectional SEM images of the perovskite films were obtained using a field-emission SEM (MERLIN compact, ZEISS) at the Research Institute of Advanced Materials in Seoul National University. TCSPC measurement was conducted by using TCSPC module (FluoTime 300, PicoQuant). The instrument response function (IRF) was ignored because the PL lifetime curves were much longer than the temporal width of the IRF. The excitation power density was around 25 mW·cm<sup>-2</sup>, and the excitation wavelength was fixed at 405 nm. The excitation power density was determined by using a laser power meter (Thorlabs) for the excitation-dependent PL lifetime measurement. For the temperature-dependent PL measurement, the sample was mounted in a cryostat under vacuum condition. The target temperature was equilibrated by over 3 min stabilization before measuring a steady-state PL spectrum. Ultraviolet Photoemission Spectroscopy (UPS) of the perovskite films was measured using a photoelectron spectrometer (Kratos Inc., AXIS-Ultra DLD) with He I radiation (21.2 eV) in collaboration with Korea Basic Science Institute (KBSI). PLQE of perovskite thin films on quartz substrate was measured by using the integrating sphere method with a continuous-wave 405 nm laser diode (2.5 mW cm<sup>-2</sup>).



**Transmission electron microscopy (TEM) analysis** High-angle annular dark-field scanning transmission electron microscopy (HAADF-STEM) and energy-dispersive X-ray spectrum (EDXS) imaging were performed on an aberration-corrected Titan-Themis 60-300 (Thermo Scientific) at an acceleration voltage of 200 kV with probe currents of approximately 100 pA and 500 pA, respectively. This microscope is equipped with a high brightness Schottky X-FEG gun, a Super-X EDX system comprising four silicon drift detectors, and Velox acquisition software. The specimen for STEM analysis was prepared on a carbon support grid by dripping solution which was a dispersion of perovskite powder in chloroform after being scraped off the film.

**Characterization of PeLEDs** The current-voltage-luminance characteristics of PeLEDs were measured using a source-measurement unit (Keithley 236), a spectroradiometer (Minolta CS-2000), and a control computer. The operational lifetime of the PeLEDs was measured using a lifetime measurement system (M6000, McScience) under a constant current condition that yielded luminance of 100 cd·m<sup>-2</sup>. Capacitance-voltage, capacitance-frequency, and time-dependent *J-V* characteristics were measured using a Solartron 1260 impedance/gain-phase analyzer with a Solartron 1287 potentiostat.

**Charge-density calculation details** Charge-density calculations were conducted using a plane-wave pseudopotential approach within density functional theory as implemented in the Viena Ab Initio Simulation Package. The electron-core interactions were described with the projected augmented wave pseudopotentials and the exchange and correlation functional were treated using the Perdew-Burke-Ernzerhof parametrization of GGA for structural relaxations. The molecule was



placed in the middle of a size-fixed cubic cell with  $a = b = c = 30 \text{ \AA}$  to optimize the atomic configuration. The electronic energy was minimized with a tolerance of  $10^{-6}$  eV, and ionic relaxation was performed with a force tolerance of  $0.01 \text{ eV \AA}^{-1}$  on each ion. The kinetic energy cutoff was set as 520 eV, and a Gamma point was used for the Brillouin zone integration. The charge density along  $b$ -axis was integrated from the CHGCAR by  $\rho(y) = \int \rho(x, y, z) dx dz$ .



## 2.3. Result and Discussion

### Protonation of benzylamine enabling 2D perovskite formation

The incorporation of BnA into MAPbBr<sub>3</sub> precursor leads to the formation of 3D/2D hybrid dimensional perovskite in which the formation of 2D perovskite does not degrade the existing 3D phase so that 3D and 2D perovskites coexist (Figure 2.1). In contrast, the addition of ANI does not make the structural change maintaining the 3D phase of perovskite as the case without an additive. We performed <sup>1</sup>H NMR spectroscopy to understand the underlying chemistry in MAPbBr<sub>3</sub> precursor according to the addition of 2.4 mol% of ANI or BnA compared to MAPbBr<sub>3</sub> without the addition before the crystallization of perovskites occurs (Figure 2.2a). The precursors were dissolved in dimethyl sulfoxide-*d*<sub>6</sub> (DMSO-*d*<sub>6</sub>) as the same condition of the films for actual PeLEDs which we will discuss in the following sections. The spectrum of pristine MAPbBr<sub>3</sub> precursor showed two dominant proton signals, one at  $\delta = 7.44$  ppm that represents the ammonium ( $-\text{NH}_3^+$ ) of MA<sup>+</sup>, and the other at 2.32 ppm that represents its methyl ( $-\text{CH}_3$ ) group. The addition of BnA to the precursor of MAPbBr<sub>3</sub> caused an upfield shift of the proton signal of the ammonium group to  $\delta = 7.31$  ppm. The proton signal of the ammonium group progressively showed further upfield shift as the amount of BnA addition increased; the signal reached 6.33 ppm at 50 mol% BnA and 5.67 ppm at 100 mol% BnA (Figure 2.2b). These changes can be attributed to the strong shielding of ammonium moiety of MA<sup>+</sup> by BnA reagent. In contrast, the addition of ANI to the MAPbBr<sub>3</sub> precursor did not cause any shift. Even high concentrations of ANI did not cause a noticeable chemical shift of the proton signal of MA (Figure 2.2c); this lack of effect



indicates that the solution with ANI remained as a mixture without causing a chemical reaction even though ANI has the same molecular structure as BnA except the methylene bridge ( $-\text{CH}_2$ ) between the amine and the benzene ring. The integration ratio ( $I$ ) of proton signals ( $H_{\text{ammonium}}/H_{\text{alkyl}}$ ) increased from 1 for pristine MAPbBr<sub>3</sub> to 1.81 for MAPbBr<sub>3</sub> with 100 mol% of BnA (Figure 2.3). This change indicates the presence of a strong interaction that represents an increased hydrogen bond strength by sharing a proton between BnA and MA<sup>+</sup>. In contrast, MAPbBr<sub>3</sub> with 100 mol% ANI had  $I$  around 1 implying that ANI does not interact with MA<sup>+</sup>.

This different effects of BnA and ANI on the chemical behaviour can be explained by the Brønsted–Lowry acid–base reaction. BnA is a strong base, so a proton from the ammonium group of MA<sup>+</sup> which is a weak acid, can be transferred to nitrogen of BnA to yield BnA<sup>+</sup>. In contrast, ANI is a weak base, so cannot extract a proton from MA<sup>+</sup>. To learn the cause of this difference, we calculated the electron densities of BnA and ANI with the first-principles density functional theory (DFT). The resultant contour plots of the electron density of each molecule and its integrated profiles along the  $b$ -axis direction are presented (Figure 2.2d, e). The calculated results indicate that BnA has a much higher electron density on the terminal amine moiety than ANI, because the methylene bridge on BnA can donate more electrons to the more-electronegative nitrogen and localise the electrons on the nitrogen leading to an inductive effect. ANI, in contrast, has electrons that are delocalized between the nitrogen and the benzene ring governed by a resonance effect, which makes ANI much less basic than BnA. As a consequence of these differences, the protonation tendency from MA<sup>+</sup> to BnA is  $5.5 \times 10^4$  times stronger than from MA<sup>+</sup> to ANI.



The absorption characteristics of the solid-state perovskite films from the corresponding precursors support this result (Figure 2.2f, g): the excitonic peak of the MAPbBr<sub>3</sub> absorption spectrum at 525 nm changes significantly according to the amount of BnA added, but does not shift with the addition of ANI regardless of the amount. For example, addition of 30 mol% BnA resulted in new excitonic peaks at 399 nm and 430 nm, which can be assigned to a phase with  $n = 1$  and 2, respectively, indicating the formation of 2D perovskites<sup>[18–20]</sup>.

Interestingly, the film obtained using a precursor with 100 mol% of BnA showed the spectrum of a typical 2D perovskite film that has an excitonic peak at 399 nm; this peak is the result of the strong proton-withdrawing tendency of BnA which takes protons from MA<sup>+</sup> and participates in the formation of 2D perovskite (Figure 2.2h). Furthermore, we predicted the importance of the protonation of BnA by performing first-principles molecular dynamics (MD) simulations in which perovskite lattice including the protonated BnA (BnA<sup>+</sup>) showed much greater structural stability than that with neutral BnA. (Figure 2.4). Also, we performed the solid-state magic-angle-spinning (MAS) NMR spectroscopy to gain an atomic-level insight about the formation of crystalline perovskite (Figure 2.5). The result confirmed that the protonated BnA composed the solid-state crystalline perovskite while ANI did not participate in the formation of perovskite.



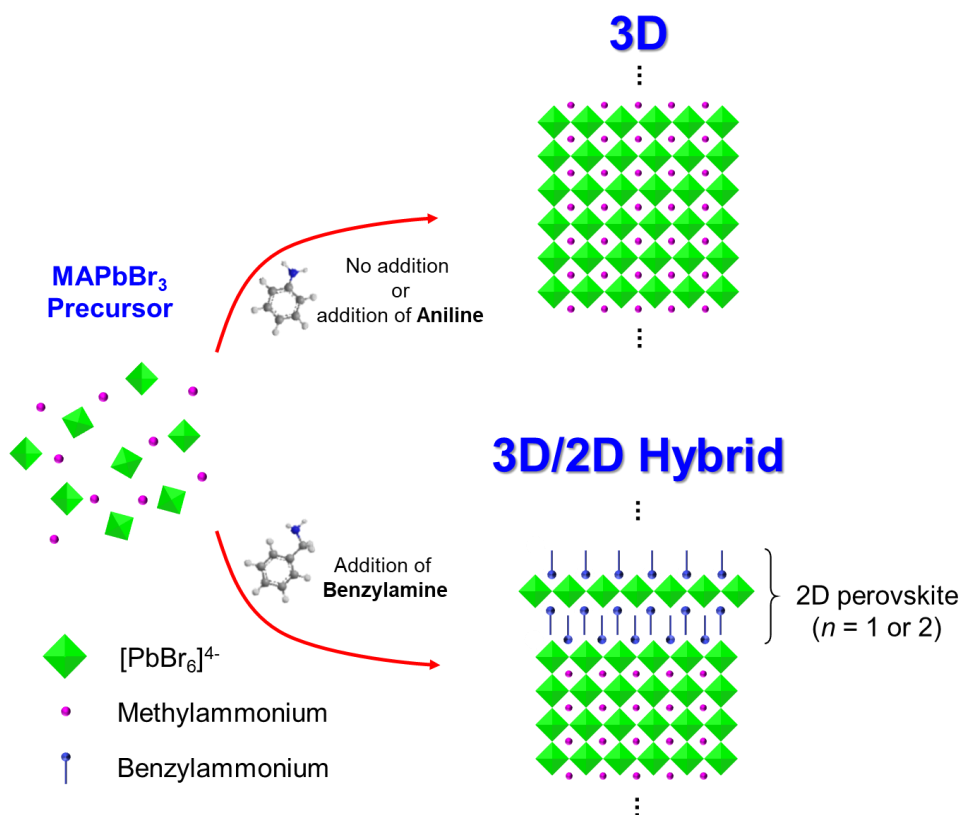


**Figure 2.1** Principal scheme of our study. The neutral reagent, benzylamine (BnA) leads to the formation of 3D/2D hybrid perovskites while aniline (ANI) does not induce the formation of 2D perovskites.



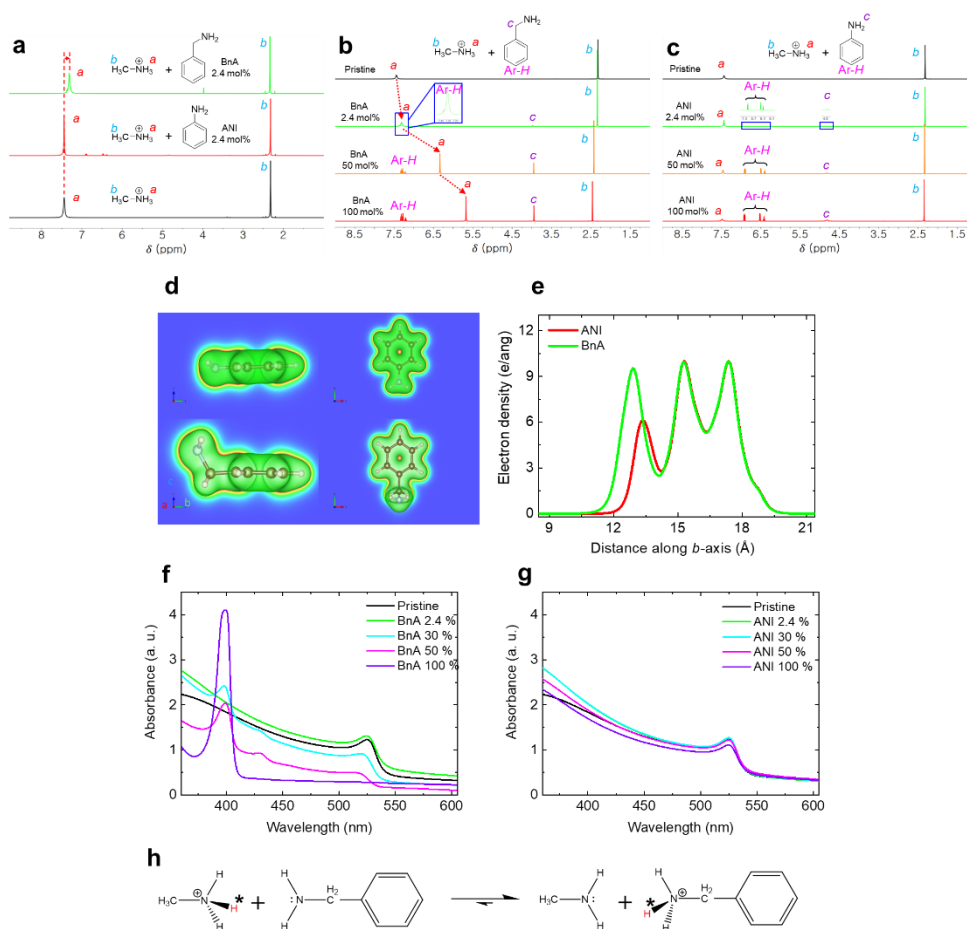


**Figure 2.2** Proton-transfer induced 2D perovskite formation with BnA. **a**  $^1\text{H}$  NMR spectra of MAPbBr<sub>3</sub> precursor solutions in DMSO-*d*<sub>6</sub> according after addition of additives. Pristine MAPbBr<sub>3</sub> (black), MAPbBr<sub>3</sub> with 2.4 mol% of ANI (black) and MAPbBr<sub>3</sub> with 2.4 mol% of BnA (green). **b**, **c**  $^1\text{H}$  NMR spectra according to the different amount of BnA and ANI addition. **d** Electron density contour plots of BnA (bottom) and ANI (top) with an iso-surface of  $0.03 \text{ e} \cdot \text{\AA}^{-3}$ . **e** Integrated electron density profile for BnA (green) and ANI (red) along with *b*-axis in **d**. **f**, **g** Absorption spectra of MAPbBr<sub>3</sub> thin film according to the addition of BnA and ANI. **h** Proton-transfer reaction between MA and BnA.



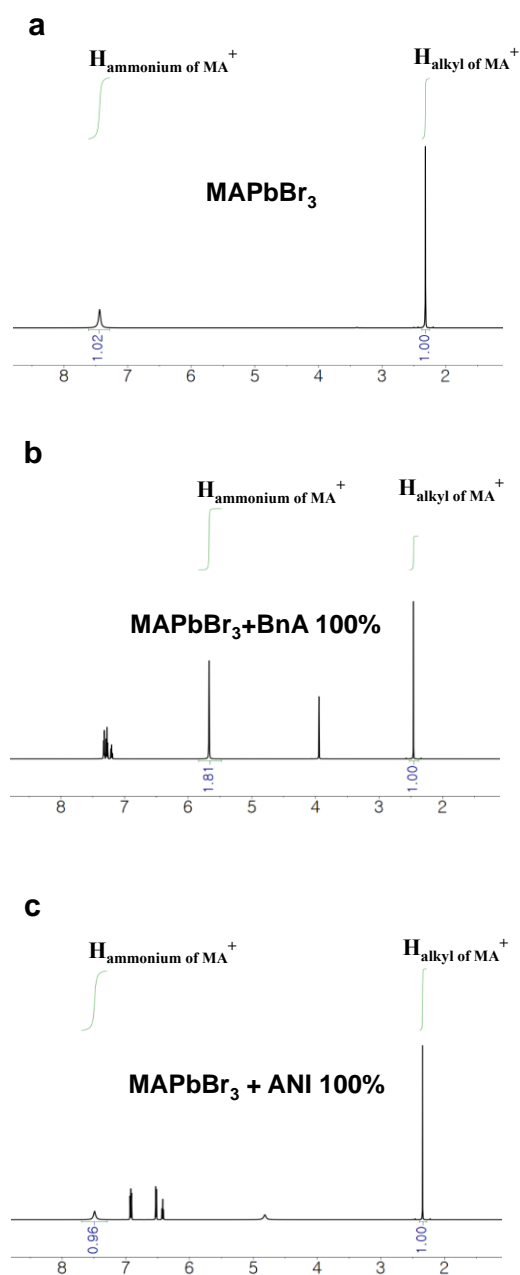


**Figure 2.3**  $^1\text{H}$  NMR spectra of MAPbBr<sub>3</sub> solution (a) without additive, (b) with BnA 100 mol%, and (c) ANI 100 mol%.



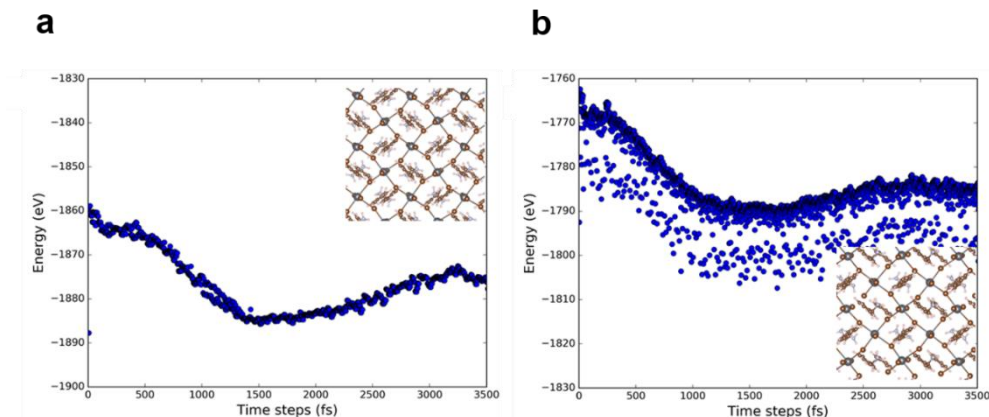


**Figure 2.4** Fluctuations of total energy as the evolution of simulation time and the snapshots of atomic configurations after the first-principles molecular dynamics (MD) simulations (3.5 ps) with a time step of 1.2 fs at the temperature of 300 K. **a** and **b** for the 2D perovskites formed by protonated BnA ( $\text{BnA}^+$ ) and unprotonated BnA, respectively. First-principles molecular dynamics (MD) simulations presented the importance of proton-transfer. We utilized a  $2\sqrt{2} \times 2\sqrt{2} \times 1$  supercell to compare thermal fluctuation behaviors of perovskite lattice including protonated or unprotonated BnA at 300K. The atoms in the 2D perovskite formed by the protonated BnA ( $\text{BnA}^+$ ) only slightly vibrate around their equilibrium positions and show steady energy fluctuations, which suggests that the 2D structure is well maintained. On the contrary, the 2D perovskite formed by the unprotonated BnA showed highly significant oscillations of the fluctuations of total energy, which indicates the intrinsic instability of the system. This result supports the importance of the protonation which enables  $\text{BnA}^+$  to form a strong bond in the lattice and implies that the incorporation of the protonated BnA ( $\text{BnA}^+$ ) can lead to effective passivation since it can maintain the 3D/2D hybrid structure without forming defects in the lattice.



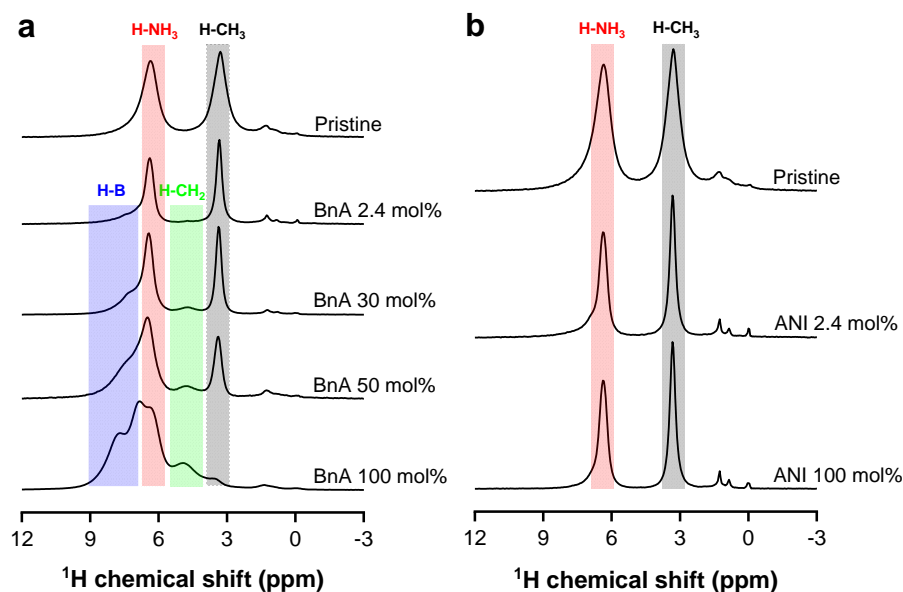


**Figure 2.5** The  $^1\text{H}$  MAS NMR spectra for the solid-state perovskites with varying **a** BnA concentration (0, 2.4, 30, 50 and 100%) and **b** ANI concentration (0, 2.4, and 100%) under a fast spinning speed of 40 kHz at 14.1 T. The pristine sample showed two dominant  $^1\text{H}$  peaks at 6.36 ppm and 3.30 ppm which can be assigned to the hydrogens in  $\text{NH}_3$  ( $\text{H-NH}_3$ ) and  $\text{CH}_3$  ( $\text{H-CH}_3$ ) of  $\text{MA}^+$ , respectively. With the addition of BnA, the spectrum had two more peaks that arose from the hydrogens bonded to the benzene ring ( $\text{H-B}$ ) and in  $\text{CH}_2$  ( $\text{H-CH}_2$ ) of  $\text{BnA}^+$ . The positions of  $\text{H-B}$  varied in the range of approximately 6.7 to 8 ppm and the peak of  $\text{H-CH}_2$  was at around 4.8 ppm. The  $^1\text{H}$  peak intensity of  $\text{H-CH}_3$  decreased with an increase in BnA concentration because  $\text{MA}^+$  is deprotonated to be methylamine which can be easily evaporated during the film annealing process. Meanwhile, the peak intensities of  $\text{H-B}$ ,  $\text{H-NH}_3$ , and  $\text{H-CH}_2$  gradually increased confirming that the protonated BnA composes the solid-state crystalline perovskite. Upon the addition of ANI, in contrast, the peak positions of  $\text{H-NH}_3$  and  $\text{H-CH}_3$  were invariant indicating ANI did not participate in the formation of perovskite.



## Crystal structure and configuration of perovskites

To examine the detail of perovskite crystal structures and dimensionality, we performed grazing-incidence X-ray diffraction (GIXD) on the perovskite films. The results confirmed that BnA contributed to the formation of 2D perovskite but that ANI did not; this result is consistent with the conclusions drawn from the  $^1\text{H}$ NMR analysis and optical absorption spectra. The films of 3D pristine  $\text{MAPbBr}_3$  and  $\text{MAPbBr}_3$  with 2.4 mol% ANI showed similar diffraction patterns; this result indicates that the ANI does not influence the perovskite crystal structure. In contrast, the addition of 2.4 mol% BnA led to an appearance of additional peaks at low angles; the most dominant one was at  $2\theta = 5.32^\circ$  (Figure 2.7). The newly appeared peak can be assigned to a 2D perovskite with the lattice plane spacing of 16.58 Å according to Bragg's equation, which corresponds to  $\text{BnA}_2\text{PbBr}_4$  with  $n = 1$ . The information about the crystal structure of perovskite also can be shown in 2D GIXD patterns (Figure 2.6a-c). It is clear that the  $\text{MAPbBr}_3$  film with 2.4 mol% BnA had an additional X-ray reflection ring at scattering vector  $Q = 0.38 \text{ \AA}^{-1}$ ; this is a consequence of the 2D phase. In contrast, the  $\text{MAPbBr}_3$  with 2.4 mol% ANI had the same pattern as the pristine film of 3D phase. It is worth noting that  $\text{MAPbBr}_3$  with BnA retained the diffraction patterns of 3D phase; i.e., 3D  $\text{MAPbBr}_3$  and 2D  $\text{BnA}_2\text{PbBr}_4$  coexisted in the film, which can be called 3D/2D hybrid perovskite. Ring-shaped diffraction patterns with a uniform intensity indicate a random orientation and can be attributed to a nanocrystal pinning process that renders grains small by rapid crystallization of perovskite; such small grains can induce an efficient radiative recombination<sup>2,35–37</sup>. An increase in the ratio of BnA to 30 mol% increased



the intensity of the signal of the 2D perovskite phase, whereas the increase in the amount of ANI addition did not cause the formation of any other phase while maintaining 3D phase (Figure 2.7).

The addition of BnA caused an apparent change in the film morphology of perovskites. The films of pristine MAPbBr<sub>3</sub> and MAPbBr<sub>3</sub> with 2.4 mol% ANI had a similar columnar grain structure, whereas 3D/2D hybrid perovskite film with 2.4 mol% BnA had granular grains with a smaller size (Figure 2.6d). This is because the growth of 2D perovskite can decrease the growth rate of 3D perovskite leading to the formation of a smaller granular type of grains, which can be beneficial to efficient exciton confinement within a grain<sup>2,35</sup>. The morphology of 3D/2D hybrid perovskite films with BnA showed a strong dependence on the amount of BnA (Figure 2.8). However, addition of even a large amount of ANI had little influence on the morphology of MAPbBr<sub>3</sub> film.



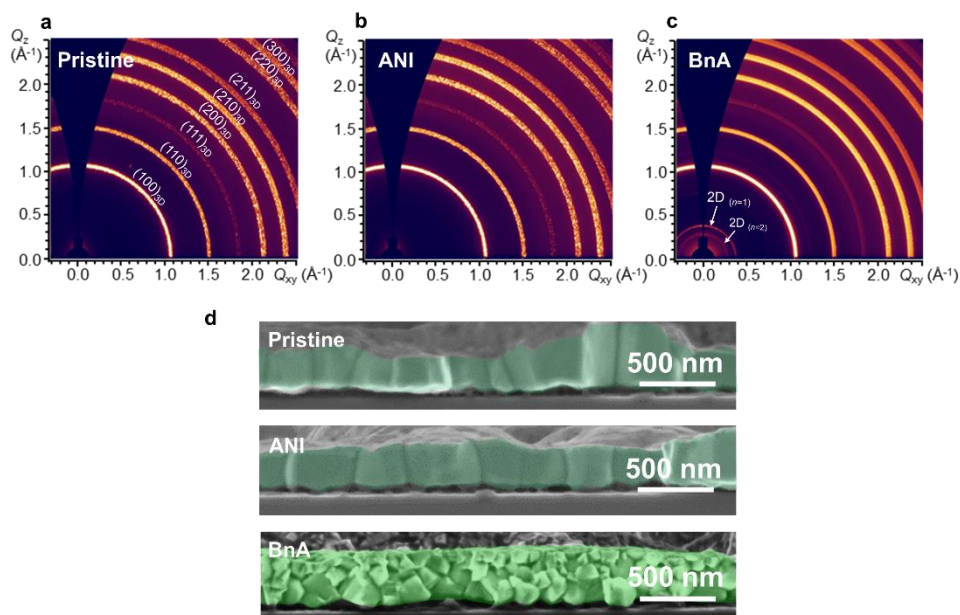


**Figure 2.6** Crystal structure and morphology of MAPbBr<sub>3</sub> according to the addition of ANI or BnA. **a-c** 2D GIXD patterns of pristine MAPbBr<sub>3</sub>, MAPbBr<sub>3</sub> with 2.4 mol% ANI, and 2.4 mol% BnA. **d** Cross-sectional SEM images of pristine MAPbBr<sub>3</sub> (top), MAPbBr<sub>3</sub> with 2.4 mol% ANI (middle) and 2.4 mol% BnA (bottom).



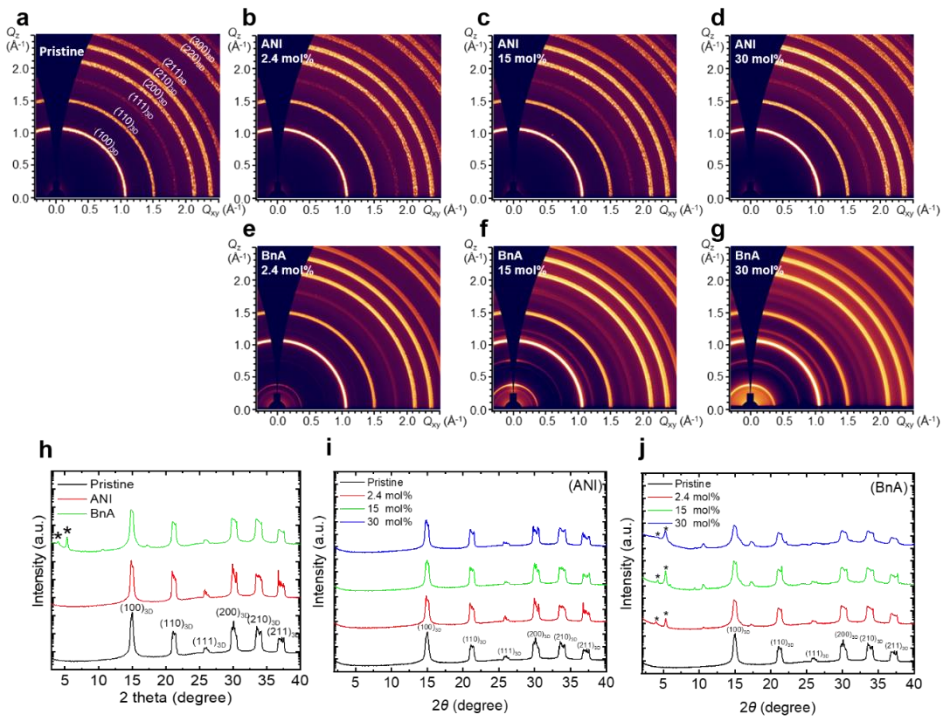


**Figure 2.7** 2D GIXD patterns of **a**, pristine MAPbBr<sub>3</sub> film, **b**, with ANI 2.4 mol% , **c**, ANI 15 mol% , **d**, ANI 30 mol% , **e**, BnA 2.4 mol% , **f**, BnA 15 mol% , and **g**, BnA 30 mol% . 1D XRD profiles of pristine MAPbBr<sub>3</sub> film, MAPbBr<sub>3</sub> with ANI 2.4 mol% and BnA 2.4 mol% (**h**). 1D XRD profiles of MAPbBr<sub>3</sub> with different amounts of ANI (**i**) and BnA (**j**). Traces have been offset vertically for clarity.



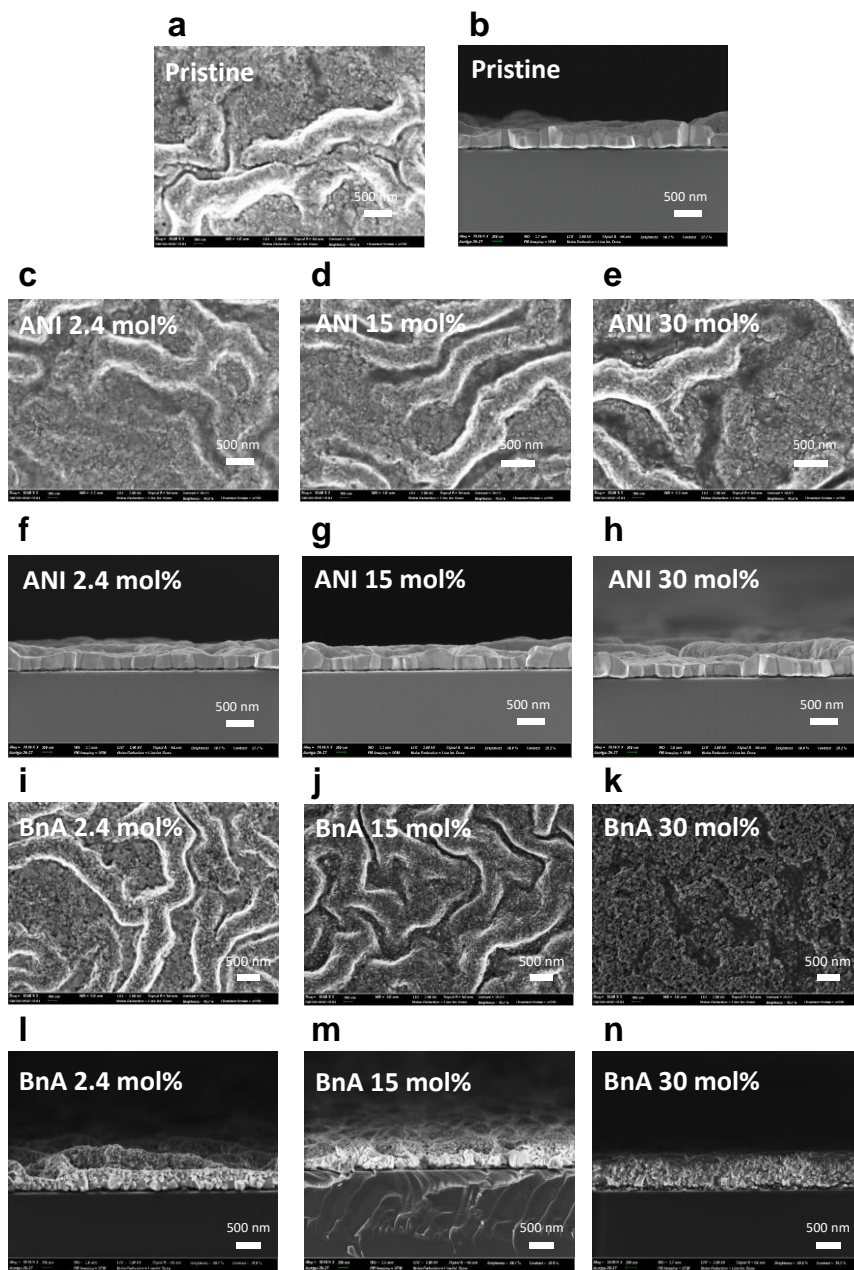


**Figure 2.8** Scanning electron microscopic images (SEM) of MAPbBr<sub>3</sub> perovskite films. **a**, Top-view and **b**, cross-sectional view of pristine MAPbBr<sub>3</sub>, **c-e**, top-view and **f-h**, cross-sectional view with different amount of ANI, **i-k**, top-view, and **l-n**, cross-sectional view with different amounts of BnA.



### Improvements in PL characteristics and trap passivation

We investigated photoluminescence (PL) characteristics of the 3D and the 3D/2D hybrid perovskite films. The perovskite films were prepared on a glass substrate/buffer hole-injection layer (Buf-HIL), which consists of poly(3,4-ethylenedioxythiophene) polystyrene sulfonate (PEDOT:PSS) and perfluorinated ionomer. In steady-state PL measurement, the 3D/2D hybrid perovskite film with 2.4 mol% BnA showed a much higher PL intensity than the 3D perovskite film, whereas addition of 2.4 mol% ANI caused significant PL quenching (Figure 2.9a). Also, the transient PL measurement of the films resulted in the same trend as in the steady-state PL (Figure 2.9b). The PL average lifetime  $\tau_{Ave}$  was more than four times longer in 3D/2D hybrid perovskite film ( $\tau_{Ave} = 254.4$  ns) than in pristine 3D film ( $\tau_{Ave} = 60.94$  ns), but the film with ANI showed considerably shortened PL lifetime ( $\tau_{Ave} = 24.71$  ns). We summarized the detailed decay parameters based on bi-exponential decay function in Table 2.1.

Condition	$A_1$	$\tau_1$ [ns]	$A_2$	$\tau_2$ [ns]	$\tau_{Ave}$ [ns]	$\chi^2$
Pristine	326.3	119.2	540.6	25.8	60.94	0.967
ANI	438	37.8	463.0	12.3	24.71	0.997
BnA	354.0	487.6	480.8	82.7	254.4	1.048

**Table 2.1** Bi-exponential decay function,  $y = A_1e^{-t/\tau_1} + A_2e^{-t/\tau_2}$  fitted results of PL lifetime curves of pristine, 2.4 mol% ANI-added, and 2.4 mol% BnA-added MAPbBr<sub>3</sub> films on Quartz/Buf-HIL substrates.



We realized that 2.4 mol% BnA did not cause a shift in the peak position compared to the PL of 3D MAPbBr<sub>3</sub> at 543 nm, or cause the formation of 2D perovskite PL emission peaks. These observations indicate that the radiative recombination occurs only in the 3D perovskite rather than in the 2D perovskite, which can be attributed to the energy cascade that results from the difference in the dimensionality between perovskite phases in the 3D/2D hybrid structure (Figure 2.9c, d)<sup>33,38</sup>. Only the addition of the larger amount of BnA caused a blue-shift of PL emission (to 537 nm for 30 mol% and to 530 nm for 50 mol%), accompanied by the appearance of 2D perovskite PL emissions at 405 nm and 435 nm, which can be assigned to  $n = 1$  and 2, respectively. The further addition of BnA up to 100 mol% which corresponds to the same amount as MA, caused a dramatic increase in the intensity of PL emission at 409 nm from 2D perovskite. This shift can be more clearly seen in normalized PL spectra (Figure 2.9d). We also measured the absolute PL quantum efficiency (PLQE) which showed a similar trend to the steady-state PL intensity according to the amount of BnA (Figure 2.10). On the other hand, increasing the amount of ANI only decreased the PL intensity, and did not shift the emission wavelength, which can be attributed to intensive non-radiative recombination due to the electron deficiency of ANI (Figure 2.11)<sup>39</sup>.

Also, we showed that alignment of energy bands contributes to the improvement in PL properties of the 3D/2D hybrid perovskite film based on ultraviolet photoemission spectroscopy (UPS) analysis (Figure 2.12, 2.13). We further investigated the carrier confinement effect in the perovskites by performing the excitation density dependent PL measurement at room temperature (Figure 2.14). In the excitation density range of  $10^{15}$  to  $10^{18}$  cm<sup>-3</sup> which corresponds to the operation



regime of LEDs, The integrate PL ( $PL_{\text{int}}$ ) follows a power-law dependence on the excitation density,  $n_{\text{ex}}$  as  $PL_{\text{int}} \propto n_{\text{ex}}^k$  where the 3D perovskite had  $k = 1.30$  indicating the co-existence of excitons (monomolecular emission) and free carriers (bimolecular emission) while the 3D/2D hybrid perovskite film showed  $k = 1.08$  indicating the predominant excitonic character by monomolecular recombination, which can be attributed to the effective carrier confinement.



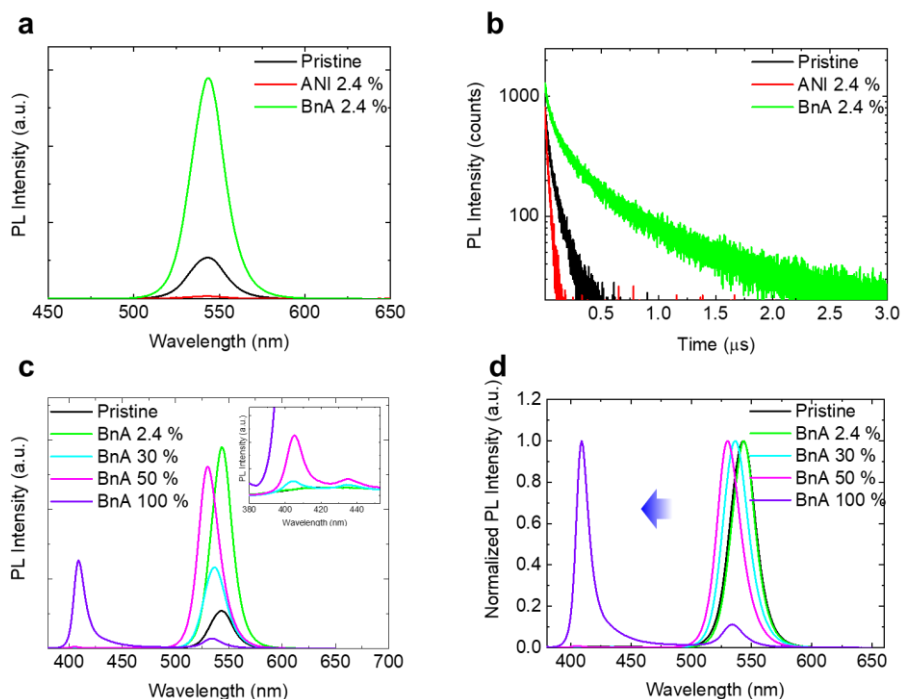


**Figure 2.9** PL characteristics of perovskites and the trap passivation. **a**, PL spectrum of pristine MAPbBr<sub>3</sub> film (black), film with 2.4 mol% of ANI (red), and 2.4 mol% of BnA (green)mol%. **b**, PL lifetime curves of pristine MAPbBr<sub>3</sub> film (black), film with 2.4 mol% of ANI (red), and 2.4 mol% of BnA (green). **c**, PL spectra of MAPbBr<sub>3</sub> film with different amount of BnA and magnified PL spectra at low wavelength region (inset). **d**, Normalized PL spectra of MAPbBr<sub>3</sub> film with different amount of BnA.



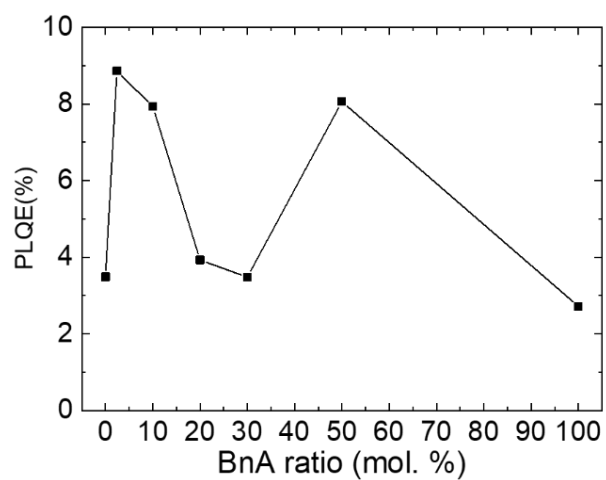


**Figure 2.10** PLQE of MAPbBr<sub>3</sub> film according to the amount of BnA addition. The films were excited with a continuous-wave 405 nm laser diode (2.5 mW cm<sup>-2</sup>).



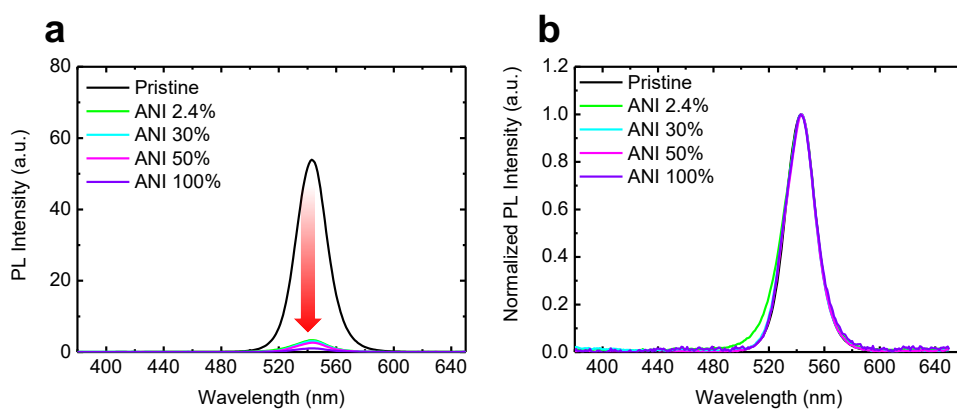


**Figure 2.11** **a**, Steady-state PL spectra and **b**, normalized PL spectra of MAPbBr<sub>3</sub> film with different amounts of ANI.



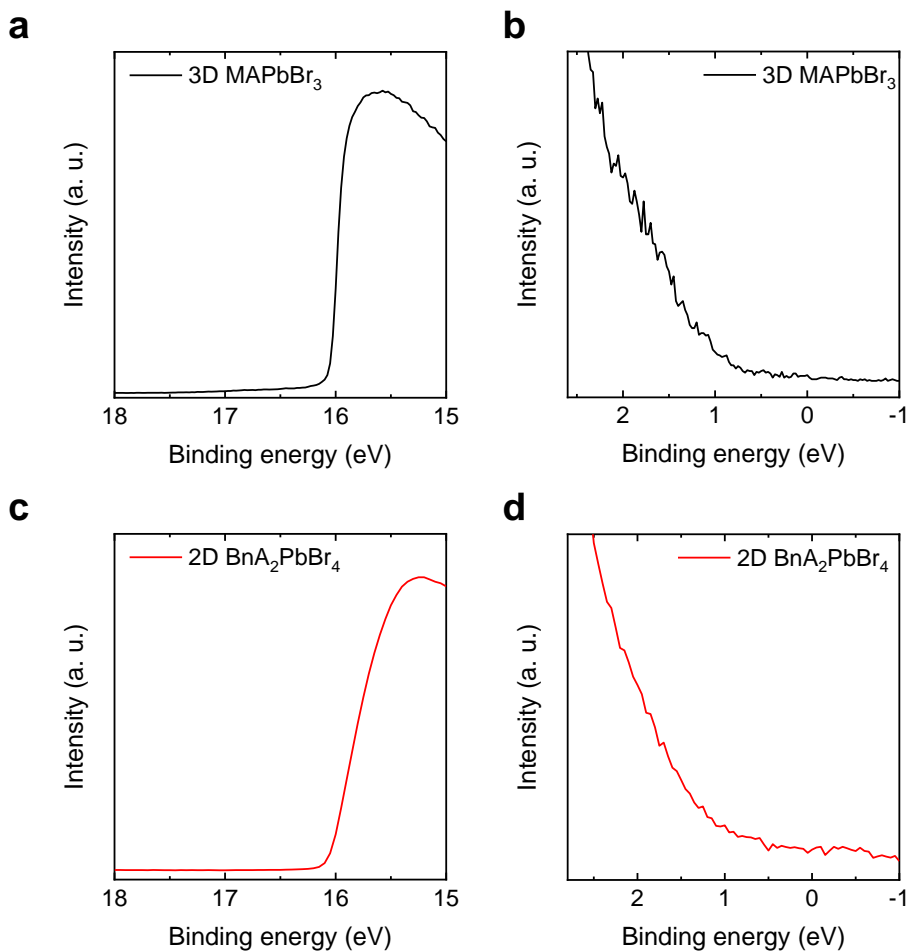


**Figure 2.12** a-b, UPS spectra of 3D MAPbBr<sub>3</sub> and c-d, 2D BnA<sub>2</sub>PbBr<sub>4</sub> films showing secondary cut-off (left column) and onset (right column).



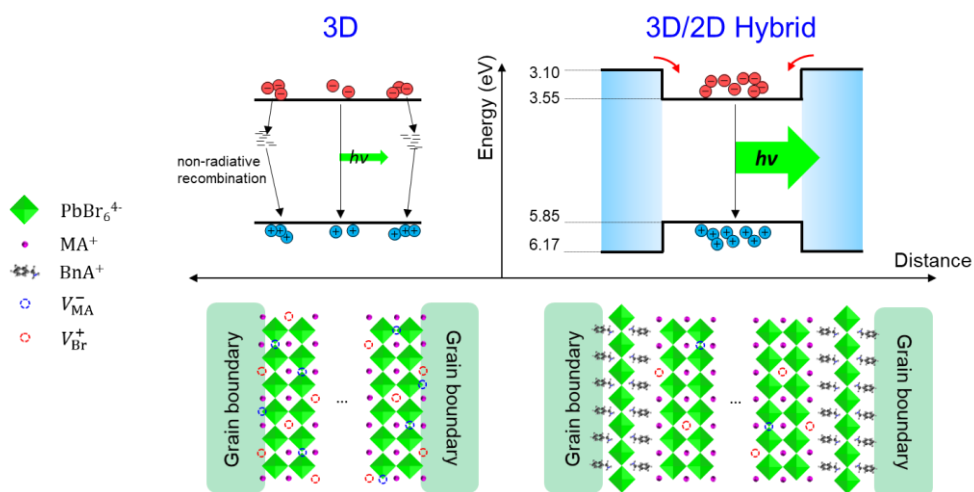


**Figure 2.13** Energy band structure of 3D and 3D/2D hybrid perovskites based on UPS result showing recombination behaviour (top) based on the configurations of grain and GB of each perovskite.



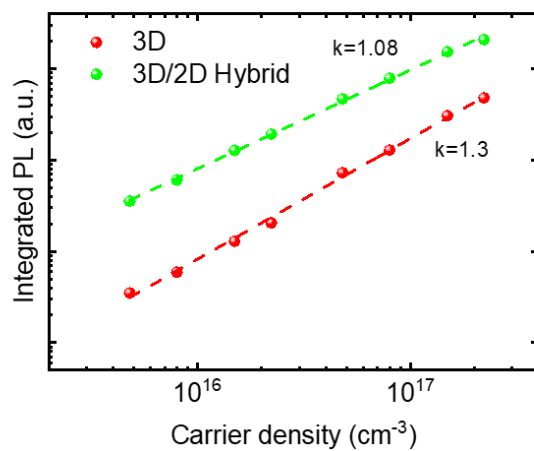


**Figure 2.14** Integrated PL as a function of the excitation density of 3D and 3D/2D hybrid perovskites.



To deeply understand the trap passivation effect by using 3D/2D hybrid perovskite, we investigated temperature-dependent steady-state PL characteristics of the perovskite films from 70 K to 300 K. The 3D perovskite film showed two distinct PL emission peaks at low temperatures below 130 K (Figure 2.15a). While the sharp PL peaks with higher energy can arise from band-edge (BE) emission, the broad PL band with lower energy can be attributed to shallow trap states induced by structural disorder in the orthorhombic phase of MAPbBr<sub>3</sub>. In this temperature regime, the ratio of integrated PL intensity of BE versus the shallow trap-mediated PL emission (TE) was increasing as temperature increased, which implies that thermally-assisted de-trapping of charge carriers occurs (Figure 2.15b and Figure 2.16). To estimate the value of the activation energy to de-trap the charge carriers from the shallow traps, the curve was fitted by the Boltzmann distribution function:

$$y = y_0 e^{(-\frac{E_a}{k_B T})} \quad \text{Equ. (2-1)}$$

where  $k_B$  is the Boltzmann constant and  $T$  is temperature and  $E_a$  is the activation energy to de-trap charge carriers, which resulted in 88.84 meV. In contrast, the 3D/2D hybrid perovskite film only showed a single PL peak of BE without the TE in the whole range of temperature (Figure 2.15c). This indicates that the incorporation of 2D perovskites effectively passivates the shallow trap states even in the orthorhombic phase.

Furthermore, the excitation density dependence of the PL lifetimes revealed defect-related recombination kinetics of the perovskites (Figure 2.15d). We controlled the excited charge carrier density of the perovskite films from  $4.8 \times 10^{15} \text{ cm}^{-3}$  to  $2.2 \times 10^{17} \text{ cm}^{-3}$  (Figure 2.17). We used a rate equation model where the decay



of the excited charge carrier density  $n_0$  can be explained regarding radiative and non-radiative recombination, which can be written as

$$\tau_{\text{PL}} = (A + Bn_0)^{-1} \quad \text{Equ. (2-2)}$$

where  $A$  is non-radiative recombination rate coefficient, and  $B$  is radiative recombination rate coefficient. We found that the 3D/2D hybrid perovskite film exhibited a significantly lower  $A = 6.16 \times 10^5 \text{ s}^{-1}$  than that of 3D perovskite ( $A = 2.96 \times 10^6 \text{ s}^{-1}$ ). This indicates that the 3D perovskite has a high density of non-radiative Shockley–Read–Hall recombination centre which can be associated with certain kinds of ionic defects in the lattice despite a high degree of defect tolerance of perovskite. In contrast, the incorporation of 2D perovskite into 3D perovskite can restrict the defect formation and migration leading to such lowered non-radiative recombination rate coefficient. This is due to the presence of  $\text{BnA}^+$  which has a lower rotational degree of freedom than  $\text{MA}^+$ , which will be discussed in detail in the following section. Meanwhile, the 3D perovskite and the 3D/2D hybrid perovskite showed a similar radiative recombination rate coefficient,  $B$  as  $2.30 \times 10^{-11} \text{ cm}^3 \cdot \text{s}^{-1}$  and  $1.08 \times 10^{-11} \text{ cm}^3 \cdot \text{s}^{-1}$ , respectively. This result well matches with the explanation that the shallow traps mostly disappeared in both perovskites. On the basis of the results of the comprehensive PL analyses, we depicted a schematic of the charge recombination dynamics of 3D and 3D/2D hybrid perovskites (Fig 5e). In the 3D perovskite, the excited charge carriers can be trapped into the shallow traps in the orthorhombic phase, which can be de-trapped by increased thermal energy. Even though the structural stabilization by the phase transition of  $\text{MAPbBr}_3$  can lead to the reduction in the density of the activated shallow trap states, deep level traps associated with ionic defects can still exist and cause non-radiative recombination.



In contrast, 3D/2D hybrid perovskite can have more efficient radiative recombination because the incorporation of 2D perovskite can lead to effective passivation by suppressing the formation and migration of the ionic defects thereby minimizing a loss of charge carrier from quenching by the deep traps.

To verify the reduced density of trap states in 3D/2D hybrid perovskite compared to 3D perovskite, we designed and characterized hole-only devices (HODs) with a structure of ITO /BuF-HIL (50 nm) /Perovskite (400 nm)/ MoO<sub>3</sub> (10 nm)/ Au (100 nm) (Figure 2.15f). The  $I$ - $V$  behaviour of the devices had three regimes defined by slope  $k$ : an Ohmic regime ( $k = 1$ ), a trap-filled limited (TFL) regime ( $k > 3$ ) and a trap-free space charge limited current (SCLC) regime ( $k = 2$ ) as the bias increased<sup>40–42</sup>. Here, trap density  $n_t$  is linearly proportional to trap-filled limit voltage  $V_{\text{TFL}}$  at which a transition of  $I$ - $V$  behaviour from Ohmic to TFL occurs:

$$V_{\text{TFL}} = n_t \frac{eL^2}{2\epsilon\epsilon_0} \quad \text{Equ. (2-3)}$$

where  $e$  is the electron charge,  $L$  is the thickness of the perovskites,  $\epsilon$  is relative dielectric constant (25.5 for MAPbBr<sub>3</sub>), and  $\epsilon_0$  is the vacuum permittivity<sup>43</sup>. In the  $I$ - $V$  curves,  $V_{\text{TFL}}$  was lower in HODs based on 3D/2D hybrid perovskite (0.436 V) than in HODs based on pristine 3D perovskite (0.609 V). Thus, we obtained  $n_t = 9.49 \times 10^{15} \text{ cm}^{-3}$  for 3D/2D hybrid perovskite and  $n_t = 1.33 \times 10^{16} \text{ cm}^{-3}$  for 3D perovskite. This result supports that the formation of 2D perovskite can passivate the trap states of 3D perovskite leading to the efficient radiative recombination. We also calculated the hole mobility  $\mu_h$  of each device by fitting the curves in the regime of trap-free SCLC based on the Mott-Gurney law:



$$J = \frac{9\epsilon\epsilon_0\mu_h V^2}{8L^3} \quad \text{Equ. (2-4)}$$

where  $V$  is applied voltage. The hole mobility of two devices had similar value  $\mu_h$ :  $0.042 \text{ cm}^2 \cdot \text{V}^{-1} \cdot \text{s}^{-1}$  in the HOD with 3D/2D hybrid perovskite, and  $0.049 \text{ cm}^2 \cdot \text{V}^{-1} \cdot \text{s}^{-1}$  in the HOD device with 3D perovskite. This result indicates that the formation of 2D perovskite does not degrade hole transport in the perovskite.



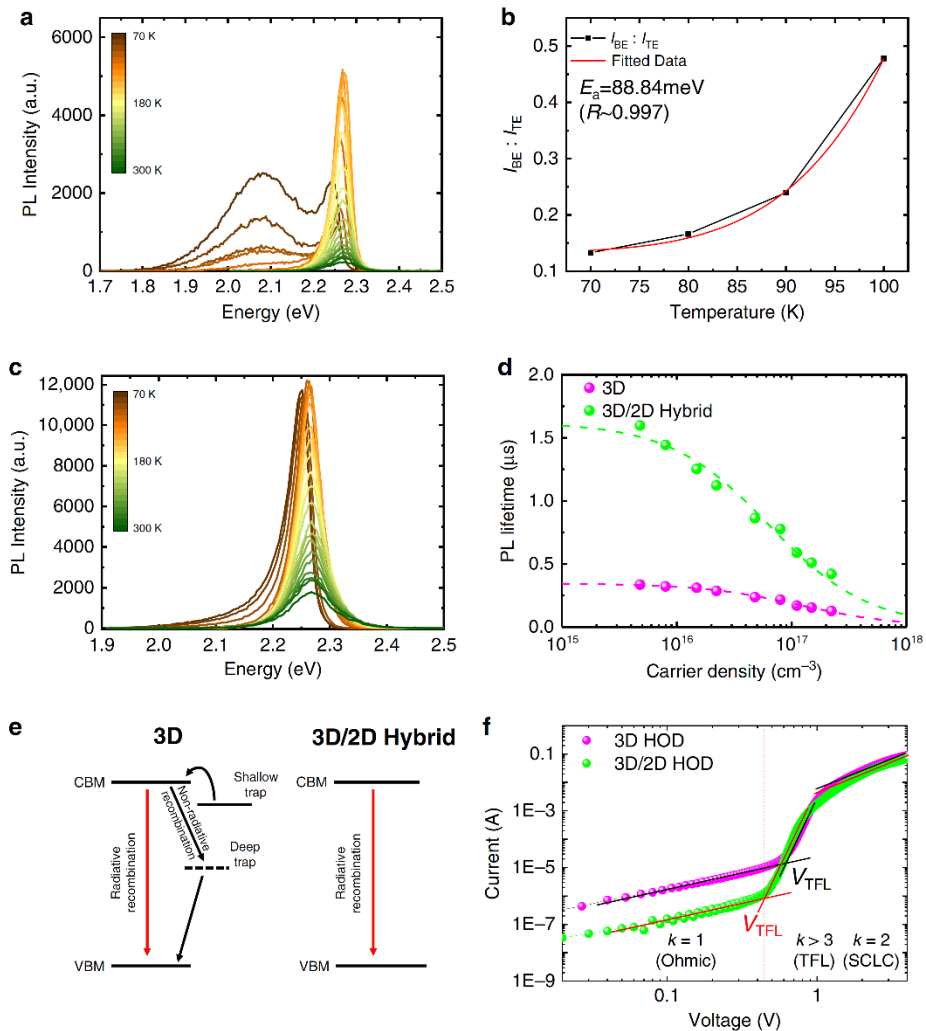


**Figure 2.15** Photo-physical analyses to investigate recombination kinetics and trap states of perovskites. **a** Temperature-dependent PL of 3D perovskite and **b** Ratio between integrated PL of band emission and trap-mediated emission of 3D perovskite as a function of temperature and its fitted curve according to Boltzmann distribution function. **c** Temperature-dependent PL of 3D/2D hybrid perovskite. **d** Excited charge carrier density-dependent PL lifetimes of the perovskites. **e** Schematic of charge carrier recombination dynamics of the perovskites. **f**  $I$ - $V$  curves of hole-only devices with 3D perovskite and 3D/2D hybrid perovskite.



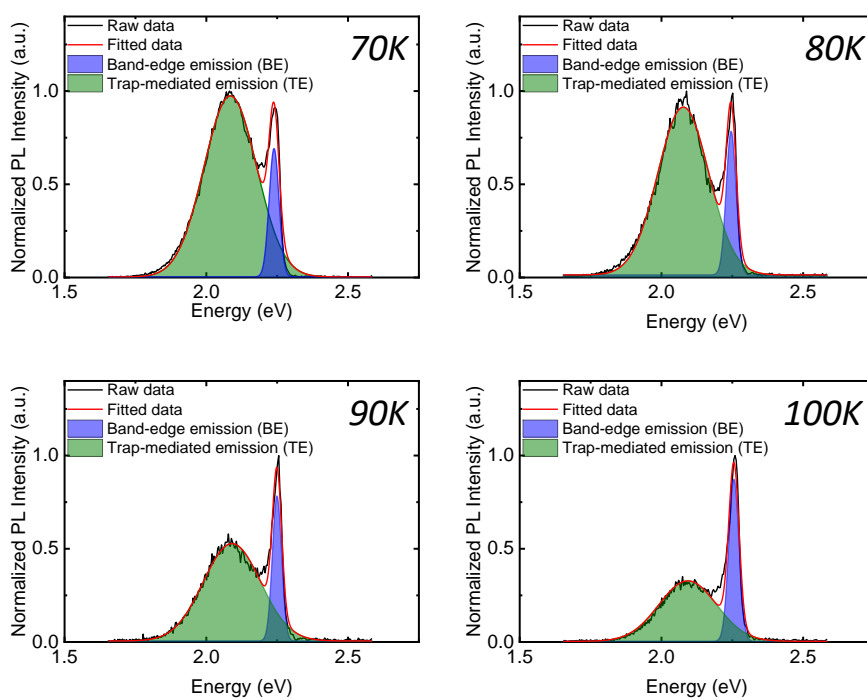


**Figure 2.16** PL emission of 3D perovskite, MAPbBr<sub>3</sub> according to temperature from 70 K to 100 K. The peaks were deconvoluted into band-edge emission and trap-mediated emission.



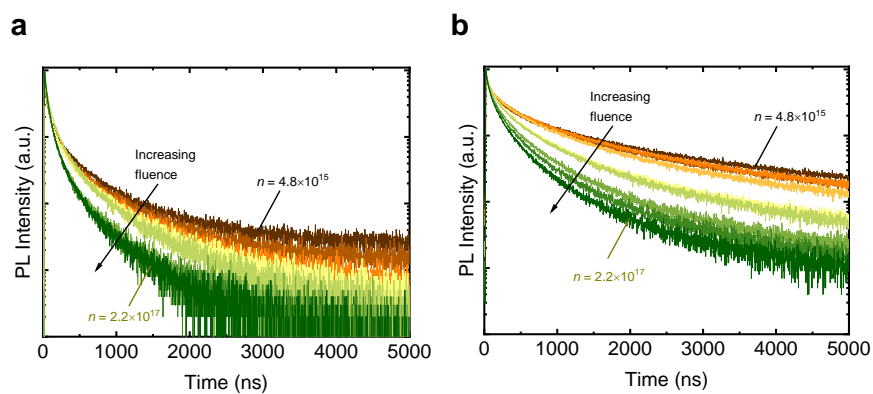


**Figure 2.17** **a**, TCSPC curves of 3D perovskite and **b**, 3D/2D hybrid perovskite as a function of excited carrier density.



## EL characteristics of PeLEDs and ion migration

We used the developed perovskite films as an emitter in PeLEDs. The device structure was FTO/BuF-HIL (50 nm)/Perovskite (400 nm)/2,2',2''-(1,3,5-benzinetriyl)-tris(1-phenyl-1-H-benzimidazole) (TPBi) (50 nm)/LiF (1 nm)/Al (100 nm) (Figure 2.18a). All LED characteristics were significantly improved in the device with the 3D/2D hybrid perovskite emitter compared to those of the device with the 3D perovskite emitter. The 3D/2D PeLED had maximum current efficiency  $CE_{\max} = 20.55 \text{ cd} \cdot \text{A}^{-1}$ , and external quantum efficiency  $EQE_{\max} = 4.23 \%$ , which are both higher than in the 3D PeLED ( $CE_{\max} = 13.23 \text{ cd} \cdot \text{A}^{-1}$  and  $EQE_{\max} = 2.50 \%$ ) (Figure 2.18b-e). Both devices had same normalized EL emission spectra, which is consistent with the result of PL spectra (Figure 2.18f). Devices were optimized by adjusting the amount of BnA (Figure 2.19). We attribute the improvement in EL of 3D/2D hybrid PeLED to the efficient exciton confinement and the reduced defect-assisted recombination that result from passivation of trap sites by the formation of 2D perovskite. The effective suppression of ion migration by the 3D/2D hybrid perovskite structure can also contribute to the EL improvement because charge carriers can result in emission of light instead of going through non-radiative recombination by the ionic space charges that are distributed at the vicinity of perovskite interfaces. In contrast, the use of ANI-added perovskite film degraded the LED characteristics due to significant non-radiative recombination by the electron-deficient ANI as well as by the ionic space charges at the interfaces with the perovskite emitting layer (Figure 2.20).



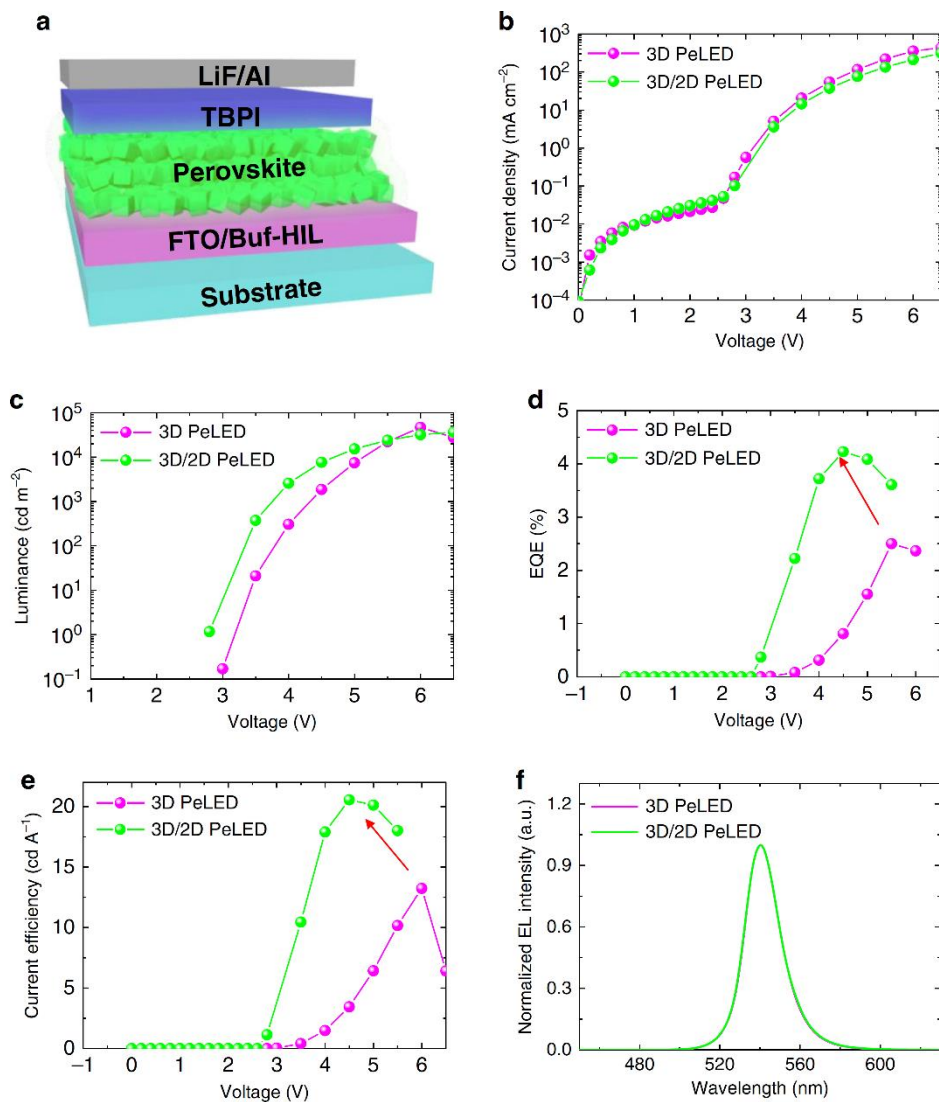


**Figure 2.18** EL characteristics of PeLEDs. **a** Device structure of PeLEDs. **b** Current density of PeLEDs as a function of applied voltage. **c** Luminance of PeLEDs as a function of applied voltage. **d** External quantum efficiency (EQE) of PeLED as a function of applied voltage. **e** Current efficiency (CE) of PeLEDs as a function of applied voltage. **f** Normalized EL spectra of PeLEDs.



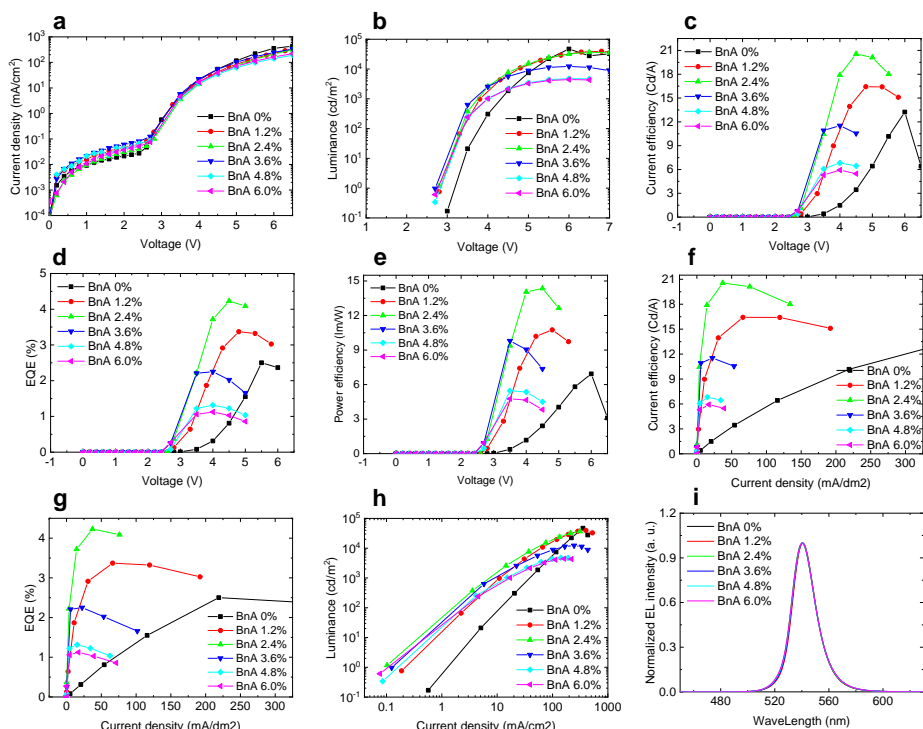


**Figure 2.19** Current-voltage-luminance characteristics of PeLEDs with various mol. % of BnA molecules. **a**, Current density, **b**, Luminance, **c**, current efficiency, **d**, external quantum efficiency (EQE), **e**, power efficiency of PeLEDs as a function of voltage. **f**, Current efficiency, **g**, EQE, **h**, luminance of PeLEDs as a function of current density. **i**, Normalized PL spectra of PeLEDs with various mol% of BnA.



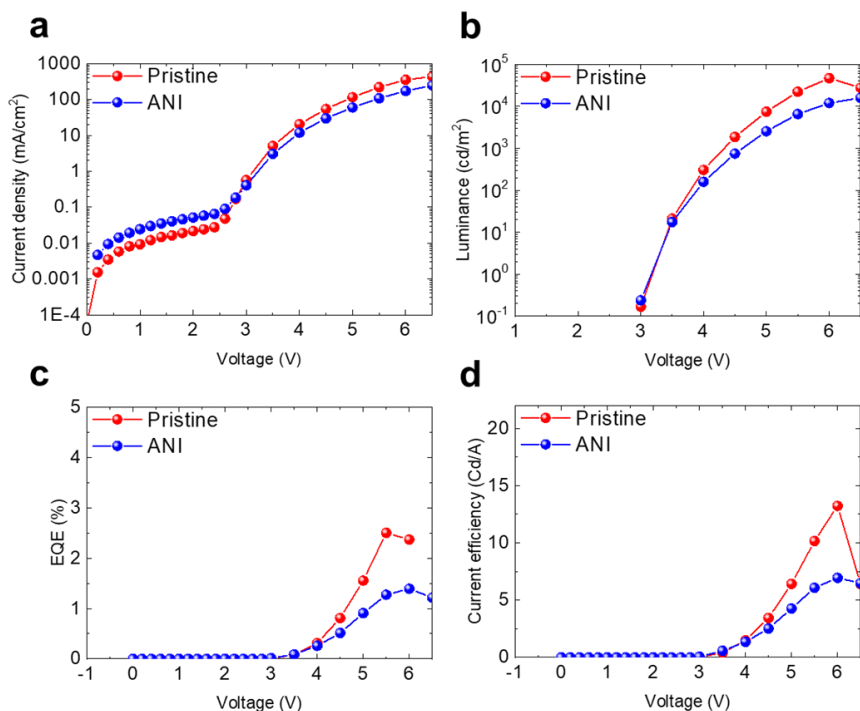


**Figure 2.20** EL characteristics of PeLEDs using pristine MAPbBr<sub>3</sub> emitter (red) and 2.4 mol % ANI added MAPbBr<sub>3</sub> emitter (blue). **a**, Current density of PeLEDs as a function of the applied voltage. **b**, Luminance of PeLEDs as a function of the applied voltage. **c**, External quantum efficiency (EQE) of PeLED as a function of the applied voltage. **d**, Current efficiency (CE) of PeLEDs as a function of the applied voltage.



To verify that there is a different behaviour regarding ion migration between 3D/2D hybrid and 3D PeLEDs, we observed a time-dependent change in current under constant voltage (CV), and time-dependent change in voltage under constant current (CC). Under CV of 3.5 V, the 3D/2D hybrid PeLED maintained relatively stable current during measurement (Figure 2.21a); this result is a consequence of suppressed ion migration, so the local electric field at the interfaces remains mild. In contrast, the 3D PeLED showed severe overshoot of current during the initial stage of the measurement; we attribute this phenomenon to rapidly-facilitated charge injection that occurs because the accumulated ions at the interfaces cause narrowing of the depletion region width or lowering of the injection barrier<sup>44</sup>.

We also examined a voltage change of PeLEDs by varying the applied CC from 0.16 to 2.22 mA·cm<sup>-2</sup> step-wise by repeating switching on and off (Figure 2.21b, c). The 3D/2D hybrid PeLED showed stable plateaus of voltage; this phenomenon proves that the device does not suffer severely from ion migration and accumulation. In contrast, the 3D PeLED showed a voltage undershoot at the beginning of each step, then recovery after the saturation threshold of ion migration. The undershoot of voltage can be explained by the facilitated charge injection, which instantly decreases the built-in potential of the device. The time to reach the saturation threshold of ion migration decreased from 25 s to 5 s as CC was increased from 0.16 to 1.11 mA·cm<sup>-2</sup>, but the further increase in CC did not cause undershoot in voltage; this result indicates that the migration can be accelerated by increasing the applied current. Magnification (Figure 2.21c) of a part of the steps with the CC of 1.11 mA·cm<sup>-2</sup> clearly shows the difference in the stabilities of the devices and peculiar behaviour of the 3D PeLED.



To understand the behaviour of ion migration, we investigated the frequency-dependent capacitance of both types of PeLED in darkness (Figure 2.21d). Both devices showed similar capacitance curves in the frequency range  $100 \text{ Hz} \leq f \leq 1 \text{ MHz}$ , in which capacitance is a result of geometric parameters and dipolar polarization, but 3D PeLED showed increasing capacitance at  $f < 100 \text{ Hz}$ . This additional capacitance may originate from mobile ions that accumulate at contact interfaces because of the severe ion migration<sup>45,46</sup>. The 3D/2D hybrid PeLED did not show the additional capacitance; this result indicates that ion migration was effectively suppressed.

Here, we propose possible pathways of ion migration in 3D and 3D/2D hybrid perovskite and a mechanism of ion migration suppression in the latter (Figure 2.21e). The diffusion barrier energy within the 3D bulk region (Figure 2.21e, red) can be considered similar in both systems because they have similar formation energy of ion defects in the 3D bulk. However, the barrier energy for ion diffusion becomes highly different when the migrating ions reach the GB, where ion migration most easily occurs (Figure 2.21e, green). In 3D perovskite, the ions can reach the GB without being required to diffuse across the 2D perovskite barrier layer. In 3D/2D hybrid perovskite, on the contrary, the ions should overcome the higher barrier energy to get over the organic capping in 2D perovskite region (Figure 2.21e, purple). Also, the 3D/2D hybrid perovskite can effectively suppress the ion migration due to the morphological advantage observed by scanning electron microscopy (SEM) images (Figure 2.3d). As the ion migration mostly occurs on grain boundaries (GBs), mobile ions have to migrate much longer pathway in the granular-like 3D/2D hybrid perovskite than in the columnar-like 3D perovskite (Figure 2.22). Furthermore, the



3D/2D hybrid perovskite has a much greater number of boundary nodes where migrating ions along the direction of the external electric field can be blocked and lose their kinetic energy leading to the termination of their migration. In order to scrutinize the structure of the 3D/2D hybrid perovskites in grain scale, we used high-angle annular dark-field scanning transmission electron microscopy (HAADF-STEM) and clearly observed the 2D perovskite layer with  $n = 1$  (Figure 2.23). Highly oriented 2D phase was shown to surround the inner 3D core, as reported similarly before using small amount of 2D perovskite precursors<sup>47</sup>.



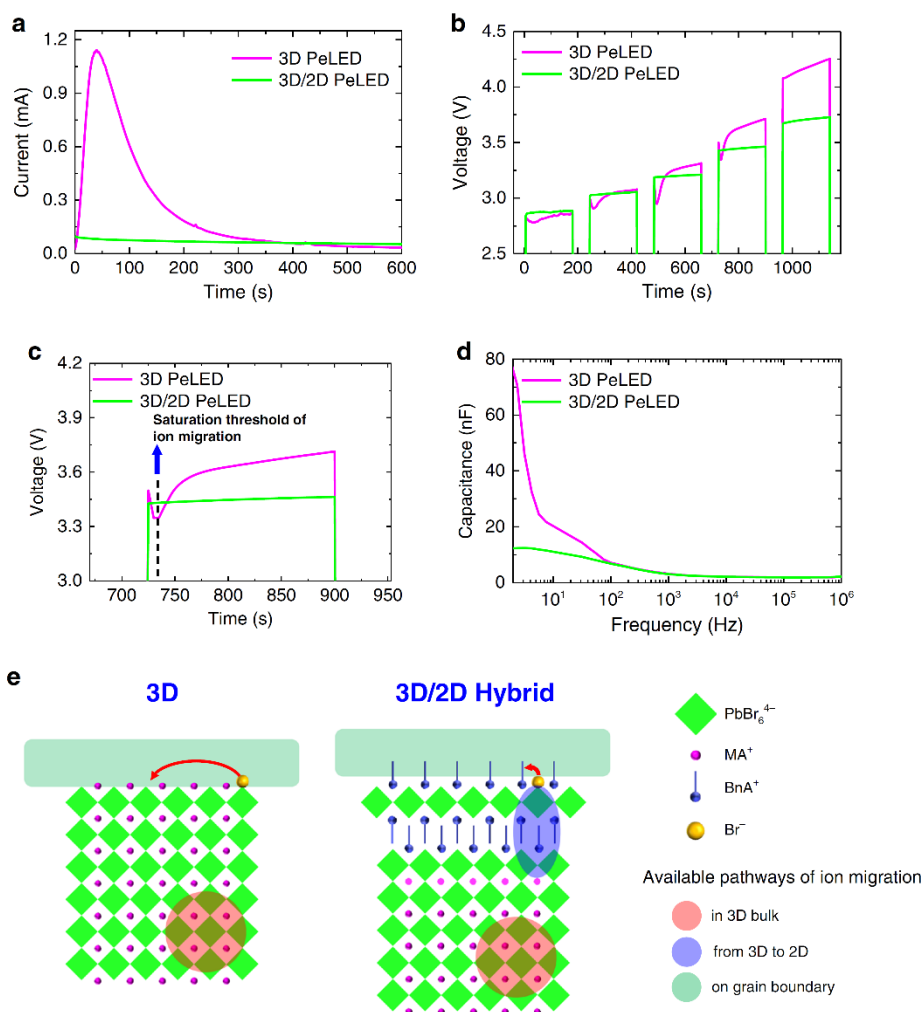


**Figure 2.21** Influence of ion migration in perovskites on PeLEDs. **a** Current behaviour of PeLEDs as a function of time under constant voltage of 3.5 V. **b** Voltage behaviour of PeLEDs under increasing step constant current of 0.16, 0.22, 0.44, 1.11, 2.22  $\text{mA}\cdot\text{cm}^{-2}$  from the left column to the right in a sequence. **c** Magnified version of one step showing the discrepancy in the voltage behaviour between 3D PeLED and 3D/2D hybrid PeLED. **d** Capacitance-frequency curve of PeLEDs. **e** Schematic of possible ion migration pathways in 3D and 3D/2D hybrid perovskites and efficient restriction of ion migration owing to the BnA which has retardation effect of reorientation.



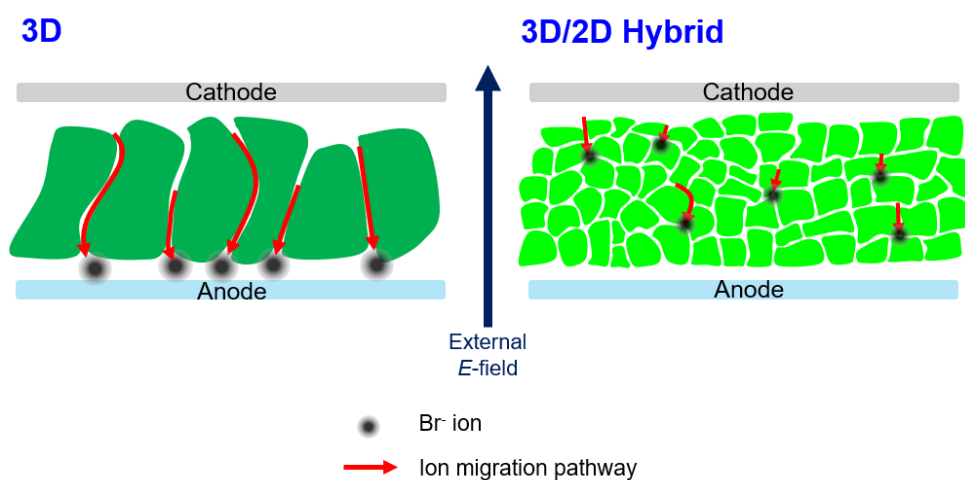


**Figure 2.22** Schematic showing ion migration pathway in 3D (left) and 3D/2D hybrid (right) perovskite.



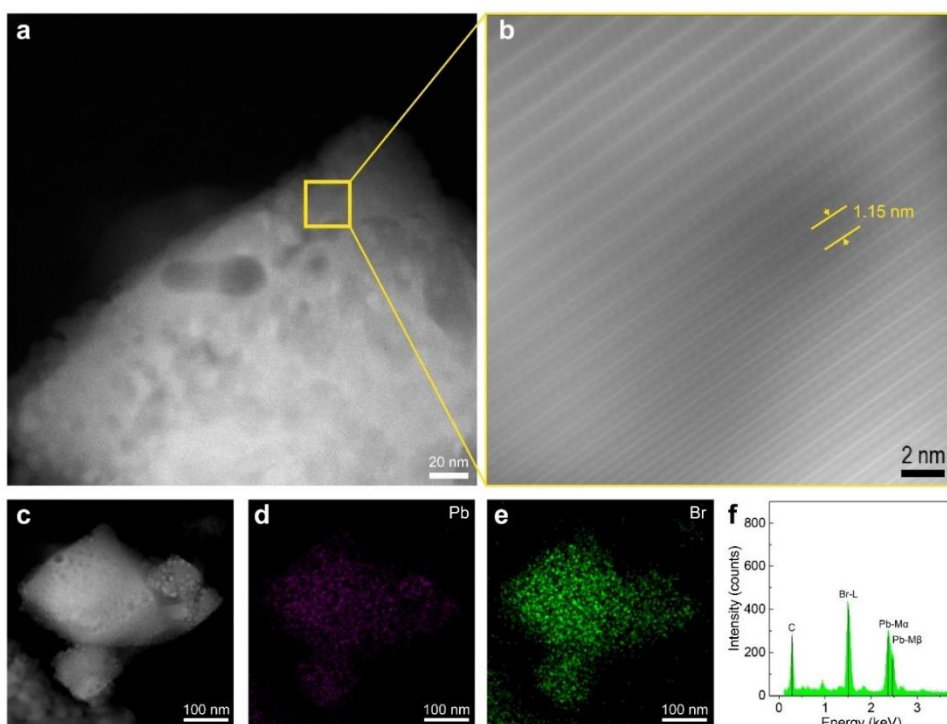


**Figure 2.23** **a**, HAADF scanning TEM image of a 3D/2D hybrid perovskite grain. **b**, High-resolution image of the grain framed with the yellow box in **a** showing the 2D perovskite ( $n = 1$ ) with  $d$ -spacing of 1.15 nm. It is worth noting that the smaller  $d$ -spacing (1.15 nm) than that obtained by grazing-incident X-ray diffraction (GIXD) analysis (1.66 nm) can be attributed to transient lattice contraction due to the highly strong beam intensity. Interestingly, the highly periodic 2D perovskite was only observable at the shell region of the grain. Because the 2D perovskite has lower surface energy than the 3D perovskite due to its fewer surface dangling bonds and surface relaxation, growth of the 2D perovskite most possibly occurs on the 3D perovskite grains and it also makes an interface with grain boundary which has the highest surface energy, thereby lowering the total potential energy of the system. Therefore, the mounted 2D perovskite on the 3D perovskite can effectively passivate the traps and block ion migration. **c**, A lower magnification HAADF scanning TEM image of the 3D/2D hybrid perovskite grain shown in **a**, corresponding EDXS elemental maps of **d**, Pb and **e**, Br, and **f**, integrated EDX spectrum of the acquired dataset. HAADF-STEM images and corresponding EDXS elemental maps indicate that the grain is composed of Pb and Br elements.



*Ab initio* molecular dynamics (MD) simulations predicted that ion migration in perovskites can be greatly assisted by MA<sup>+</sup> reorientation in response to motion of the halide ion<sup>48</sup>. For example, the rotation of MA<sup>+</sup> can lead to the displacement of a halide ion along the direction of the C-N axis of MA<sup>+</sup> based on their attractive Coulomb force. Thus, the incorporation of less orientationally mobile cations with a lower rotational degree of freedom than MA<sup>+</sup> can reduce ion migration in perovskites. In this regard, BnA<sup>+</sup> can have remarkably reduced reorientation rate by themselves based on their  $\pi$ - $\pi$  interaction and steric repulsion as a result of neighbouring benzene rings; this slowing of BnA<sup>+</sup> reorientation in the perovskite lattice can effectively impede ions migration along GBs compared to MA<sup>+</sup><sup>49</sup>.

Combining the simulation results with the transition-state theory of rate processes, we can predict the retardation effect of BnA<sup>+</sup> relative to MA<sup>+</sup> on the ion migration rate. We examined this retardation effect more concretely by considering atomic-bond breaking associated with the organic-cation reorientation. In MAPbX<sub>3</sub>, the two dominant hydrogen bonds should be broken to allow 180° reorientation of an MA<sup>+</sup> adjacent to a migrating defect ion<sup>50</sup>. We defined the energy of the dominant hydrogen bond between a proton in NH<sub>3</sub> and halide ion in the PbX<sub>6</sub> octahedron unit as  $E_{\text{HB}}$ . Previous *ab initio* calculations based on quantum mechanics of atoms in molecule (QTAIM) obtained  $E_{\text{HB}} \approx 200$  meV/MA<sup>+</sup> for MAPbI<sub>3</sub><sup>50,51</sup>. In BnA<sup>+</sup>, the breaking of the  $\pi$ - $\pi$  interaction themselves should be considered, in addition to the rupturing of this hydrogen bonding. According to *ab initio* calculations based on the density-functional tight-binding (DFTB) method, the energy  $E_{\pi\pi}$  of the  $\pi$ - $\pi$  stacking interaction between two neighbouring benzene rings is -4.38 kcal·mol<sup>-1</sup>. For



simplicity, we assume that  $E_{HB}$  of  $BnA^+$  is approximately equal to that of  $MA^+$ . This assumption does not alter our qualitative argument on the retardation effect caused by the substitution of  $BnA^+$  for  $MA^+$ . We define the rate (frequency per unit time) of reorientation of  $BnA^+$  and  $MA^+$  as  $\nu_{BnA}$  and  $\nu_{MA}$ , respectively, and the retardation coefficient ( $R_c$ ) as the ratio of these two frequencies. According to the transition-state theory,

$$\nu_{BnA} = \frac{RT}{N_0 h} e^{-(E_{HB} + 2E_{\pi\pi})/(RT)}, \quad (5)$$

where  $N_0$  is Avogadro's number,  $h$  is Planck's constant, and  $R$  denotes the gas constant ( $= 1.987 \text{ cal}\cdot\text{mol}^{-1}\cdot\text{K}^{-1}$ )<sup>49</sup>; Here, a factor of '2' is introduced in the exponent by considering that two  $\pi$ - $\pi$  stackings must be broken for the reorientation of each  $BnA^+$  in the 3D/2D hybrid structure. Then the retardation coefficient can be written as  $R_c \equiv \frac{\nu_{BnA}}{\nu_{MA}} \approx e^{-2E_{\pi\pi}/(RT)} = 4.23 \times 10^{-7}$  at 300 K. This is only an order-of-magnitude estimate, but it suggests strongly that the substitution of  $BnA^+$  for  $MA^+$  remarkably reduces the reorientation rate and, thereby significantly suppresses ion migration.

### Stability of PeLEDs and ion migration

The 3D/2D hybrid PeLEDs also showed the excellent  $I$ - $V$ - $L$  reliability under the repetition of sweeping voltage from 0 to 5 V and remarkably maintained its current density and luminance in spite of the repeating voltage sweep over 20 times (Figure 2.24a-d). This characteristic is a result of the suppressed ion migration. In contrast, the 3D PeLED showed degradation in current density and luminance in less than 10 such voltage sweeps. The 3D/2D hybrid PeLED also showed much less  $J$ - $V$



hysteresis than the 3D PeLED under continuous forward and backward scan (Figure 2.25). This excellence of the stability demonstrates that the 3D/2D hybrid PeLED has much better operational stability than the 3D PeLED. The measurement was performed under CC condition for each device to elicit luminance of 100  $\text{cd}\cdot\text{m}^{-2}$  (Figure 2.24e). The luminance of the 3D PeLED overshoot to 150.4 % of the initial luminance, then dropped to 40 % of the luminance after time  $T_{40} = 38$  min. As ions migrate towards and accumulate at each end of the perovskite layer, the charge injection from the electrodes tends to be facilitated because of the strong local electric field at the interfaces, and this facilitation results in the initial luminance overshoot. In contrast, the 3D/2D hybrid PeLED had a dramatically increased operating lifetime as  $T_{40} = 810$  min, which is more than 21 times longer than  $T_{40}$  of 3D PeLED. Moreover, the 3D/2D hybrid PeLED showed extremely reduced luminance overshoot as only 7.4 % increase from the initial luminance, because the ion migration was effectively suppressed (Figure 2.24f). We also investigated the operational stability of the PeLED using the ANI-added  $\text{MAPbBr}_3$ , which showed strong luminance overshoot as 146.7 % compared to the initial luminance, implying that the addition of ANI cannot effectively suppress the ion migration (Figure 2.26). We summarized the luminance overshoot of PeLEDs from reported studies and compared their overshoot ratios (**Table 2.2 and Figure 2.27**).



Ref.	Device structure	Emission layer (colour)	Operational lifetime	Overshoot ratio ( $L_{max}/L_0$ ) [%]
6	ITO/PEDOT:PSS/Perovskite/PMMA <sup>a</sup> /B3PYMPM <sup>b</sup> /LiF/Al	CsPbBr <sub>3</sub> /MABr (Green)	$T_{50} \approx 10.42$ m	87.6 at 166.67 mA cm <sup>-2</sup>
7	ITO/NiO <sub>x</sub> /Perovskite/TPBi/LiF/Al	FAPbBr <sub>3</sub> /BnABr (Green)	$T_{50} \approx 1.67$ h	189.8 $L_0 \approx 100$ cd m <sup>-2</sup>
8	ITO/LiF/Perovskite/LiF/Bphen <sup>c</sup> /LiF/Al	CsPbBr <sub>3</sub> (Green)	$T_{50} \approx 96$ h	97.9
9	SOCP <sup>d</sup> /Perovskite/TPBi/LiF/Al	FA <sub>2</sub> Cs <sub>1-x</sub> PbBr <sub>3</sub> (Green)	$T_{50} \approx 0.67$ h	182.2 $L_0 \approx 100$ cd m <sup>-2</sup>
10	SOCP/Perovskite/TPBi/LiF/Al	MAPbBr <sub>3</sub> :TPBI (Green)	$T_{50} \approx 2.5$ h	51.2 $L_0 \approx 100$ cd m <sup>-2</sup>
<b>This work</b>	<b>FTO/Buf-HIL/Perovskite/TPBi/LiF/Al</b>	<b>MAPbBr<sub>3</sub> : BnA<sub>2</sub>MA<sub>n-1</sub>Pb<sub>n</sub>Br<sub>3n+1</sub> (n=1 or 2) (Green)</b>	<b><math>T_{50} \approx 14</math> h</b>	<b>7.4 <math>L_0 \approx 100</math> cd m<sup>-2</sup></b>

**Table 2.2** A summary of published luminance overshoot of PeLEDs with visible emission. ( $T_{50}$ : half lifetime,  $L_0$ : initial luminance,

<sup>a</sup>PMMA: poly(methyl methacrylate),

<sup>b</sup>B3PYMPM: 4,6-bis(3,5-di(pyridin-3-yl)phenyl)-2-methylpyrimidine,

<sup>c</sup>Bphen: Bathophenanthroline, <sup>d</sup>SOCP: Self-organized conducting polymer)

The applied voltage in the devices also showed a large difference as a function of time (Figure 2.24g). The steeper voltage increase in the 3D PeLED indicates the inferior stability of the device compared to the 3D/2D hybrid PeLED. Also, accumulated ions at the interface can cause chemical corrosion of electrodes and thereby accelerate degradation of the device. The 3D/2D hybrid PeLED does not suffer from those problems because of the effectively suppressed ion migration resulting in the much longer operating lifetime than the 3D perovskite PeLED.



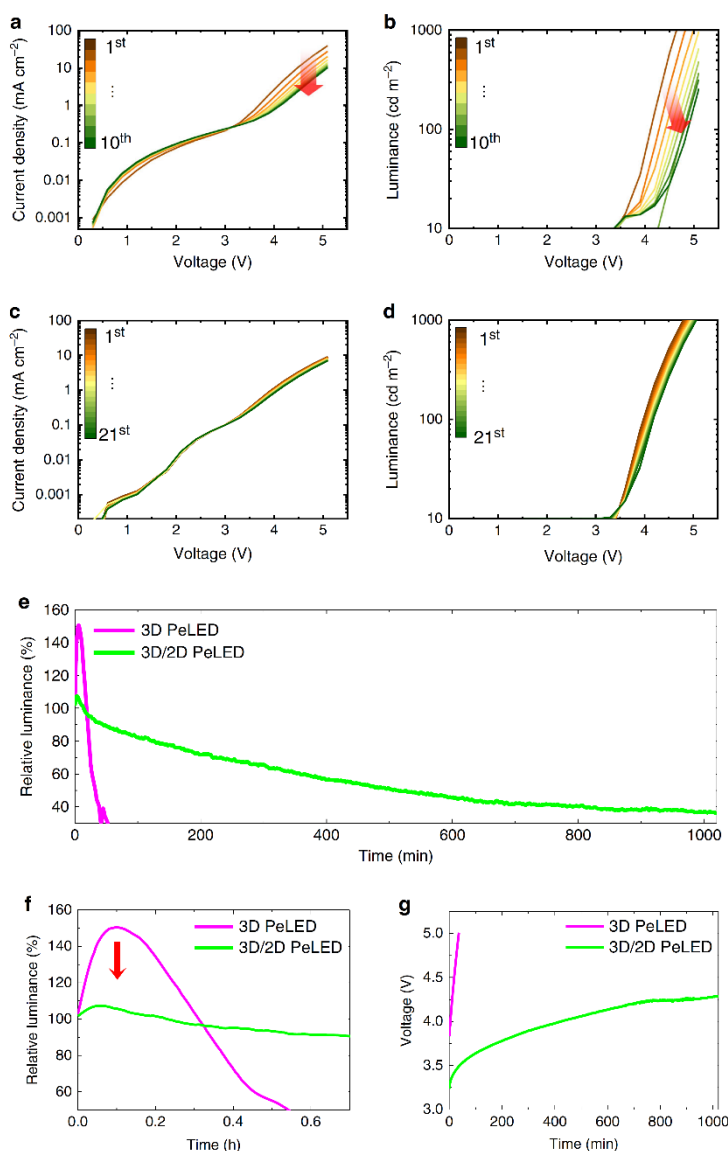


**Figure 2.24** Reliability and long-term stability of PeLEDs. **a**,  $J$ - $V$  and **b**,  $L$ - $V$  curves of 3D PeLEDs with a repetition of voltage sweep and **c-d**, those of 3D/2D hybrid PeLED. **e**, Relative luminance of 3D/2D hybrid PeLED (green) and of 3D PeLED (red) over time. **f**, Magnified version of relative luminance of PeLEDs showing an extremely reduced overshoot of luminance. **g**, Voltage curves of 3D/2D hybrid PeLED (green) and 3D PeLED (red) over time under constant current to make PeLEDs have an emission of  $100 \text{ cd} \cdot \text{m}^{-2}$ .



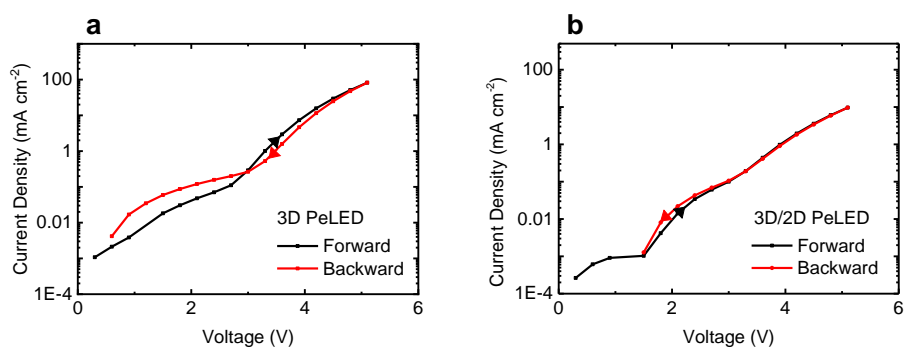


**Figure 2.25** Current-voltage hysteresis on forward-backward sweep of **a**, 3D PeLED and **b**, 3D/2D hybrid PeLED.



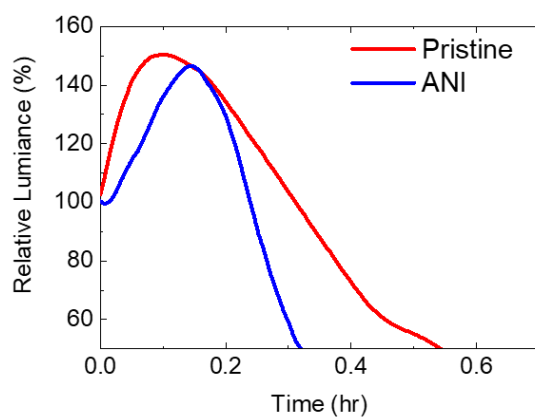


**Figure 2.26** Relative luminance of PeLEDs using pristine MAPbBr<sub>3</sub> emitter and 2.4 mol % ANI-added MAPbBr<sub>3</sub> emitter over time.



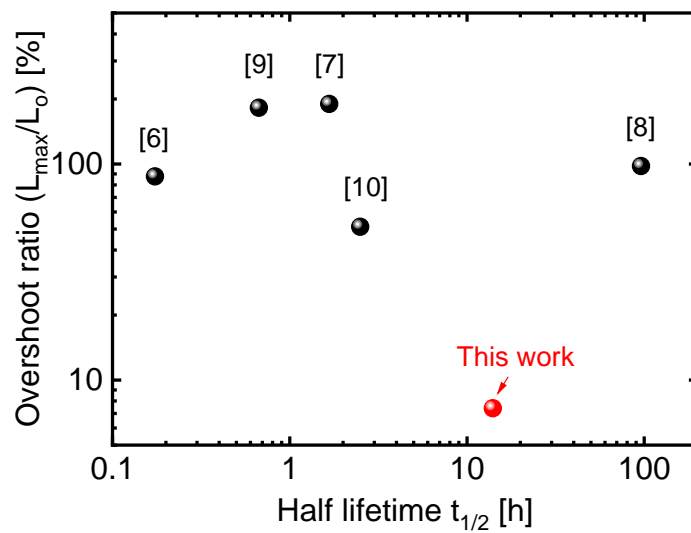


**Figure 2.27** A summary of reported luminance overshoot ratio versus half lifetime of PeLEDs with green emission on table 2.2 ( $L_{\max}$ : maximum luminance,  $L_0$ : initial luminance).



## 2.4. Conclusion

Perovskite light-emitter of proton-transfer-induced 3D/2D hybrid structure composed of dominant 3D MAPbBr<sub>3</sub> and a small amount of 2D BnA<sub>2</sub>PbBr<sub>4</sub> has been developed by using a neutral amine reagent BnA instead of ammonium halide salt. A proton-transfer reaction between MA<sup>+</sup> and BnA occurs in the precursor state, and facilitates participation by BnA<sup>+</sup> in 2D perovskite crystallization. A 2D phase forms without destroying 3D perovskite phase in the film. The incorporation of 2D perovskite into 3D perovskite restricts the formation of ionic defects because BnA<sup>+</sup> has a lower rotational degree of freedom than MA<sup>+</sup>. Therefore, 3D/2D hybrid perovskite leads to efficient radiative recombination by deactivating even deep-level trap states. Also, the 3D/2D hybrid structure can suppress ion migration owing to the retardation effect in reorientation of BnA<sup>+</sup> in the lattice based on  $\pi$ - $\pi$  interaction of their aromatic rings by considering possible pathways of ion migration. PeLEDs with the 3D/2D hybrid perovskite emitter show an extremely reduced initial luminance overshoot ratio as 7.4 %, 21 times longer operational stability without noticeable overshoot of luminance, and improved luminous efficiency. The material insights on ‘proton-induced 3D/2D hybrid perovskites’ we propose can help pave the way for the future practical applications of perovskite electronics with long operating lifetime.



# **Chapter 3. *In situ* Formed Core/Shell Perovskites for Simultaneously Ultra-Bright, Efficient, and Stable Perovskite LEDs**

## **3.1. Introduction**

Metal halide perovskites (MHPs) are being studied as promising candidates for light emitters due to their narrow emission spectra (full-width at half maximum (FWHM)  $\approx 20$  nm), easy color tuning, excellent charge transport properties, and low-cost solution processability<sup>1–3,21</sup>. Because of these advantages, research has mainly focused on achieving highly-efficient operation of perovskite light-emitting diodes (PeLEDs). By introducing a perovskite nanocrystal structure synthesized with organic ligands or cation alloying (e.g. FAGAPbBr<sub>3</sub>), high current efficiency of 108 cd A<sup>-1</sup> and external quantum efficiency (EQE) of 23.4 % were achieved by realizing strong carrier confinement and bulk/surface defect suppression<sup>2,4–11</sup>. However, in these perovskite nanocrystal emitters, the insulating characteristics of organic ligands can impede charge injection and transport, and thereby limit the brightness at the given voltage and the operational lifetime despite their high luminous efficiency<sup>11–14</sup>. In contrast, 3D polycrystalline perovskite (hereafter, 3D perovskite)



film without such organic ligands has good charge transport characteristics and simple fabrication processes, but low luminous efficiency because of the poor charge confinement effect in the big grains of >100 nm and non-radiative recombination defects at the grain boundary<sup>16–19</sup>. Although the improvements in both perovskite nanocrystals and 3D perovskites have enabled drastic advances in the EQE of PeLEDs, the state-of-the-art efficient PeLEDs mostly suffer from low brightness ( $\sim 10,000 \text{ cd m}^{-2}$ )<sup>5,8,14</sup> and short device half-lifetime ( $T_{50}$ ) (< 100 h at initial brightness ( $L_0$ ) =  $100 \text{ cd m}^{-2}$ )<sup>5</sup>. Therefore, developing a perovskite material system that allow high brightness, high efficiency and long device lifetime simultaneously is of great importance at the current stage of research on PeLEDs.

Here, we developed a simple method to produce *in situ* core/shell nanocrystals by reacting 3D perovskite films with benzylphosphonic acid (BPA), which can split large crystals into nanoparticles (NPs) and surround them to form a core/shell structure. Significantly reduced particle size of *in situ* core/shell nanocrystals ( $10 \pm 2 \text{ nm}$ ) compared with that of the 3D perovskite ( $200 \pm 97 \text{ nm}$ ) showed significantly improved carrier confinement, and the phosphonate group of BPA effectively passivated the defect sites by binding covalently to undercoordinated  $\text{Pb}^{2+}$ . In the *in situ* core/shell perovskite NPs, the trap density was greatly decreased and the radiative recombination efficiency was significantly increased compared to the 3D perovskites. PeLEDs based on *in situ* core/shell structure showed maximum current efficiency of  $151 \text{ cd A}^{-1}$  (maximum EQE of 28.9 %), maximum brightness of  $\sim 470,000 \text{ cd m}^{-2}$ , very little efficiency roll-off ( $\sim 5\%$  even at  $400,000 \text{ cd m}^{-2}$ ) and half-lifetime of 520 h at initial brightness of  $1,000 \text{ cd m}^{-2}$  (estimated half-lifetime >30,000 h at  $100 \text{ cd m}^{-2}$ ) with green emission at EL peak



of 540 nm, and therefore shows excellent efficiency, luminance, and lifetime simultaneously.



## 3.2. Experimental

**Materials.** Formamidinium bromide (FABr, > 99.99 %), Methylammonium bromide (MABr, > 99.99 %), and Guanidinium bromide (GABr, > 99.99 %) were purchased from Dyesol. Cesium bromide (CsBr), BPA, tetrafluoroethylene-perfluoro3,6-dioxa-4-methyl-7-octene-sulfonic acid copolymer (PFI), Chlorobenzene (CB), Tetrahydrofuran (THF), and Molybdenum oxide ( $\text{MoO}_3$ ) were purchased from Sigma-Aldrich. Lead bromide ( $\text{PbBr}_2$ ) was purchased from TCI Co., Ltd. 2,2',2''-(1,3,5-Benzinetriyl)-tris(1-phenyl-1-H-benzimidazole) (TPBi) was purchased from OSM. 9,10-di(naphthalene-2-yl)anthracen-2-yl-(4,1-phenylene)(1-phenyl-1H-benzo[d]imidazole) (ZADN) was purchased from Shinwon Chemtrade Co., Ltd. Lithium fluoride (LiF) was supplied from Foosung Co., Ltd. Unless otherwise stated, all materials are used without purification.

**Preparation of MHP solution.** The mixed-cation precursor,  $((\text{FA}_{0.7}\text{MA}_{0.1}\text{GA}_{0.2})_{0.87}\text{Cs}_{0.13}\text{PbBr}_3)$  was prepared by dissolving stoichiometric ratio of each of FABr, MABr, GABr, CsBr and  $\text{PbBr}_2$  (molar ratio  $(\text{FABr} + \text{MABr} + \text{GABr} + \text{CsBr}) : \text{PbBr}_2 = 1.15 : 1$ ) in DMSO at a concentration of  $1.2 \text{ M}^{8,52}$ . In case of precursor solution for the *in situ* particle perovskite, 10 mol. % of BPA relative to  $\text{PbBr}_2$  were added. The solution was stirred overnight in  $\text{N}_2$ -filled glove box before use.

**Fabrication of PeLEDs.** Pre-patterned FTO(200 nm) glasses (25 mm X 25 mm) were sonicated in acetone and 2-propanol for 15 min each sequentially, then boiled



in 2-propanol for 30 min. The surface of FTO substrates undergo ultraviolet-ozone (UVO) treatment to achieve hydrophilic surface. We used a previously-described method to synthesize a HIL (BufHIL) that has a gradient work function (WF), by inducing self-organization of PEDOT:PSS (CLEVIOS P VP AI4083) and tetrafluoroethylene-perfluoro3,6-dioxo-4-methyl-7-octene-sulfonic acid copolymer (PFI); the solution was spin-coated to form 75-nm thickness, then annealed at 150 °C for 30 min<sup>21</sup>. After baking, the substrates were transferred into a N<sub>2</sub>-filled glove box for deposition of MHP layer. MHP films with thickness of 270 nm were deposited by spin-coating the precursor solution at 6000 rpm with additive-assisted nanocrystal pinning (NCP) process:<sup>2</sup> during the second spin step, TPBi-dissolved CB solution was dropped onto the spinning perovskite film. For synthesis of *in situ* core/shell perovskite film, BPA dissolved in THF solution was loaded on top of the perovskite, followed by reaction time of 30s and direct spin-drying afterward. Samples were then moved to the vacuum chamber (<10<sup>-7</sup> Torr) to sequentially deposit ZADN (45 nm), LiF (1.2 nm), and Al (100 nm). The active area of 4.9 mm<sup>2</sup> was defined by shadow masking during deposition of cathode. Finally, the fabricated PeLEDs were encapsulated under N<sub>2</sub> atmosphere by using a glass lid and UV-curable epoxy resin.

**Perovskite film characterizations.** Images of the surfaces were obtained using a field-emission scanning electron microscope (SEM) (SUPRA 55VP). XPS and UPS spectra were measured by using a photoelectron spectrometer (AXIS-Ultra DLD, Kratos Inc.). A monochromatic Al-K $\alpha$  line (1486.6 eV) was used for XPS, and He I radiation (21.2 eV) was used for UPS. Steady-state photoluminescence



(PL) spectra and ultraviolet/visible (UV-Vis) absorption spectra were measured by using a JASCO FP8500 spectrofluorometer and Lambda-465 UV-Vis spectrophotometer. For transient PL decay measurement, a system composed of a streak camera (c10627, Hamamatsu Corp.) and a nitrogen pulse laser (337 nm, 20 Hz, Usho Inc.) was used. PLQY was measured with a PMT and monochromator (Acton Research Corporation) using a 325 nm He:Cd CW laser (Kimmon Koha) at the excitation power of  $62.5 \text{ mW cm}^{-2}$ . Direct and indirect emission from the perovskite film was measured to determine the accurate PLQY values. For the temperature-dependent PL measurement, the sample was mounted in a cryostat under vacuum and the emission spectrum was analyzed. For single-carrier device analysis,  $\text{MoO}_3$  (30nm) and Au (50nm) were thermally deposited sequentially onto FTO / BufHIL / perovskite and encapsulated in  $\text{N}_2$  atmosphere to obtain the current-voltage curve using a Keithley 236 source measurement unit.

### **Transmission electron microscopy characterizations.**

Perovskite thin films were deposited on a 5-nm-thick silicon nitride membrane using the same spin-coating conditions as for the actual device. The membrane, with a size of  $100 \mu\text{m} \times 1,500 \mu\text{m}$ , is supported on a 100- $\mu\text{m}$ -thick silicon frame. The silicon nitride membrane grid was loaded on a sample holder for TEM characterization without further processing of TEM sample preparation. Double Cs-corrected (S)TEM systems (Themis Z, Thermo Fischer Scientific) equipped with EELS (Quantum ER965, Gatan) and EDX (Super-X EDS system) were used for atomic-scale structure imaging and chemical analysis of the samples at an accelerating voltage of 200 kV. Due to the electron beam damage of core/shell perovskite



nanocrystals by high-energy electron illumination in TEM, we acquired high-resolution TEM images, high-resolution STEM-HAADF images, and EELS and EDS data at the low dose-rates. Core-loss EELS using a 2 Å nominal probe size and 1.8-2.0 eV energy resolution were obtained with exposures of 12 sec (integrated by 60 scans with each taking for 0.2 sec). EELS entrance aperture of 5 mm, and an energy dispersion of 0.5 eV/ch and 1.0 eV/ch were used for high-loss EELS (>1500 eV).

#### **Characterization on efficiency of PeLEDs.**

Electroluminescence efficiencies of the fabricated PeLEDs were measured using a Keithley 236 source measurement unit and a Minolta CS-2000 spectroradiometer. External quantum efficiency of PeLEDs was calculated by measuring full angular electroluminescence distribution<sup>53</sup>.

**Lifetime analysis of PeLEDs.** Operational lifetime of PeLEDs was measured under constant current condition by simultaneously tracking brightness and applied voltage using a M760 Lifetime Analyzer (Mcscience Inc.) with control computer.

**Optical Simulation.** Outcoupling efficiency, perovskite reabsorption  $A_{\text{act}}$ , and parasitic absorption  $A_{\text{para}}$  were obtained from the calculated Poynting vectors at each interface of glass ( $n = 1.5$ , incoherent)/ FTO ( $n = 1.9$ , 200 nm)/ BufHIL ( $n = 1.5$ , 75 nm)/ perovskite / ZADN ( $n = 2$ , 45 nm)/ LiF ( $n = 1.4$ , 1.2 nm)/ Al ( $n$  from literature<sup>54</sup>), by using a recently-proposed method<sup>55,56</sup> ( $n$ : refractive index). The imaginary part of the refractive index spectrum of perovskite was obtained from



the measured absorbance, while the real part was assumed to be constant ( $n_{\text{perov}} = 2.3$ ). The internal radiation spectrum was obtained by the reverse calculation from the measured external radiation spectrum. The maximum EQE values with photon recycling effect were obtained at each perovskite thickness, by integrating the results for dipoles with various wavelengths, orientations (vertical and horizontal), polarizations ( $s$  and  $p$ ), and positions (20 positions uniformly distributed over the perovskite layer). The relationship between external and internal PLQE was calculated in the same way, for the structure of glass/perovskite.



### 3.3. Result and Discussion

#### *In situ* nanostructure formation by BPA treatment

We first show how post-treatment using BPA forms the *in situ* nanostructure of the perovskite crystal. 3D perovskite film of  $(\text{FA}_{0.7}\text{MA}_{0.1}\text{GA}_{0.2})_{0.87}\text{Cs}_{0.13}\text{PbBr}_3$  was fabricated (left of **Figure 3.1a**) using the additive-based nanocrystal pinning (A-NCP) method<sup>2</sup>. In this case, ionic defects with low formation energy exist on the crystal surface and inside the crystal, acting as a cause of ion migration and carrier trapping, thereby significantly reducing the luminescence efficiency and operational stability<sup>19</sup>. First, we added BPA as an additive into the precursor solution, implementing an *in situ* particle structure in which BPA cover the surface of crystals by attaching as a ligand to the undercoordinated Pb on the surface of 3D perovskites (center of **Figure 3.1a**). The surface of the 3D perovskite film initially had an amorphous and irregular shape due to a defective surface; after addition of up to 10 mol. % of BPA into the precursor, the fabricated film developed a very clear cubic structure as the BPA molecules assembled on the surface (**Figure 3.2, 3.3**).

The perovskite thin film was further exposed to a BPA solution in tetrahydrofuran (THF), forming *in situ* core/shell perovskite NPs (right of **Figure 1a**). Unlike other long alkyl ligands (e.g. oleic acid, decylamine, and octylphosphonate), small BPA molecules with strong acidity can penetrate and intercalate into large perovskite crystals<sup>57</sup>. After sufficient time is provided for the BPA to intercalate into the crystal, BPA binds to the surface sites within the crystal and splits the large crystal domain into a nanosized *in situ* core/shell structure that is surrounded by BPA.



The progressive particle refinement of large 3D perovskite grain to *in situ* core/shell perovskite NPs was observed by high-resolution transmission electron microscopy (TEM). With increasing reaction time in BPA-THF solution, initially rectangular 3D crystals with size of 200 nm showed gradual change in grain shape and decrease of grain size, and finally became spherical *in situ* core/shell structured nanograins with a size of 10 nm. (**Figure 3.1b-i**) The *in situ* core/shell synthesis process was further confirmed using atomic-scale scanning transmission electron microscopy (STEM) and scanning electron microscopy (SEM). At the beginning of the reaction, BPA molecules bind to defective surfaces of large crystals that appear as dark contrast regions or vague boundaries on STEM images, cracking the crystal out and thus reducing the grain size (**Figure 3.4a-c**). The grain splitting reveals new defective surfaces, and the cycle of BPA binding and breakage repeats and the grain size gradually decreased with increased coverage of a BPA shell on the surface (**Figure 3.4d-g**). Finally, when BPA molecules fully surround the 3D core that lacks a defective surface to which BPA can bind, the *in situ* core/shell structure is achieved (**Figure 1e,i**). Perfect 3D lattice structure in the core part and clear core/shell interface between perovskite and BPA molecule was identified by STEM image and electron energy loss spectra (EELS) (**Figure 3.1j-l, Figure 3.5**). When the *in situ* core/shell synthesis is finished, these *in situ* core/shell grains are located adjacent to each other, after being aggregated by the excess BPA molecules around them to form macroparticles, as observed in SEM and TEM images and EDS maps (**Figure 3.6, 3.7**). The grain size distribution of these perovskite grains significantly decreased from the 3D perovskite ( $205 \pm 97$  nm) to the *in situ* particle structure ( $123 \pm 34$  nm) and further to the *in situ* core/shell structure ( $10 \pm 2$  nm) (**Figure 3.8**).



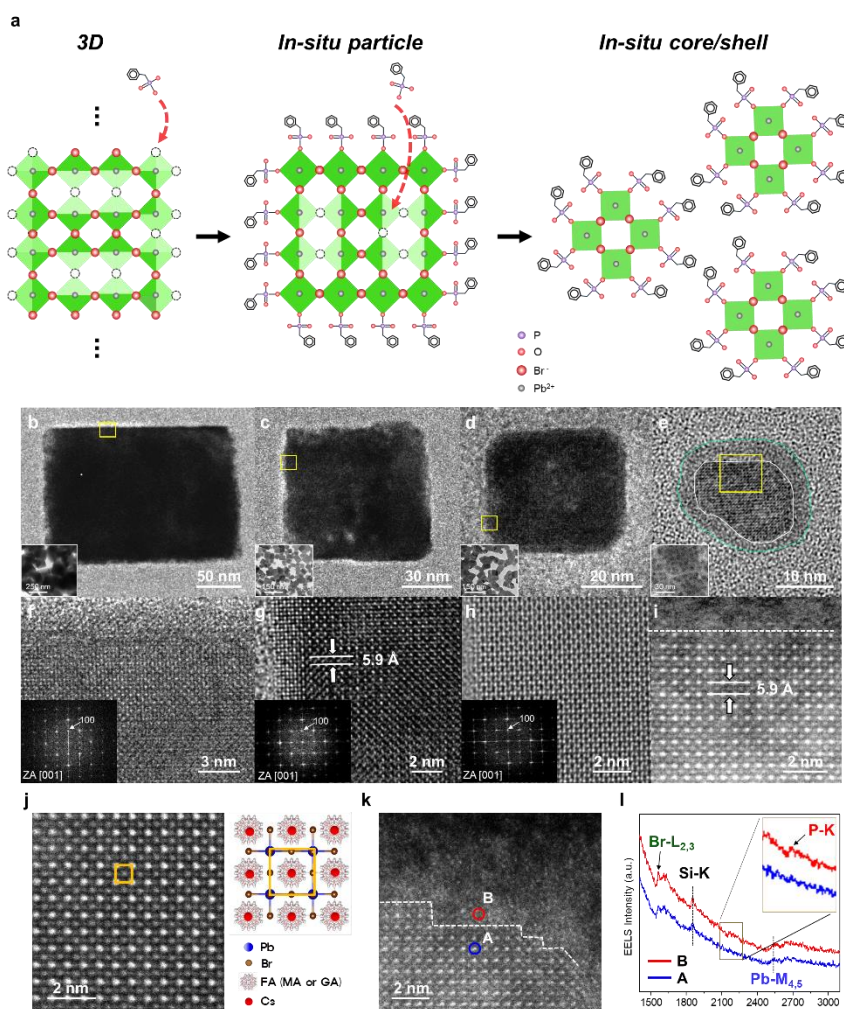


**Figure 3.1** **a**, Schematic illustration of the transformation process of 3D (left) into *in situ* particle (middle) and *in situ* core/shell (right) structure by BPA treatment. TEM image of perovskite nanograins during *in situ* core/shell synthesis process with reaction time of **b**, 1s, **c**, 10s, **d**, 20s, **e**, 30s. (insets: low-magnification TEM images). **f-h**, High-resolution TEM images of the boxed regions in **b-d**. (insets: FFT-diffractograms showing the cubic lattice structure) **i**, High-resolution HAADF-STEM image of the single *in situ* core/shell NP taken from the boxed region in **e**, showing a flat interface between the perovskite core and the BPA shell. **j**, Atomically resolved HAADF-STEM image of the core region taken from the *in situ* core/shell perovskite NP with atomic structure model, showing the perfect 3D perovskite crystal structure. **k**, High-resolution STEM image focusing on surface region of *in situ* core/shell. **l**, the EEL spectra acquired from the positions A and B highlighted in **k**. The Si peak is a background signal from the silicon nitride TEM window grid.



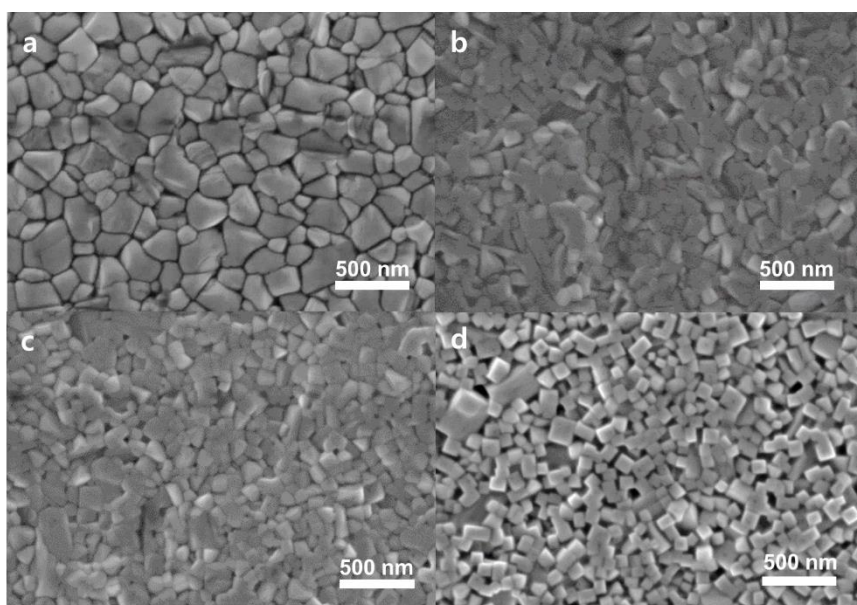


**Figure 3.2** SEM image of perovskite thin films made of 1.2M precursor solution with **a**, 0 % (3D), **b**, 2.5 %, **c**, 5 %, **d**, 10 % (*in situ* particle) molar ratio of BPA molecule relative to  $\text{PbBr}_2$ .



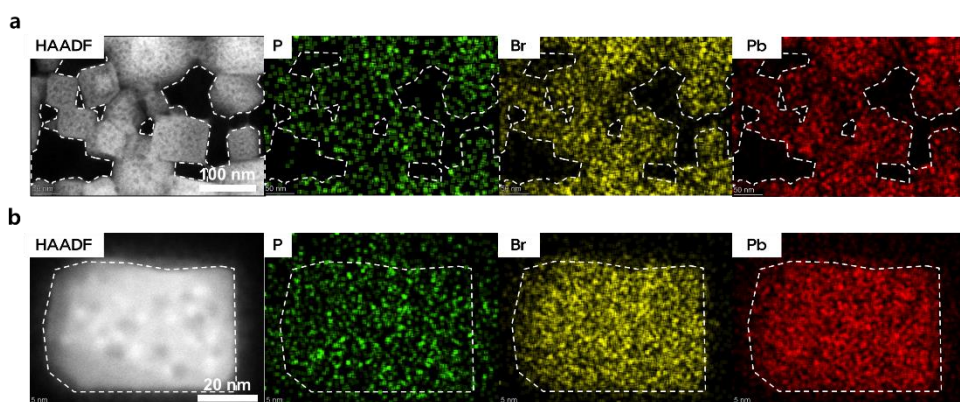


**Figure 3.3** **a**, HAADF-STEM image and EDS elemental maps of P (green), Br (yellow), and Pb (red), respectively. **b**, HAADF-STEM image and EDS elemental maps of a single perovskite grain showing the uniform dispersion of P (green), Br (yellow), and Pb (red) on the grain.



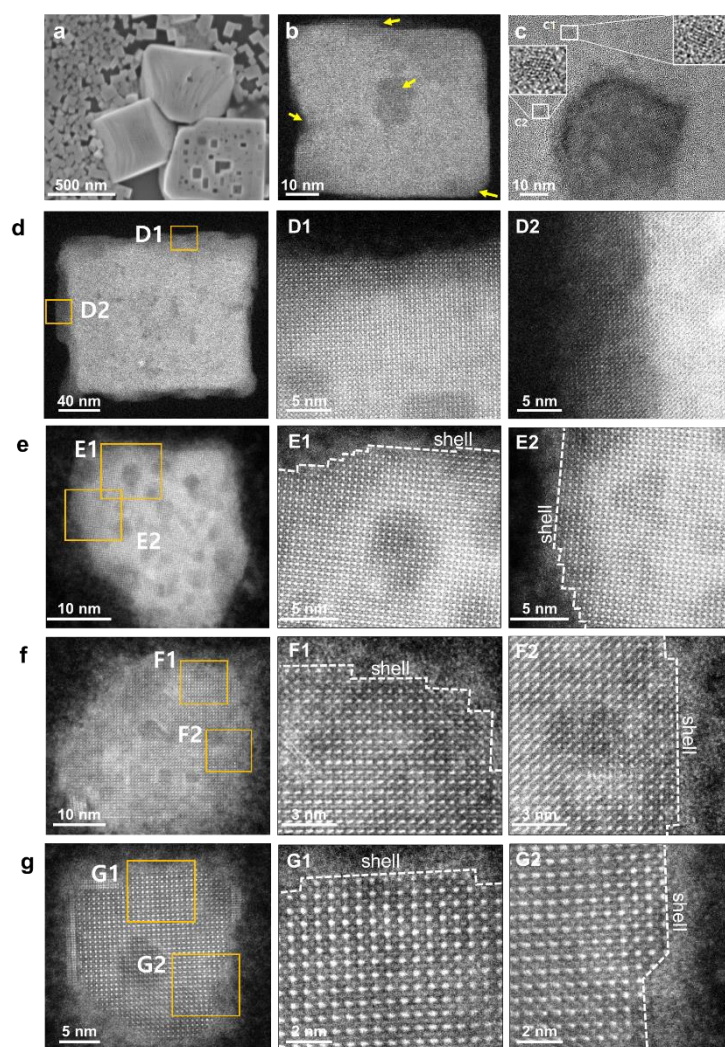


**Figure 3.4** **a**, SEM image of a perovskite thin film (after 1s of reaction time with BPA-THF solution) showing small grains cracked out from large 3D grain. **b**, STEM image of 50-nm-size perovskite crystal during *in situ* core/shell synthesis process. Yellow arrows indicate the defective perovskite surfaces that can be bound with BPA. **c**, HR-TEM image of another perovskite crystal showing ultra-small nanocrystals segregated during *in situ* core/shell synthesis process. Insets: Magnified HR-TEM images of ultra-small nanocrystals taken from the white-boxed regions labelled C1 and C2. **d-e**, High-resolution HAADF-STEM images of single perovskite nanograins with decreasing grain size. Magnified HAADF-STEM images of the grain surfaces (D1, D2, E1, E2, F1, F2, G1, G2) demonstrate that the BPA shell coverages on the grain surfaces gradually increase and the defective surface regions decrease as the grain size decreases.



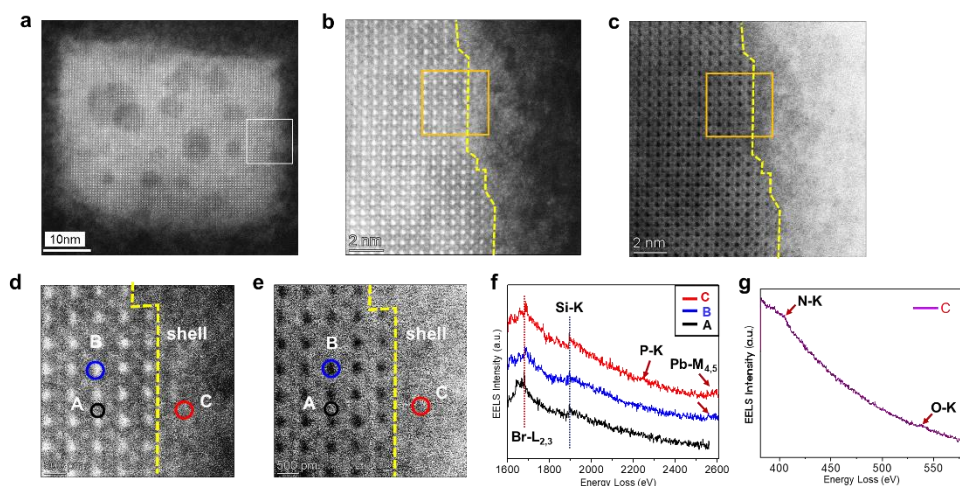


**Figure 3.5** **a**, High-resolution HAADF-STEM image of single perovskite grain formed during *in situ* core/shell synthesis process. **b**, **c**, Atomic-scale HAADF-STEM (**b**) and ABF-STEM (**c**) images of the boxed area denoted in **a**. **d**, **e**, Magnified HAADF-STEM (**d**) and ABF-STEM (**e**) images of the boxed area shown in **b** and **c** to indicate the positions of EELS acquisition. **f**, EEL spectra acquired at the atomic positions labelled A, B, and C in **d**, **e**. **g**, EEL spectrum in the energy-loss range of the N-K and O-K edges acquired at the position labelled C. The O-K peak indicates the presence of BPA shells, but N-K peak is simply a background signal from the silicon nitride TEM window grid.



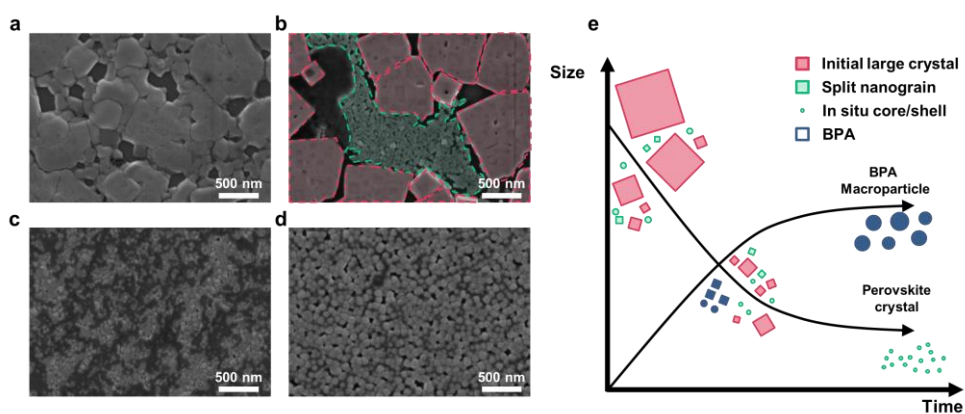


**Figure 3.6** **a**, 3D perovskite without reaction, **b**, 1 s, **c**, 15 s, **d**, 30 s of exposure time to BPA-THF solution before spin-drying. Colored regions indicate *in situ* particle perovskites (red) and *in situ* core/shell perovskites (green). **e**, Schematic illustration of the growth process of BPA macroparticle domain and perovskite crystal forming *in situ* core/shell structure.



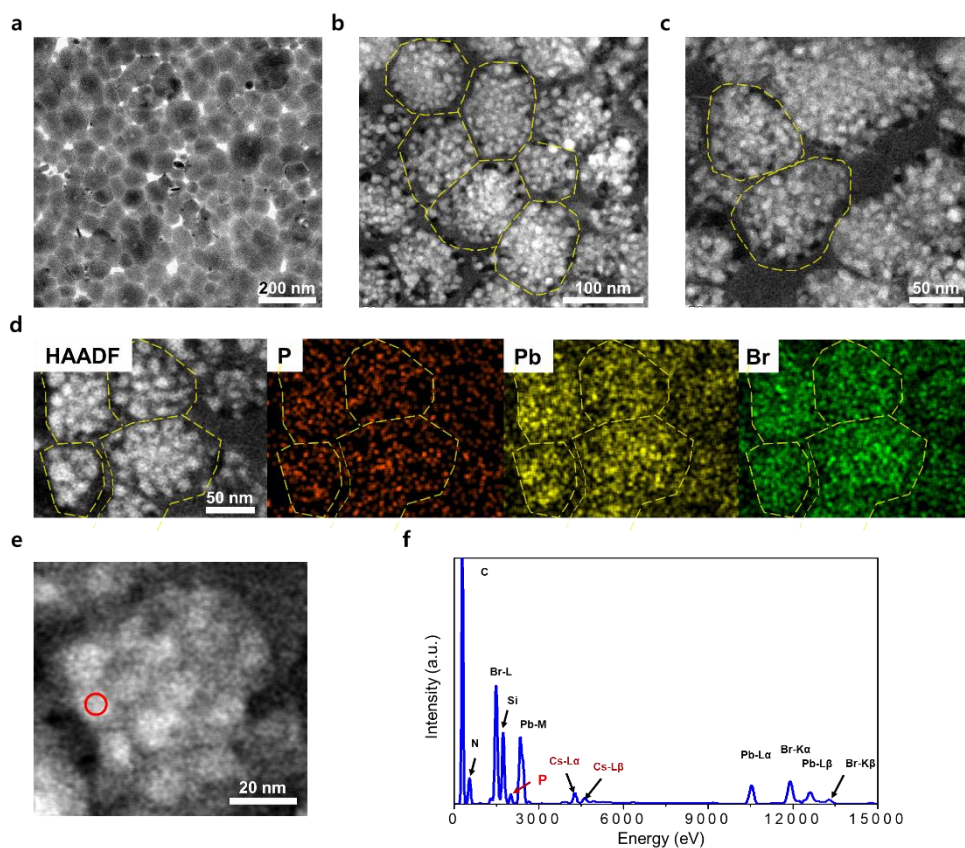


**Figure 3.7** **a**, TEM image and **b**, **c**, magnified HAADF-STEM images of *in situ* core/shell thin films. **d**, HAADF-STEM image of *in situ* core/shell grains and EDS elemental maps of P (red), Pb (yellow), and Br (green), respectively. The EDS maps clearly show the uniform dispersion of P (red) over macrograins. **e**, HAADF-STEM image of single macrograins consists of *in situ* core/shell NPs. **f**, EDS spectrum acquired at the location of the red circled region in **e**.



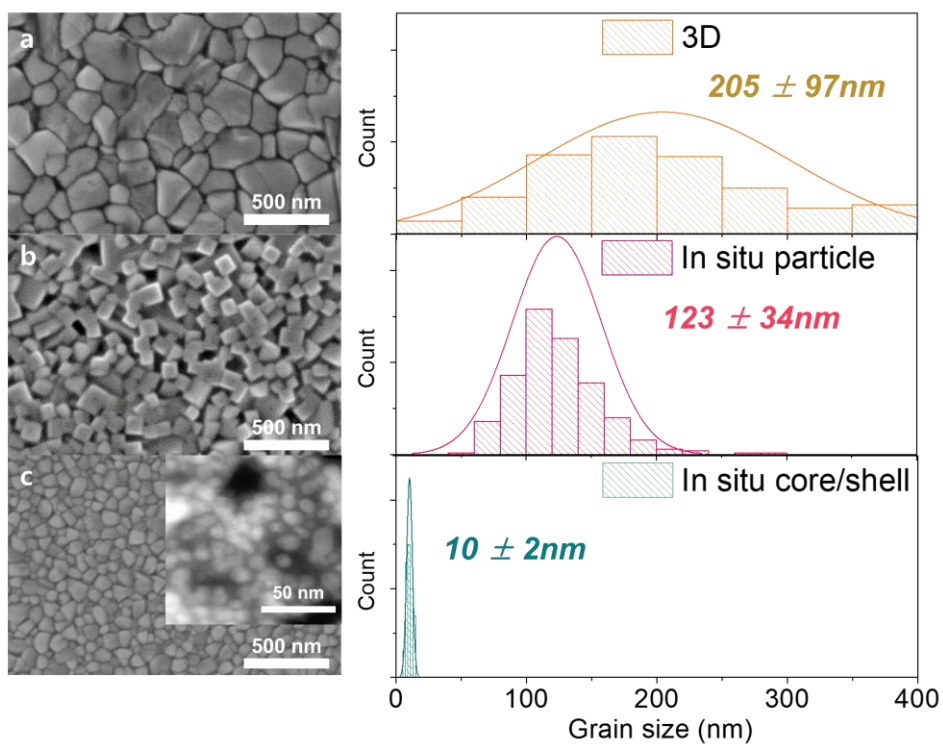


**Figure 3.8** Top SEM image and corresponding grain size analysis of **a**, 3D, **b**, *in situ* particle, and **c**, *in situ* core/shell (inset: magnified view of STEM image in macroparticle showing each *in situ* core/shell grain) perovskite thin films with concentration of 1.2M.



## Surface passivation of BPA shell

To elucidate the mode of binding between BPA and the perovskite structure, we performed X-ray photoelectron spectroscopy (XPS) and ultraviolet photoelectron spectroscopy (UPS) analysis. The existence of BPA in perovskite films can be confirmed by emergence of new peak at P 2p and O 1s spectra only in *in situ* particle and *in situ* core/shell perovskites (**Figure 3.9a-b**). The O 1s spectrum of the BPA prior to any reaction shows the main oxygen peak from the P-OH group at 533.0 eV and the P=O group at 531.5 eV in a ratio of 2:1, which is consistent with previously-reported O 1s spectra of phosphonic acid derivatives (**Figure 3.10a**)<sup>58,59</sup>. In contrast, in the O 1s peak of *in situ* particles and *in situ* core/shell perovskite, a new peak around 531.0 eV appeared (**Figure 3.10b-c**). This change can be ascribed to the formation of covalent bonds during adsorption of phosphonate onto a metallic surface<sup>58,60</sup>. i.e., BPA bonds to the surface of perovskite by forming a new Pb-O-P covalent bond and replaces the bromide vacancy site. The coordination of BPA molecule with PbBr<sub>2</sub> was double-checked by solution-state <sup>1</sup>H NMR spectra. When BPA molecule co-exist with PbBr<sub>2</sub> precursor, coordinative bonding between P(OH)<sub>2</sub> and PbBr<sub>2</sub> resulted into upfield-shift of -OH group from 10.3 ppm to 9.3 ppm, which was further intensified at elevated temperature (**Figure 3.10d**). The hydroxyl functional group (10.3 ppm) of the phosphonic acid corresponds to the tightly-bound hydrogen bond with other phosphonic acid molecules, which was broken after addition of PbBr<sub>2</sub> molecules to form new coordination (**Figure 3.10e**). In addition, the Pb 4f peak and the Br 3d peak of the BPA-induced structures are shifted to higher binding energy than in the 3D perovskite structure. This difference can be attributed to higher electronegativity of oxygen atoms compared with that of bromines, and



therefore modifying the Fermi level (**Figure 3.9c-d**). This can also be confirmed by UPS analysis, which showed that the *in situ* particle and *in situ* core/shell particle have much lower work function and higher energy offset between the work function and valence band (**Figure 3.10f, 3.11**). This difference can arise from gradual diminishing of self p-doping effects caused by ionic defects at the surface and within the crystal in 3D perovskite and *in situ* particle perovskite, which was suppressed in the *in situ* core/shell particle.



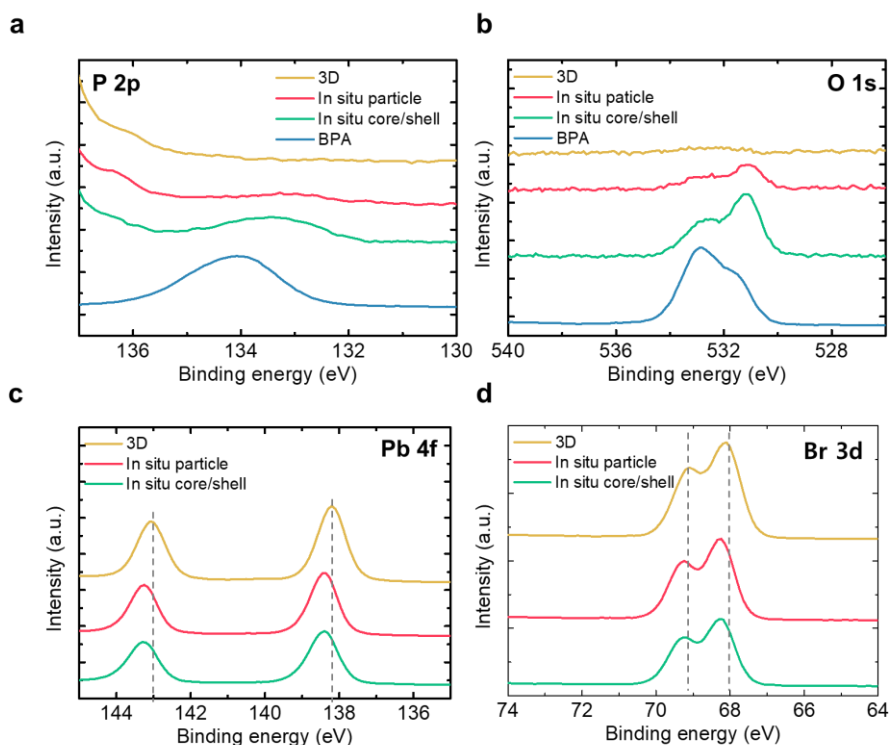


**Figure 3.9** a, P 2p, b, O 1s, c, Pb 4f, d, Br 3d XPS core level spectra of 3D, *in situ* particle, *in situ* core/shell structure perovskite thin films. The lowered proportion of the O 1s spectra at 531.0 eV in the *in situ* core/shell structure than that in the *in situ* particle structure can be understood as the presence of BPA molecules that cannot bind to the perovskite surface and can self-assemble to form macroparticles.



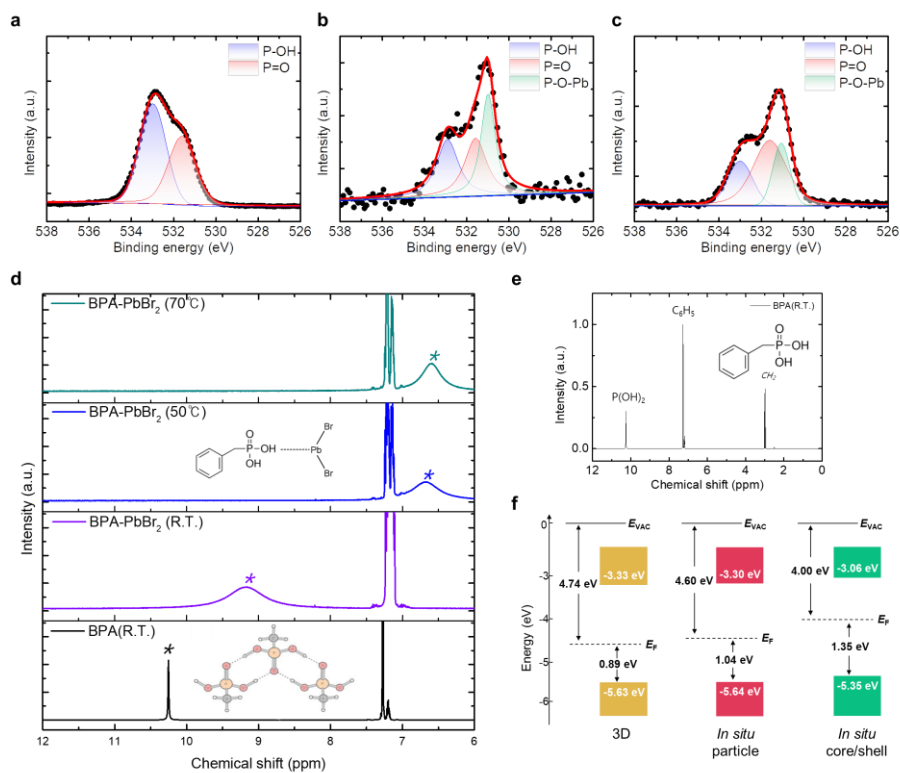


**Figure 3.10** a-c, O 1s XPS core-level spectra of a, BPA, b, *in situ* particle perovskite, c, *in situ* core/shell perovskite. d,  $^1\text{H}$  NMR spectra of BPA and BPA-PbBr<sub>2</sub> solution in DMSO d<sub>6</sub> with different temperature. e,  $^1\text{H}$  NMR spectra of BPA in DMSO d<sub>6</sub>. f, Energy level diagram of the pristine 3D, *in situ* particle, *in situ* core/shell perovskites obtained from parameters derived from UPS spectra.



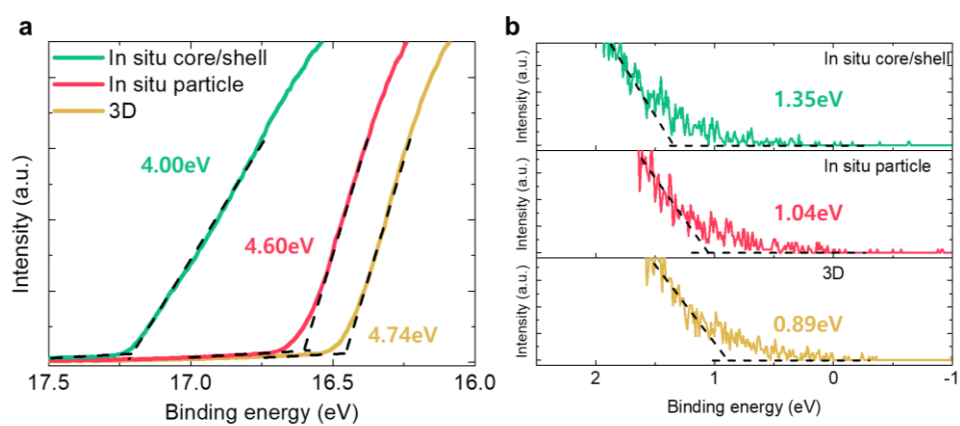


**Figure 3.11** UPS spectra of 3D, *in situ* particle, *in situ* core/shell perovskite films showing **a**, secondary cut-off and **b**, onset.



### Improvement in emission characteristics and defect passivation

We analyzed the luminescence properties of perovskite films by conducting photoluminescence quantum efficiency (PLQE) analysis. Perovskite thin films based on 3D and *in situ* particle structure showed comparably low internal quantum efficiency (IQE) of 30 % and 32 % respectively, *in situ* core/shell perovskite film showed greatly high IQE of 89 %, where the IQE values were estimated from measured external PLQE values by considering the reabsorption and photon recycling effect in thick perovskite film with high absorption coefficient (**Figure 3.12a, 3.13**). In addition, time-correlated single photon counting (TCSPC) measurement confirmed the longer PL lifetime in *in situ* particles and *in situ* core/shell structure compared to 3D perovskite (**Figure 3.12b**). The great improvement of IQE can be realized by reducing the particle size to strengthen charge confinement and defect density by passivating defects, i.e., undercoordinated Pb atoms and halide vacancies, which act as non-radiative recombination centers in the perovskite emitter. The improved charge confinement was confirmed by temperature-dependent PL analysis (**Figure 3.12c-e, 3.14**). From 3D to *in situ* particle and *in situ* core/shell structure, the peak center was blue-shifted, and the activation energy of PL quenching ( $E_a$ ) was increased from 90 meV to 220 meV; this change indicates that the *in situ* core/shell structure experiences improved confinement effect from the grain size reduction and passivation of shallow trap states.

To further confirm the passivation effect of BPA-induced nanostructure, we performed trap-density analysis by fabricating hole-only device (HOD) and analyzing the transport characteristics (**Figure 3.15**). HOD with device structure of



ITO/BuF-HIL/perovskite/MoO<sub>3</sub>/Au was utilized to characterize the charge transport properties of perovskite layer with efficient charge injection efficiency using BuF-HIL<sup>61,62</sup>. The current-voltage (I-V) characteristics of these HOD can be classified into three types of region according to the slope ( $k$ ), Ohmic region ( $k = 1$ ) in the low-injection regime, a trap-filled limited (TFL) region ( $k > 3$ ), and a space-charge limited current (SCLC) regime ( $k = 2$ )<sup>63</sup>. In this, the total trap state density inside the perovskite film can be calculated as

$$n_t = 2\varepsilon\varepsilon_0 V_{TFL} / (eL^2)$$

where  $n_t$  is the trap state density,  $V_{TFL}$  is the trap-filled limit voltage,  $L$  is the thickness of the perovskites,  $e$  is the elementary charge,  $\varepsilon_0$  and  $\varepsilon$  are the vacuum permittivity and relative permittivity, respectively. By estimating  $V_{TFL}$  as the intersection between ohmic region and TFL region, we calculate  $n_t = 2.66 \times 10^{16} \text{ cm}^{-3}$  for 3D,  $n_t = 2.36 \times 10^{16} \text{ cm}^{-3}$  for *in situ* particles,  $n_t = 1.37 \times 10^{16} \text{ cm}^{-3}$  for *in situ* core/shell perovskites. This result is evidence that the passivation effect of BPA-induced nanostructure in perovskite films also contributes to the increased luminescent efficiency.



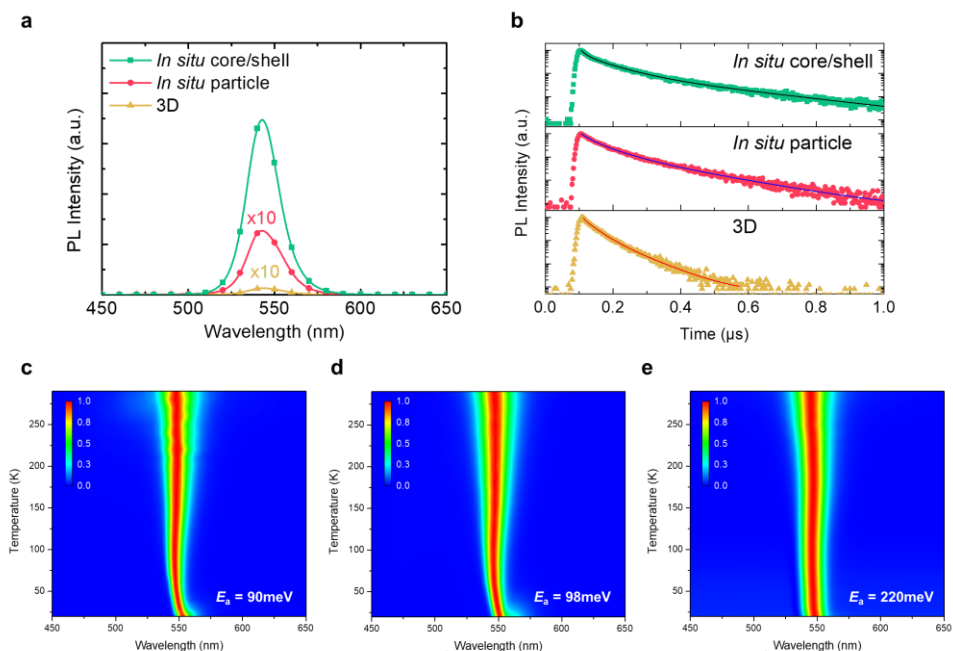


**Figure 3.12** **a**, PL spectrum of 3D, *in situ* particle, and *in situ* core/shell perovskite films. **b**, PL lifetime curves of 3D, *in situ* particle, and *in situ* core/shell perovskite films. **c-e**, Two-dimensional (2D) map of temperature-dependent PL spectra of 3D, *in situ* particle, *in situ* core/shell perovskite film respectively (normalized to peak value).



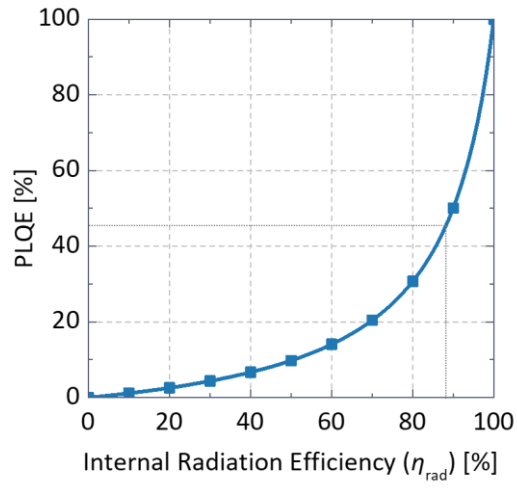


**Figure 3.13** External PLQE vs internal radiation efficiency ( $\eta_{\text{rad}}$ ) of perovskite film calculated considering the influence of perovskite reabsorption<sup>55,56</sup>. 3D, *in situ* particle, and *in situ* core/shell perovskite thin films exhibit the external PLQEs of 4.4 %, 4.8 %, and 46 %, which correspond to  $\eta_{\text{rad}}$  of 30 %, 32 %, 89 %, respectively.



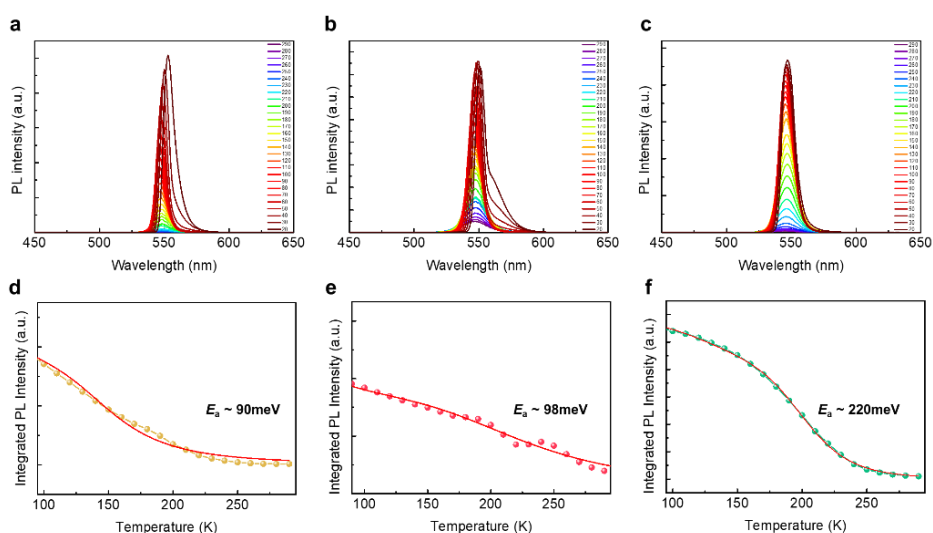


**Figure 3.14** Temperature-dependent PL spectrum and corresponding integrated PL intensity with calculated activation energy of **a,d**, 3D, **b,e**, *in situ* particle, **c,f**, *in situ* core/shell perovskite thin films.



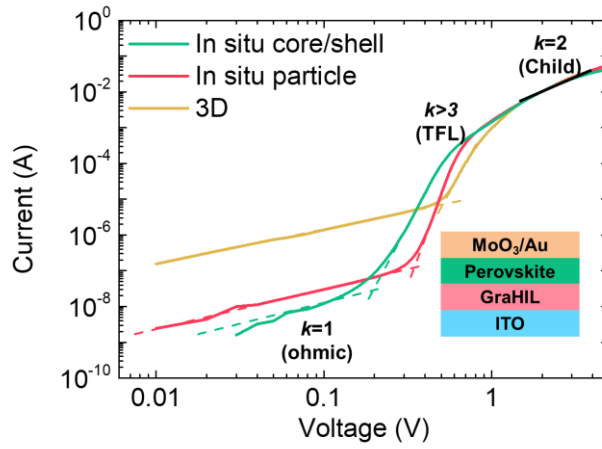


**Figure 3.15** Current density vs voltage for HODs under dark conditions. Inset: Device structure. SCLC fitting (dashed lines) shows the trap-filling limit voltage ( $V_{TFL}$ ), showing reduced trap densities of *in situ* particle structure and *in situ* core/shell structure.



## Light-emitting diode performance

Encouraged by the improved PL efficiency and greatly decreased trap density, we fabricated LEDs based on the BPA-induced nanostructured perovskites (**Figure 3.16a**). The PeLEDs based on *in situ* core/shell perovskites showed maximum current efficiency of 151 cd A<sup>-1</sup> and maximum EQE of 28.9 %, calculated using the full angular electroluminescence distribution (**Figure 3.16b-c**, **Figure 3.17**)<sup>53</sup>. In contrast to many previously-reported OLEDs and PeLEDs that have ultrathin EMLs (< 50 nm), this is a remarkably high EQE with an EML > 200 nm in devices in which the microcavity effects are diluted. The result emphasizes the important role of photon recycling effect in thick EMLs<sup>55,56,64,65</sup>. Optical simulation verified that our PeLEDs can reach EQE of 29 % with an aid of photon recycling effect (**Figure 3.18**). The detailed current-voltage-luminance characteristics are summarized in **Table 3.1**.

Perovskite	$V_{\text{turn-on}}$	$L_{\text{max}}$ (cd m <sup>-2</sup> ) (at bias (V))	$EQE_{\text{max}}$ (%) (at bias (V))	$CE_{\text{max}}$ (cd A <sup>-1</sup> ) (at bias (V))	$PE_{\text{max}}$ (lm W <sup>-1</sup> ) (at bias (V))
3D	2.31	20,271 (4.1)	3.66 (3.2)	22.41 (3.2)	19.8 (3.2)
<i>In situ</i> particle	2.31	149,331 (5.0)	8.29 (4.1)	41.05 (4.4)	27.2 (4.1)
<i>In situ</i> core/shell	2.22	473,990 (5.0)	28.9 (4.1)	151.1 (4.1)	112.8 (3.5)

**Table 3.1** Summarized electrical and luminance characteristics of PeLEDs.  $V_{\text{turn-on}}$ : Voltage at luminance of 1 cd m<sup>-2</sup>,  $L_{\text{max}}$ : maximum luminance,  $EQE_{\text{max}}$ : maximum EQE,  $CE_{\text{max}}$ : maximum current efficiency,  $PE_{\text{max}}$ : maximum power efficiency



Not likely the 3D PeLEDs with emission from ZADN layer, the *in situ* core/shell PeLEDs showed pure green emission from perovskite layer without any side-peak from other layer including ZADN, implying smooth morphology and charge confinement inside emitting layer without leakage current toward ZADN layer (**Figure 3.19c**). Also, the distribution of EQE and luminance obtained from 40 devices showed great reproducibility (**Figure 3.16d**, **Figure 3.19**). Especially, to manufacture efficient *in situ* core/shell PeLEDs with great reproducibility, the crystallization process of as-synthesized perovskite thin films must be controlled so that the grain size does not increase too much before the *in situ* reaction with BPA. When the A-NCP timing is not delayed and the processing temperature is kept < 18 °C, the grain size can be sufficiently small (< 100 nm), so that BPA can completely penetrate them during the reaction, and thereby provide nanostructures that are favorable for obtaining high-efficiency devices (**Figure 3.19i**). The PeLEDs showed high maximum brightness of 473,990 cd m<sup>-2</sup> whereas 3D PeLEDs and *in situ* particle PeLEDs showed maximum brightness of only 20,271 cd m<sup>-2</sup> and 149,331 cd m<sup>-2</sup>, respectively. The maximum brightness of *in situ* core/shell PeLEDs is the highest so far reported among PeLEDs based on any of the 3D, quasi-2D, or perovskite nanocrystals, and is even comparable with the highest brightness of state-of-the-art inorganic quantum dot (QD) LEDs (**Figure 3.16f**)<sup>66</sup>. In addition, they maintained the EQE value of ≥20 % under ultra-high brightness conditions from 50,000 cd m<sup>-2</sup> to 400,000 cd m<sup>-2</sup>, and exhibited very low roll-off of ~ 5 % at luminance of 400,000 cd m<sup>-2</sup> (**Table 3.2**).



Perovskite	EQE at 50,000 cd m <sup>-2</sup> (%)	EQE at 100,000 cd m <sup>-2</sup> (%)	EQE at 200,000 cd m <sup>-2</sup> (%)	EQE at 400,000 cd m <sup>-2</sup> (%)
3D	-	-	-	-
<i>In situ</i> particle	8.19	7.84	-	-
<i>In situ</i> core/shell	20.0	24.4	28.0	27.3

**Table 3.2** Summarized EQE at high-brightness operation of PeLEDs.

These results are remarkable considering that reported high-efficiency PeLEDs with EQE > 20 % have low brightness ( $\sim 10,000$  cd m<sup>-2</sup>) and large efficiency roll-off (>50 % at >10,000 cd m<sup>-2</sup>), because they use insulating ligands and therefore have thickness of emitting layer mostly < 30 nm to compensate its poor charge-transporting characteristics and to strengthen light outcoupling from the device (**Figure 3.16f**). In contrast, *in situ* core/shell perovskite is formed by *in situ* treatment of 3D perovskites without long insulating ligands, so both high efficiency and high brightness could be realized without significantly sacrificing charge transport. We also fabricated bright large-area PeLEDs (pixel size: 120 mm<sup>2</sup>) based on *in situ* core/shell structure. These PeLEDs had high uniformity and efficiency >20 %; these results show the potential of hybrid perovskite emitters for use in solid-state lighting and display applications (**Figure 3.16e**, **Figure 3.20**).

Finally, the operational lifetime of the PeLEDs were analyzed by applying a constant current and monitoring the luminance. Compared with the half-lifetime ( $T_{50}$ ) of 3D (0.2 h) and *in situ* particle (3.5 h) PeLEDs at initial brightness ( $L_0$ ) = 10,000 cd m<sup>-2</sup>, *in situ* core/shell PeLEDs showed much longer  $T_{50}$  of 14 h, due to greatly improved luminescent efficiency without sacrifice of charge-transport



properties (**Figure 3.21**). The operational lifetime of *in situ* core/shell PeLEDs was further measured at various  $L_0$  from 1,000 cd m<sup>-2</sup> to 200,000 cd m<sup>-2</sup> (**Figure 3.16g-h**). Specifically, *in situ* core/shell PeLEDs showed ultra-long  $T_{50}$  of 520 h at 1,000 cd m<sup>-2</sup>. By using the accelerated lifetime equation ( $L_0^n T_{50} = \text{constant}$ , where  $n$  is an acceleration factor)<sup>67,68</sup> with  $n = 1.68$  over 21 devices, we estimated the device's  $T_{50}$  at 100 cd m<sup>-2</sup> to be 31,808 h, which is, to our knowledge, the highest  $T_{50}$  estimated to date in PeLEDs (**Figure 4h-i, Table 3.3**).



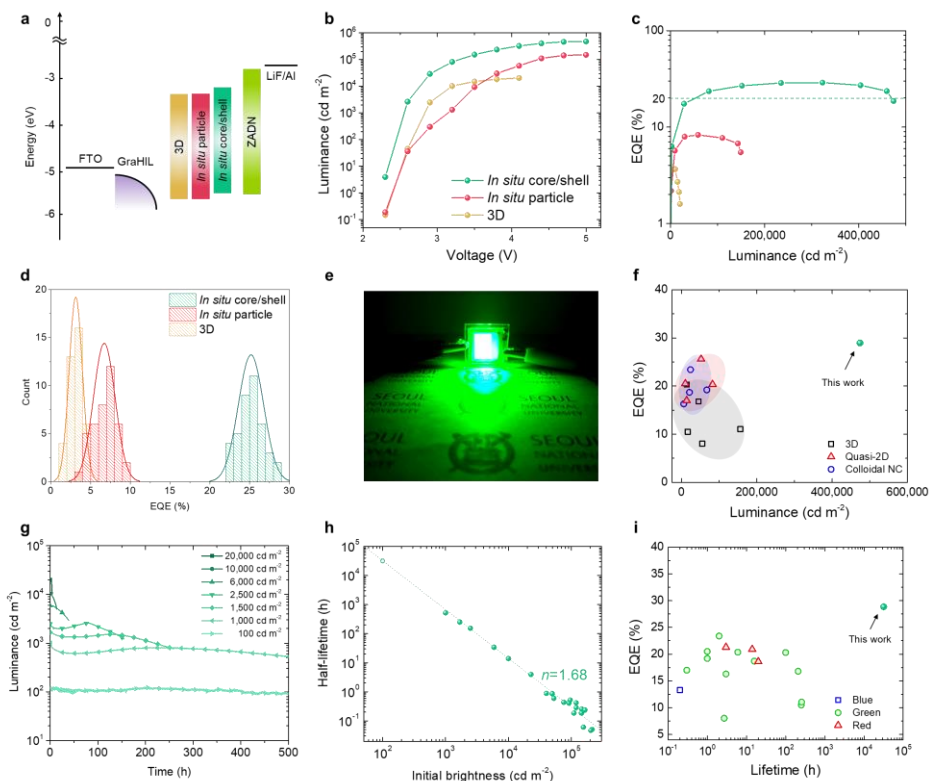


**Figure 3.16** **a**, schematics of energy diagram of PeLEDs. **b**, luminance vs voltage, **c**, EQE vs luminance, and **d**, EQE histogram of PeLEDs. **e**, photograph of operating large-area device. (pixel size: 120 mm<sup>2</sup>) **f**, Summary of the reported green PeLEDs characteristics based on maximum EQE and luminance. **g**, Luminance vs time of PeLEDs based on *in situ* core/shell perovskites at various initial brightness. **h**, half-lifetime vs brightness from accelerated lifetime test of *in situ* core/shell structure PeLEDs. **i**, Summary of the reported PeLEDs characteristics based on maximum EQE and estimated or measured half-lifetime at 100 cd m<sup>-2</sup>.



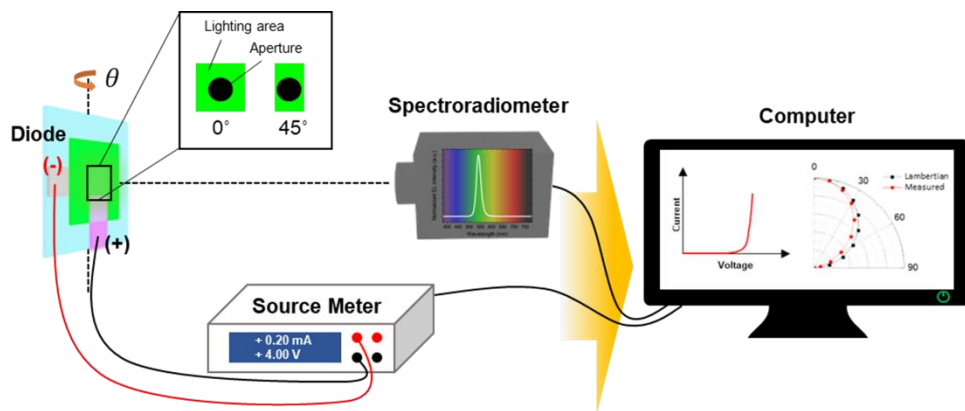


**Figure 3.17** Schematic illustration of device efficiency characterization setup for current-voltage-luminance measurement and goniometric measurement.



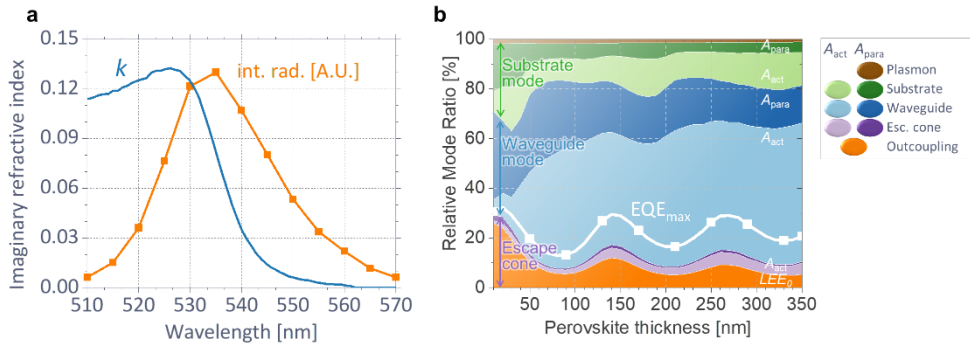


**Figure 3.18** **a**, Imaginary part of refractive index ( $k$ ) and internal radiation spectrum used for the simulation.  $n = 2.3$  is assumed for perovskite. **b**, Calculated maximum EQE ( $EQE_{max}$ ) considering the effect of photon recycling as a function of perovskite thickness in our device. Background colors represent the fractions of outcoupling, waveguide, substrate, and plasmon modes per each condition. Non-outcoupled photons are reabsorbed by either perovskite ( $A_{act}$ ) or parasitic layers ( $A_{para}$ ).



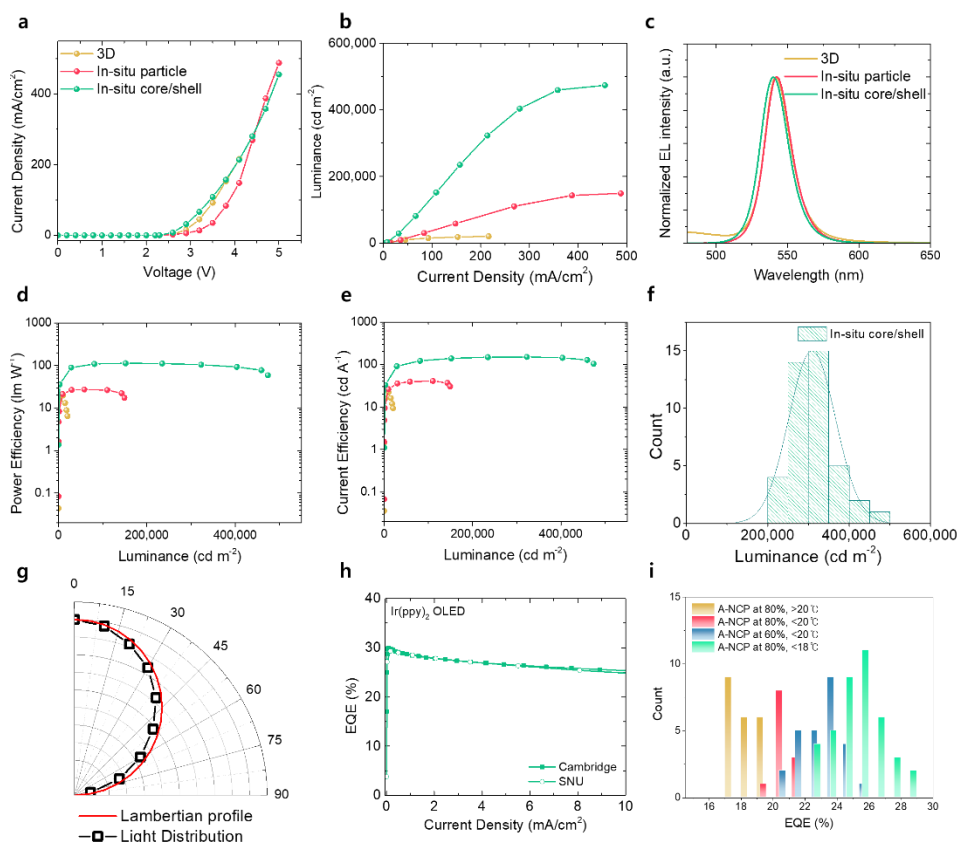


**Figure 3.19** **a**, Current density vs voltage; **b**, luminance vs current density; **c**, Normalized EL spectra; **d**, power efficiency vs luminance; **e**, current efficiency luminance of PeLEDs based on 3D, *in situ* particle, *in situ* core/shell structure. **f**, luminance histogram; **g**, Angle-dependent EL intensity of PeLEDs based on *in situ* core/shell structure. **h**, EQE versus vs density of OLEDs measured in our lab at Seoul National University (SNU) and at the Cavendish group at University of Cambridge. **i**, EQE histogram of the PeLEDs based on *in situ* core/shell structure with different processing condition. As the temperature of the glove box increases or the A-NCP process is delayed, the grain size of the spin-coated perovskite thin film increases, and this increase slows the penetration of the BPA solution into perovskite crystal and impedes their full conversion into the *in situ* core/shell structure.



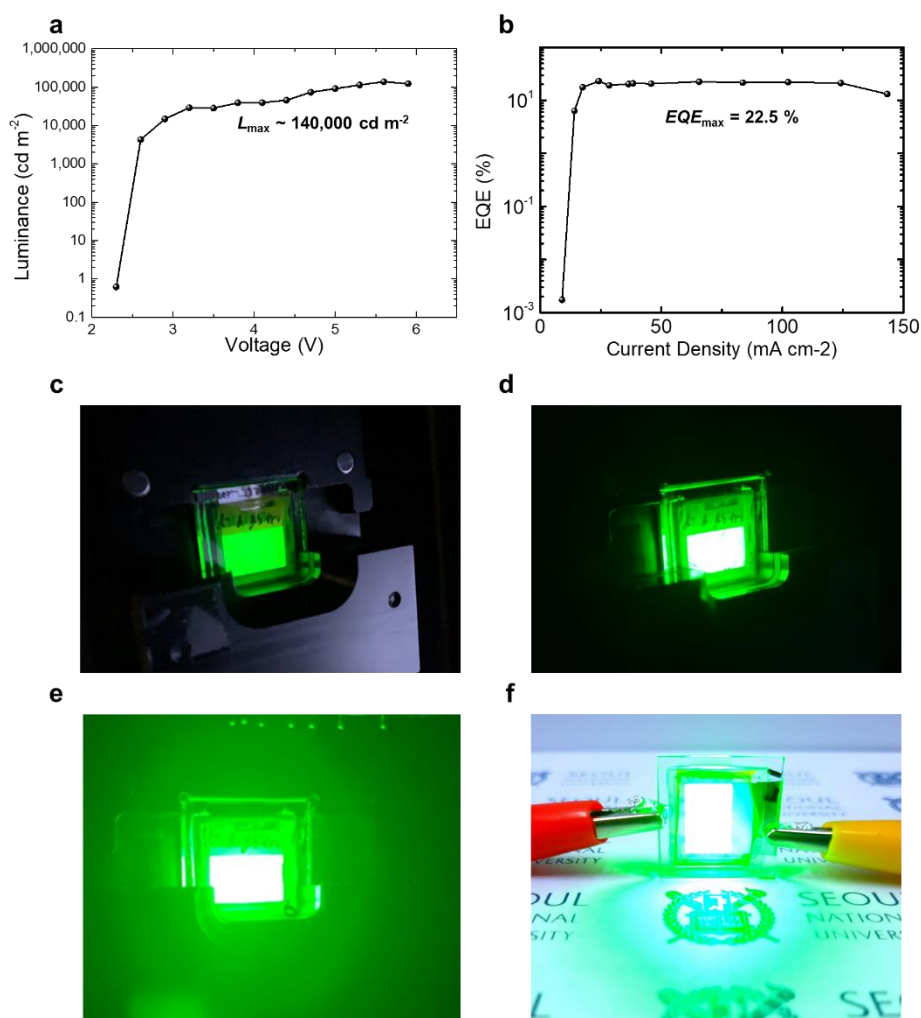


**Figure 3.20** **a**, luminance vs voltage, **b**, EQE vs current density of large-area devices based on *in situ* core/shell perovskites. Photographs of large-area devices (Pixel size:  $120 \text{ mm}^2$ ) operating at **c**,  $<10 \text{ cd m}^{-2}$ , **d**,  $1,000 \text{ cd m}^{-2}$ , **e**,  $100,000 \text{ cd m}^{-2}$ , and **f**,  $100,000 \text{ cd m}^{-2}$  under daylight, showing uniform emission over the pixel.



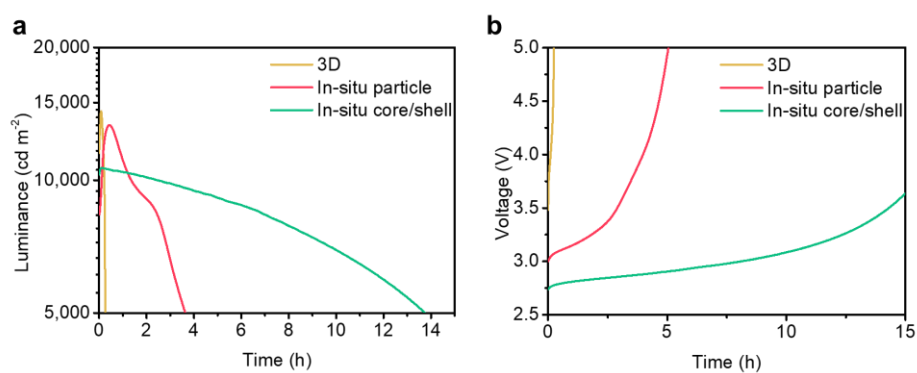


**Figure 3.21** **a**, Luminance vs time of PeLEDs based on 3D, *in situ* particle, and *in situ* core/shell perovskite at initial brightness of 10,000  $\text{cd m}^{-2}$  and **b**, corresponding driving voltage vs operation time.



Color	Type	Emitting layer	EQE (%)	L <sub>max</sub> (cd m <sup>-2</sup> )	T <sub>50</sub> (h)	Ref.
IR	Bulk	CsRbFAPbI <sub>3</sub>	15.84	493 W/Sr	60	40
IR	Bulk	FAPbI <sub>3</sub>	17.3	-	100	41
IR	Bulk	FAPbI <sub>3</sub>	18.6	334 W/Sr	682	42
IR	Bulk	FAPbI <sub>3</sub>	19.6	875 W/Sr	20	43
IR	Bulk	NMAFAPbI <sub>3</sub>	20.1	10 W/Sr	46	6
IR	Bulk	FAPbI <sub>3</sub>	20.7	390 W/Sr	20	44
R	Bulk	CsPbI <sub>2.8</sub> Br <sub>0.2</sub>	18.6	-	20	45
R	Bulk	FA <sub>0.33</sub> Cs <sub>0.67</sub> Pb(I <sub>0.7</sub> Br <sub>0.3</sub> ) <sub>3</sub>	20.9	180	14	46
G	Bulk	FAPbBr <sub>3</sub>	8.02	55,000	2.6	47
G	Bulk	CsPbBr <sub>3</sub>	10.5	16,436	250	48
G	Bulk	(Cs <sub>0.83</sub> Rb <sub>0.17</sub> ) <sub>0.95</sub> K <sub>0.05</sub> PbBr <sub>3</sub>	11.05	156,155	255	20
G	Bulk	CsPbBr <sub>3</sub>	16.8	45,306	208	49
G	Bulk	MABr/CsPbBr <sub>3</sub>	20.3	14,000	100	10
IR	Quasi-2D	PEAFACsPbI <sub>3</sub>	7.7	181.5 W/Sr	200	50
G	Quasi-2D	PEACsPbBr <sub>3</sub>	17	13,640	0.3	51
G	Quasi-2D	PEAMAPbBr <sub>3</sub>	20.36	82,840	6	38
G	Quasi-2D	BACsPbBr <sub>3</sub>	20.5	10,140	1	52
B	Quasi-2D	PEACsEAPbBr <sub>3</sub>	13.3	2,790	0.2	53
R	NP	CsPb <sub>0.64</sub> Zn <sub>0.36</sub> I <sub>3</sub>	17.4	3,260	-	54
R	NP	CsPb(Br/I) <sub>3</sub>	21.3	794	3	37
G	NP	FAPbBr <sub>3</sub>	16.3	5,980	3	55
G	NP	CsPbBr <sub>3</sub>	18.7	21,000	0.5 (L <sub>0</sub> =1,000cd m <sup>-2</sup> )	56
G	NP	FAPbBr <sub>3</sub>	19.2	67,115	1	57
G	NP	GA <sub>0.1</sub> FA <sub>0.9</sub> PbBr <sub>3</sub>	23.4	24,000	2.2	7
G	Bulk	(FA <sub>0.7</sub> MA <sub>0.1</sub> GA <sub>0.2</sub> ) <sub>0.87</sub> Cs <sub>0.13</sub> PbBr <sub>3</sub>	28.9	473,990	520 at 1,000 cd m <sup>-2</sup> (31,808 at 100cd m <sup>-2</sup> )	This work

**Table 3.3** Summary of the reported PeLEDs characteristics based on maximum EQE, maximum luminance, and half-lifetime.



### 3.4. Conclusion

We demonstrated *in situ* core/shell perovskite nanocrystals with size of ~10 nm by using *in situ* reaction of BPA molecule with 3D perovskite thin films. In the process of reaction, BPA molecules penetrated into large 3D perovskite crystals and split them into nanosized crystals, thus surrounding it as a core/shell structure. This *in situ* core/shell NP structure enabled increased carrier confinement, reduction in trap density, and increase in luminous efficiency without sacrificing the charge transport properties of 3D perovskites. As a result, simultaneously ultra-bright, efficient and stable PeLEDs with maximum current efficiency of 151 cd A<sup>-1</sup> (maximum EQE of 28.9 %), maximum luminance of ~470,000 cd m<sup>-2</sup>, very low efficiency roll-off of ~5 % at 400,000 cd m<sup>-2</sup>, and half-lifetime of 520 h at initial brightness of 1,000 cd m<sup>-2</sup> (estimated half-lifetime >30,000 h at 100 cd m<sup>-2</sup>) were demonstrated. These results suggest that PeLEDs are not only laboratory-level high-efficiency devices but are promising candidates for commercial self-emissive displays and lighting applications that require ultra-high brightness and long operational lifetime comparable to those of state-of-the-art OLEDs or QD LEDs.



# **Chapter 4. Unravelling the Origin of Catastrophic Failure in Perovskite LEDs**

## **4.1. Introduction**

MHPs have attracted great attention as a next-generation light emitter for their excellent color purity, high photoluminescence efficiency, and excellent electric properties<sup>3,69</sup>. However, the low stability of perovskite-based devices still acts as a fundamental limitation and hinders their potential for various long-term and commercial applications. MHPs intrinsically have soft ionic crystal, being very sensitive to moisture, heat, light, oxygen, electric field and easily undergo degradation. Also, PeLEDs tend to show much shorter operational lifetime than that of perovskite solar cells due to the severe ion migration occurring under intense electric field at much higher driving voltage for light emission<sup>70</sup>.

PeLEDs also suffers from catastrophic failure behavior, in which the device efficiency sharply decreases and the driving voltage increases abruptly, end with device breakdown during the lifetime test. This is very characteristic behavior contrast to the lifetime characteristics of OLEDs and polymer LEDs, which usually show steady exponential decay behavior (Figure 4.1a). Thus, PeLEDs have much unpredictable and shorter lifetime than expected. Although some reports exist on the interfacial reaction and environmental instability in PeLEDs, the degradation



mechanism and solution to overcome the catastrophic failure are still absent.

Here, we present a comprehensive degradation study on PeLEDs using in situ and ex situ techniques, by comparing conventional polycrystalline PeLEDs with severe ionic behavior versus in situ core/shell PeLEDs without noticeable ionic behavior. Overall chemical state, elemental depth profile, electronic property and photoluminescence characteristics in each degradation stage of catastrophic failure were analyzed (Figure 4.2). In order to unravel critical parameter that affects abrupt device degradation, we analyzed the degradation trend of each parameters that affect external quantum efficiency (EQE) of LED devices over time. EQE of LED device can be expressed as below<sup>69</sup>.

$$EQE = \eta_{\text{rad}} \times \eta_{\text{inj}} \times \eta_{\text{balance}} \times \eta_{\text{out}} \quad \text{Equ. (4-1)}$$

Here,  $\eta_{\text{rad}}$  is internal radiative efficiency,  $\eta_{\text{inj}}$  is the charge injection efficiency,  $\eta_{\text{balance}}$  is the charge balance factor, and  $\eta_{\text{out}}$  is the outcoupling efficiency. We show that self-accelerated ion diffusion process in PeLEDs result in catastrophic failure process by ion-induced failure cycle consist of ion diffusion, chemical corrosion of metallic electrode, increased injection barrier, and Joule heating (Figure 4.1b, c). In particular, the analysis was conducted focusing on the failure section where the slope of driving voltage rises rapidly and luminance drops rapidly over time, which is not likely observed in conventional OLEDs or polymer LEDs with steady saturation of driving voltage and exponential decay of luminance. The in situ core/shell PeLEDs without ion diffusion process toward metallic cathode eliminated the catastrophic failure behavior, evidencing the importance of suppressing ion migration for obtaining long-term stable PeLEDs without abrupt degradation process.



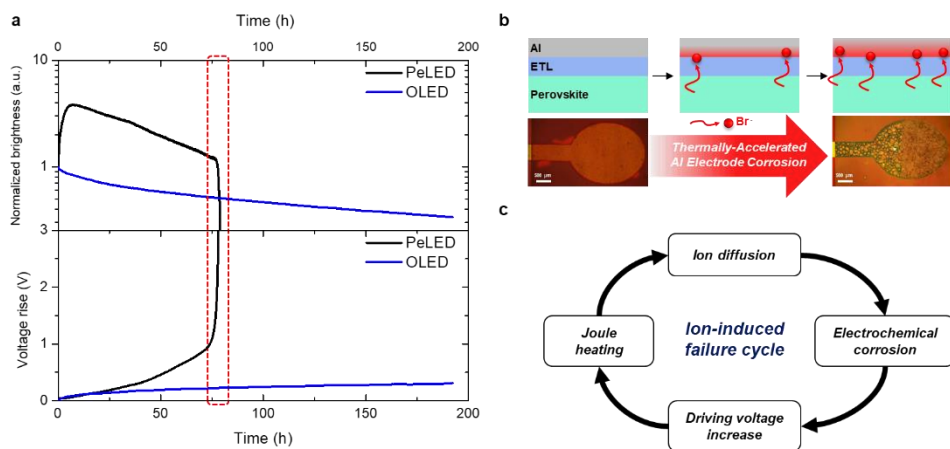


**Figure 4.1** **a**, luminance vs voltage of practical PeLEDs and OLEDs. Red boxed region indicates catastrophic failure occurring only in PeLEDs. **b**, Simplified scheme of ion diffusion from perovskite layer toward metallic electrode resulting in electrochemical corrosion of electrode. **c**, Ion-induced failure cycle as a working mechanism of catastrophic failure in PeLEDs.



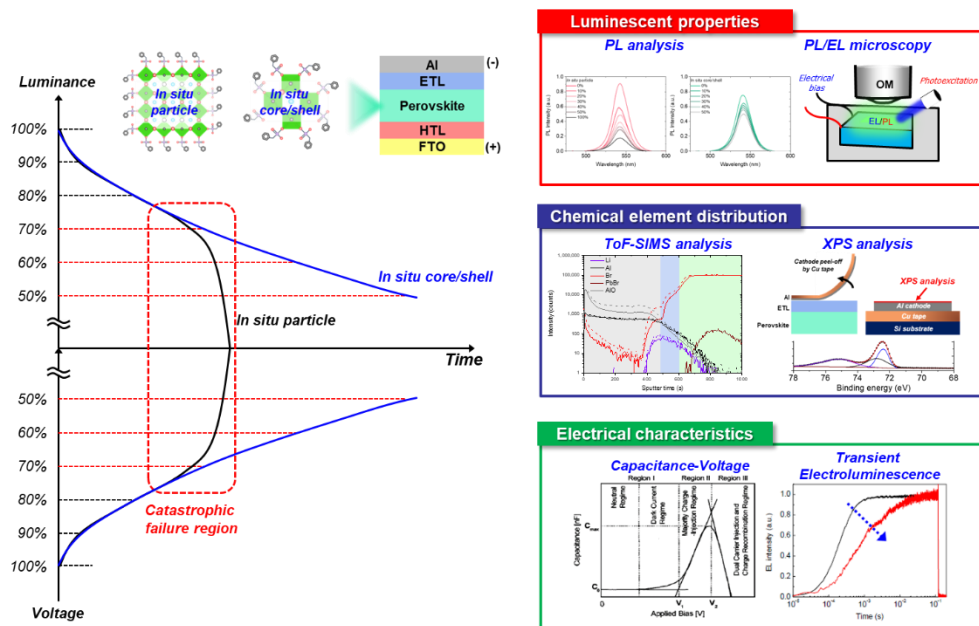


**Figure 4.2** Comprehensive degradation analysis procedure for step-by-step degradation stage of in situ particle with catastrophic failure and in situ core/shell PeLEDs without catastrophic failure.



## 4.2. Experimental

**Materials.** Formamidineum bromide (FABr, > 99.99 %), Methylammonium bromide (MABr, > 99.99 %), and Guanidineum bromide (GABr, > 99.99 %) were purchased from Dyesol. Cesium bromide (CsBr), BPA, tetrafluoroethylene-perfluoro3,6-dioxo-4-methyl-7-octene-sulfonic acid copolymer (PFI), Chlorobenzene (CB), Tetrahydrofuran (THF), and Molybdenum oxide ( $\text{MoO}_3$ ) were purchased from Sigma-Aldrich. Lead bromide ( $\text{PbBr}_2$ ) was purchased from TCI Co., Ltd. 2,2',2''-(1,3,5-Benzinetriyl)-tris(1-phenyl-1H-benzimidazole) (TPBi) was purchased from OSM. 9,10-di(naphthalene-2-yl)anthracen-2-yl-(4,1-phenylene)(1-phenyl-1H-benzo[d]imidazole) (ZADN) was purchased from Shinwon Chemtrade Co., Ltd. Lithium fluoride (LiF) was supplied from Foosung Co., Ltd. Unless otherwise stated, all materials are used without purification.

**Preparation of MHP solution.** The mixed-cation precursor,  $((\text{FA}_{0.7}\text{MA}_{0.1}\text{GA}_{0.2})_{0.87}\text{Cs}_{0.13}\text{PbBr}_3)$  was prepared by dissolving stoichiometric ratio of each of FABr, MABr, GABr, CsBr and  $\text{PbBr}_2$  (molar ratio  $(\text{FABr} + \text{MABr} + \text{GABr} + \text{CsBr}) : \text{PbBr}_2 = 1.15 : 1$ ) in DMSO at a concentration of 1.2 M<sup>8,52</sup>. In case of precursor solution for the *in situ* particle perovskite, 10 mol. % of BPA relative to  $\text{PbBr}_2$  were added. The solution was stirred overnight in  $\text{N}_2$ -filled glove box before use.

**Fabrication of PeLEDs.** Pre-patterned FTO(200 nm) glasses (25 mm X 25 mm) were sonicated in acetone and 2-propanol for 15 min each sequentially, then boiled



in 2-propanol for 30 min. The surface of FTO substrates undergo ultraviolet-ozone (UVO) treatment to achieve hydrophilic surface. We used a previously-described method to synthesize a HIL (BufHIL) that has a gradient work function (WF), by inducing self-organization of PEDOT:PSS (CLEVIOS P VP AI4083) and tetrafluoroethylene-perfluoro3,6-dioxo-4-methyl-7-octene-sulfonic acid copolymer (PFI); the solution was spin-coated to form 75-nm thickness, then annealed at 150 °C for 30 min<sup>21</sup>. After baking, the substrates were transferred into a N<sub>2</sub>-filled glove box for deposition of MHP layer. MHP films with thickness of 270 nm were deposited by spin-coating the precursor solution at 6000 rpm with additive-assisted nanocrystal pinning (NCP) process:<sup>2</sup> during the second spin step, TPBi-dissolved CB solution was dropped onto the spinning perovskite film. For synthesis of *in situ* core/shell perovskite film, BPA dissolved in THF solution was loaded on top of the perovskite, followed by reaction time of 30s and direct spin-drying afterward. Samples were then moved to the vacuum chamber (<10<sup>-7</sup> Torr) to sequentially deposit ZADN (45 nm), LiF (1.2 nm), and Al (100 nm). The active area of 4.9 mm<sup>2</sup> was defined by shadow masking during deposition of cathode. Finally, the fabricated PeLEDs were encapsulated under N<sub>2</sub> atmosphere by using a glass lid and UV-curable epoxy resin.

**Perovskite film characterizations.** Images of the surfaces were obtained using a field-emission scanning electron microscope (SEM) (SUPRA 55VP). XPS spectra were measured by using a photoelectron spectrometer (AXIS-Ultra DLD, Kratos Inc.). A monochromatic Al-K $\alpha$  line (1486.6 eV) was used for XPS. Steady-state photoluminescence (PL) spectra was measured by using a JASCO FP8500 spectrofluorometer. For transient PL decay measurement, a system composed of a



streak camera (c10627, Hamamatsu Corp.) and a nitrogen pulse laser (337 nm, 20 Hz, Usho Inc.) was used. For single-carrier device analysis, MoO<sub>3</sub> (30nm) and Au (50nm) were thermally deposited sequentially onto FTO / BufHIL / perovskite and encapsulated in N<sub>2</sub> atmosphere to obtain the current-voltage curve using a Keithley 236 source measurement unit. For ion conductivity analysis, Au electrode was thermally deposited onto Si / perovskite with inter-distance of 50μm for lateral electric field.

### **Characterization on efficiency of PeLEDs.**

Electroluminescence efficiencies of the fabricated PeLEDs were measured using a Keithley 236 source measurement unit and a Minolta CS-2000 spectroradiometer. External quantum efficiency of PeLEDs was calculated by measuring full angular electroluminescence distribution<sup>53</sup>.

### **Lifetime analysis of PeLEDs.**

Operational lifetime of PeLEDs was measured under constant current condition by simultaneously tracking brightness and applied voltage using a M760 Lifetime Analyzer (Mcscience Inc.) with control computer.

### **Perovskite device characterizations.**

The capacitance-voltage characteristics were measured by SP-200 electrochemical impedance spectrometer (EIS, BioLogic). The simultaneous photoluminescence and electroluminescence image was obtained by homemade setup combined with optical



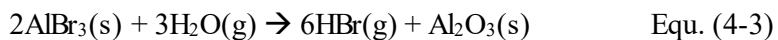
microscope, SP-200, and 405nm continuous-wave laser (MDL-III, Changchun New Industries Optoelectronics Tech. Co., Ltd.). The temperature-luminance-voltage characteristics were tracked by using Keithley 236 source measurement unit and Minolta CS-2000 spectroradiometer.



## 4.3. Result and Discussion

### Vertical ionic redistribution after catastrophic failure

In order to analyze the characteristics of the device by the presence or absence of catastrophic failure behavior, we conducted chemical element analysis before and after operating the in situ particle PeLEDs with failure behavior and the in situ core/shell device without failure behavior. We first observed the vertical ionic distribution through Time-of-Flight Secondary Ion Mass Spectroscopy (ToF-SIMS) analysis. The vertical layer of FTO / BuF-HIL / Perovskite / ZADN / LiF-Al can be distinguished through the ionic distribution of each layer's ions detected by ToF-SIMS of Fresh devices<sup>71,72</sup>. In the case of the in situ particle device, the elemental peak of AlO and Br at interface between Al and ZADN layer were greatly increased after  $L_{50}$  point with catastrophic failure occurred (Figure 4.3a). The increase of Br element can be ascribed to ionic diffusion of dissociated Br anions from the perovskite layer to the Al cathode layer, while other elements such as Pb, Li, and F remained in their original positions without severe vertical redistribution. In particular, the peak of the AlO greatly increased at the interface of Al and ZADN, which can be attributed to halide-induced electrochemical corrosion of Al electrode triggered by Br atom. The reaction scheme can be expressed as the following formula<sup>73</sup>.



In this case, aluminum bromide ( $\text{AlBr}_3$ ) is spontaneously formed by highly exothermic reaction, which can further reacts with trace amount of moisture



molecules, leading to the formation of HBr gas and aluminum oxide ( $\text{Al}_2\text{O}_3$ ) thus detected as AlO element on ToF-SIMS measurement. On the other hand, in the case of the in situ core/shell PeLEDs, the AlO and Br element peaks didn't show significant difference after device operation without failure behavior (Figure 4.3b). The result confirms that the halide diffusion into the Al cathode triggers electrochemical corrosion and causes instability. The electrochemical corrosion of the Al cathode and the formation of HBr gas were further confirmed through optical microscope (OM) and cross-sectional scanning electron microscope (SEM) analysis. In the case of the in situ particle device, a circular shape corrosion was confirmed on the Al cathode after device operation, which was not shown at all with in situ core/shell PeLEDs (Figure 4.4a-d). Also, in the top-view and cross-sectional SEM images, the thin Al cathode was swelled out due to the formation of HBr gas at interface between Al cathode and ZADN during the corrosion cycle. (Figure 4.4e-g).



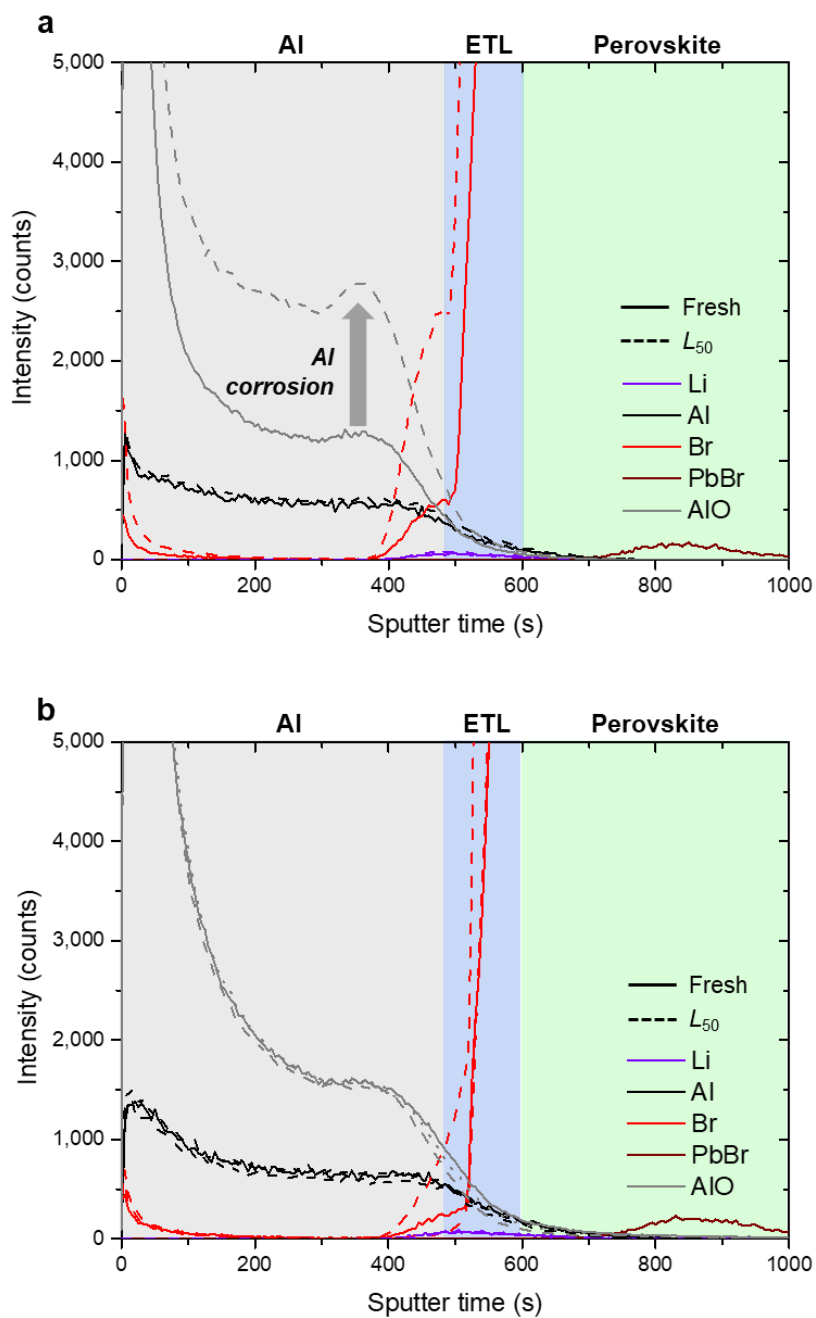


**Figure 4.3** TOF-SIMS ionic depth profiles for fresh and  $L_{50}$  devices of **a**, in situ particle PeLEDs and **b**, in situ core/shell PeLEDs, respectively.



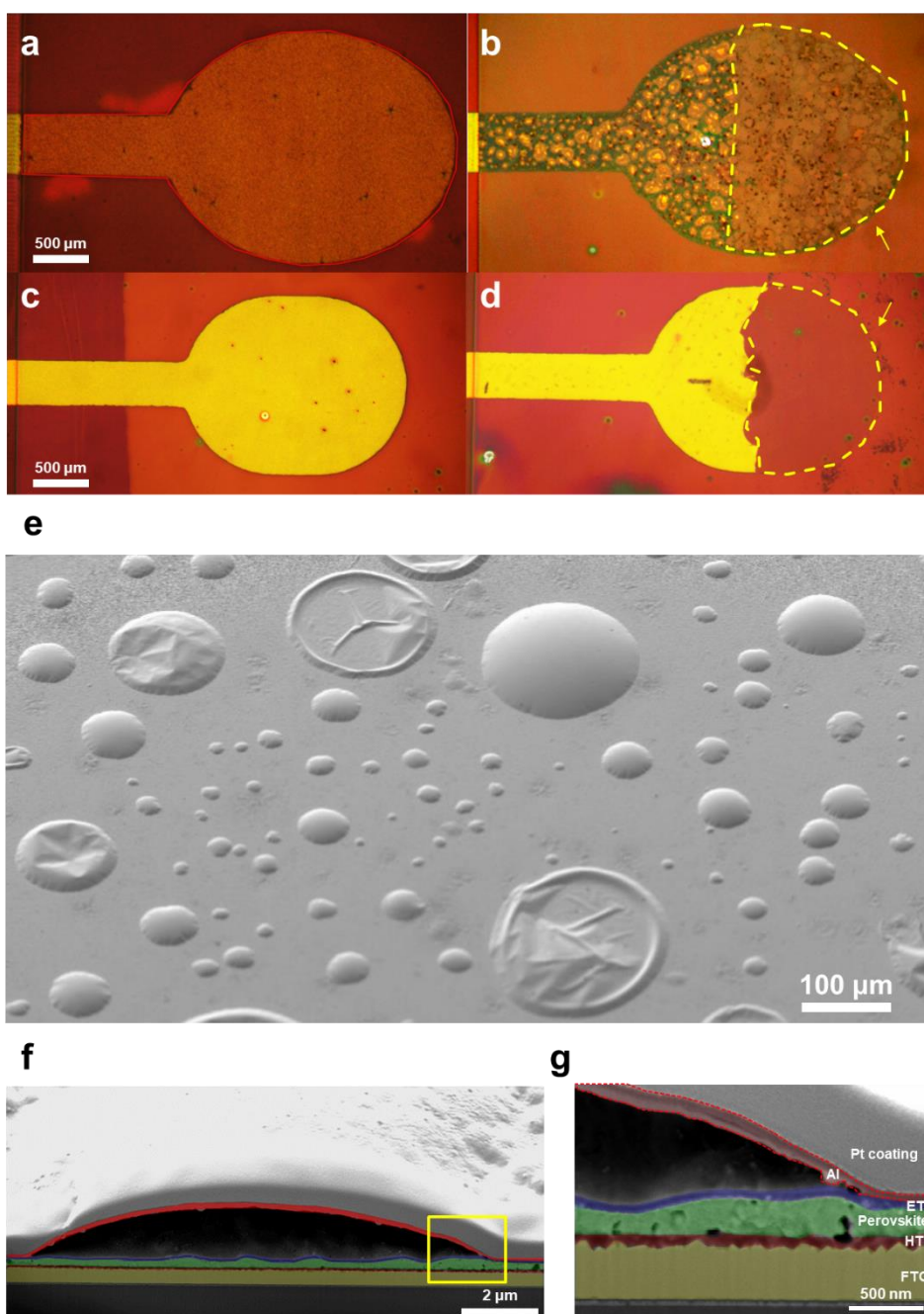


**Figure 4.4** OM image of the Al cathode before and after 50% of degradation of in situ particle PeLEDs (a,b) and in situ core/shell PeLEDs (b-d). e, top-view, f-g, cross-sectional view of Al cathode from in situ particle PeLEDs after device degradation.



### **Electrochemical corrosion of aluminum cathode during catastrophic failure**

The detailed chemical state of the interface at Al cathode and ZADN layer was analyzed by X-ray photoemission spectroscopy (XPS) analysis<sup>74</sup>. For characterization of the Al/ZADN surface during the catastrophic failure process, each PeLEDs were driven up to  $L_{70}$ ,  $L_{60}$ , and  $L_{50}$  point where the catastrophic failure occurred. By delaminating the Al cathode with Cu tape, it was attached to the conductive ITO substrate to reveal the Al/ZADN interface surface to top for XPS analysis. In the in situ particle PeLEDs, the amount of Br peak (69.5eV) starts to increase from the  $L_{70}$  point-just before the catastrophic failure behavior begins-and at the same time, new characteristic peak (76eV) in the high energy region corresponding to  $\text{AlBr}_x$  appeared (Figure 4.5a)<sup>75</sup>. These peaks became more and more intense as the operation stage goes to  $L_{60}$  and  $L_{50}$ , and at the  $L_{50}$  point, the Br element even increased to ~14% of the total atomic percentage including Al elements, evidencing severe ion diffusion toward Al/ZADN interface. At the  $L_{50}$  point, the total atomic percent of  $\text{AlBr}_x$  did not increase compared to that of the  $L_{60}$  point; this can be understood as the above-described reaction of  $\text{AlBr}_3$  reacting with trace amount of moisture and reduced to  $\text{Al}_2\text{O}_3$ . For the in situ core/shell PeLEDs, the peaks corresponding to Br and  $\text{AlBr}_x$  were not observed at all before and after device operation, which is consistent result with the ToF-SIMS depth profile (Figure 4.5b). From the ToF-SIMS and XPS analysis, it can be evidenced that the diffusion of halide ions toward Al cathode only contributed to degradation behavior on in situ particle PeLEDs.



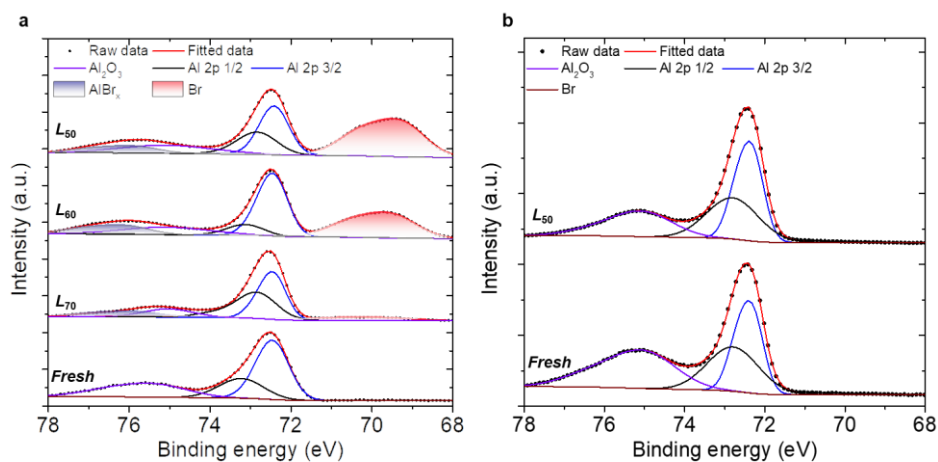


**Figure 4.5** Individual XPS spectra obtained at the delaminated Al cathode after operation of **a**, in situ particle and **b**, in situ core/shell PeLEDs during each step-by-step degradation process.



## Charge injection characteristics during catastrophic failure

To investigate the injection efficiency of PeLEDs during catastrophic failure process, we conducted capacitance-voltage (C-V) and EL spectra analysis to show the effect of corrosion of Al cathode on charge injection characteristics and its effect on device degradation. For the C-V measurement with increasing voltage, representative 3 stages can be observed; 1) the region where charge is not injected enough and only the geometric capacitance is observed, 2) the region where the majority charge is injected and accumulated to show increasing capacitance as the voltage increases, 3) the region where minority charge is injected and recombination zone is formed, thus the capacitance decreases due to light emission<sup>76</sup>. In this case, 3) the voltage at the maximum capacitance point ( $V_{\max}$ ) where light emission begins can be used as an important parameter to show the difference in charge injection characteristics and charge balance.

First, in the case of the in situ particle PeLEDs,  $V_{\max}$  was kept constant at 2.4V from the fresh state to the  $L_{80}$  stage with slight decrease in capacitance (Figure 4.6a). This indicates that the degradation process of PeLEDs is not affected by charge injection characteristics until  $L_{80}$  stage but by only degradation of internal quantum efficiency, charge mobility, defect density, and so on in perovskite layer. On the other hand, in the catastrophic failure section of  $L_{70} \sim L_{50}$ ,  $V_{\max}$  gradually increased to 2.5V ( $L_{70}$ ), 3.2V ( $L_{60}$ ), and >4V ( $L_{50}$ ). In particular, at the  $L_{50}$  stage after catastrophic failure, the contribution of the increasing capacitance due to charge accumulation is much stronger than that of the decreasing capacitance due to light emission, so the capacitance increases infinitely without maximum point thus cannot be estimated. On the other hand, in the case of in situ core/shell PeLEDs, the low  $V_{\max}$



value of  $\sim 2.0\text{V}$  and low capacitance were maintained even after degradation toward  $L_{50}$ , showing negligible difference on charge injection property, not likely in the in situ particle PeLEDs (Figure 4.6 b,c). Furthermore, from the EL spectra of in situ particle PeLEDs according to the degradation stage, emission of ZADN is observed at the range of 450 to 500 nm in the  $L_{60}$  and  $L_{50}$  stage after the catastrophic failure occurred (Figure 4.6d). The emission at ZADN layer indicates the electron injection is greatly reduced and the charge balance became worse, thus the recombination zone shifts toward ZADN with hole accumulation at the perovskite/ZADN interface. Through these results, it can be seen that ion diffusion toward Al cathode can rapidly decrease the device efficiency by inhibiting electron injection from electrochemical corrosion of LiF/Al cathode (Figure 4.6e).



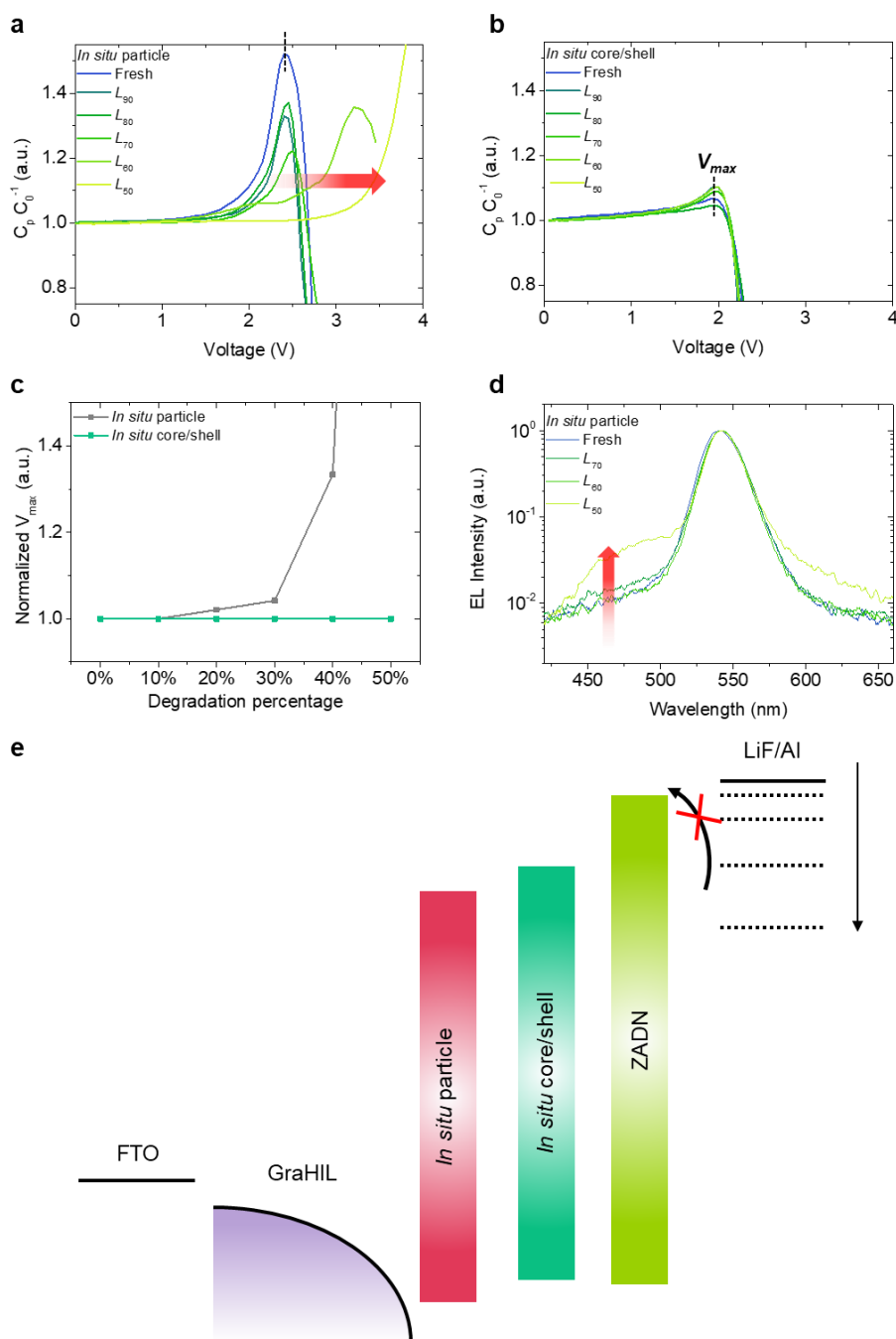


**Figure 4.6** Capacitance-voltage characteristics of **a**, *in situ* particle PeLEDs and **b**, *in situ* core/shell PeLEDs during each step of degradation processes. **c**, Normalized  $V_{max}$  of PeLEDs with each step of degradation processes. **d**, Normalized EL spectra of *in situ* particle PeLEDs during each step of degradation processes. **e**, Schematic diagram on energy level of PeLEDs and carrier injection.



## Effect of Joule heating on catastrophic failure

When the charge injection efficiency is delayed as the catastrophic failure progresses, the driving voltage for injecting the constant current must be greatly increased. In particular, the increase in driving voltage linearly increases the Joule heating in the form of  $P=VI$ , and leads to a large increase in ion diffusivity in the perovskite layer with a low ion migration barrier, accelerating electrode corrosion.

To correlate the effect of Joule heating with catastrophic failure, we simultaneously tracked the luminance, voltage, and temperature with operation time. The temperature of the LED devices can be typically estimated from fitting the high-energy tail of the EL spectra as junction temperature ( $T_j$ )<sup>77</sup>. We calculated  $T_j$  from the EL spectra according to the operating time of in situ particle and in situ core/shell PeLEDs (Figure 4.7). By operating under a constant current condition of 2 mA with initial brightness of  $\sim 10,000 \text{ cd m}^{-2}$ , the in situ particle device showed rapid increase in driving voltage, and the temperature rose rapidly from room temperature ( $\sim 20^\circ \text{C}$ ) to  $\sim 60^\circ \text{C}$ . On the other hand, the in situ core/shell PeLEDs maintained low temperature of  $< 25^\circ \text{C}$  even after degradation toward  $L_{50}$  stage. Although the driving temperature does not reach  $> 100^\circ \text{C}$ , where the possible thermal decomposition of perovskite layer can be facilitated<sup>12</sup>, it can greatly accelerate ion diffusion, which is a thermally activated process. We estimated the increase in ion diffusivity by measuring the ion conductivity of in situ particle perovskite thin film. Ion diffusivity can be estimated by the following formulas<sup>78</sup>.

$$\sigma = c_i q_i \mu_i \quad \text{Equ. (4-4)}$$



$$\mu_i = \frac{q_i D_i}{k_B T} \quad \text{Equ. (4-5)}$$

$$\sigma T = \sigma_0 e^{-\frac{E_a}{k_B T}} \quad \text{Equ. (4-6)}$$

$$\frac{q_i^2 c_i}{k_B} D_i = \sigma T = \sigma_0 e^{-\frac{E_a}{k_B T}} \quad \text{Equ. (4-7)}$$

Where  $\sigma$  is the ion conductivity,  $c_i$  is the concentration of ion,  $\mu_i$  is the ion mobility,  $q_i$  is charge of the ion,  $D_i$  is the ion diffusion coefficient,  $E_a$  is activation energy of ion migration,  $k_B$  is the Boltzmann constant. Thus, the ionic diffusivity can be directly correlated with the  $\sigma T$  from equ. (4-6). We fabricated a lateral device and analyzed the ion conduction properties of the perovskite layer. Above 250K, the activation energy of ion migration of in situ particle perovskite well matched with the previously reported value of  $\sim 0.2\text{eV}$ <sup>47</sup>. The ion diffusivity with increasing temperature during device operation increased about 4 times larger than that of ion diffusivity at room temperature (Figure 4.8). From this, we can confirm that ion diffusion causes self-accelerated process of catastrophic failure through electrode corrosion, driving voltage increase, and Joule heating, resulting in a positive feedback that returns to increase in ion diffusivity again.

To confirm the cycle of the self-accelerated process, we compared the device lifetime under low temperature conditions that can eliminate the Joule heating effect (Figure 4.9). As expected, the catastrophic failure process presented in room-temperature operation of in situ particle PeLEDs was not shown at all; With a constant current of 2 mA, the in situ particle PeLEDs showed very stable exponential lifetime decay over >30 hours even with an initial luminance of  $>10,000\text{cd m}^{-2}$ . From



this, it can be estimated that the catastrophic failure can be suppressed through various strategies that overcoming the each components of failure cycle such as ion diffusion, Joule heating, electrode corrosion, and increased charge injection barrier.



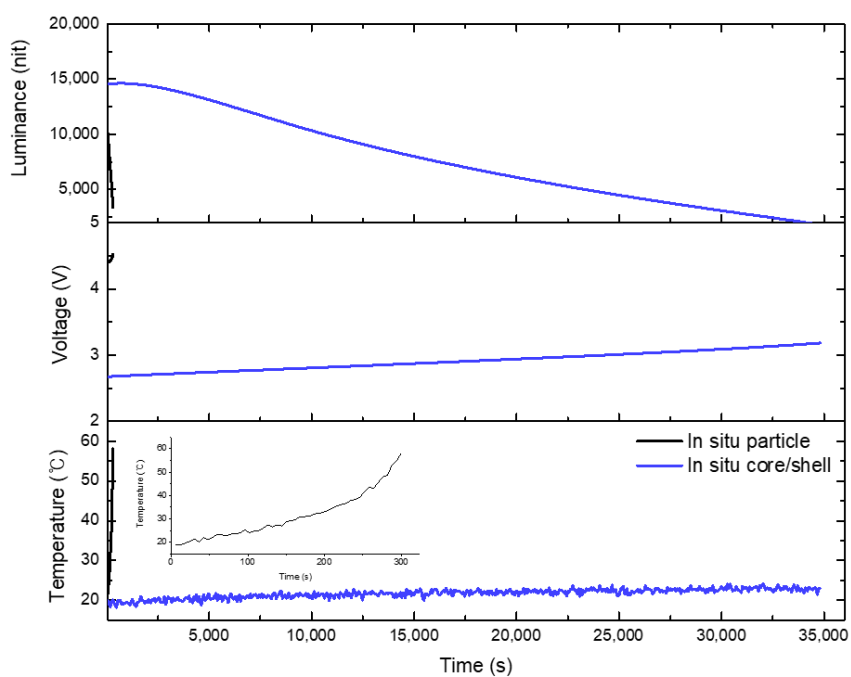


**Figure 4.7** Luminance, voltage, temperature vs time of in situ particle, in situ core/shell PeLEDs operated at constant current of 2 mA. Inset at the bottom shows magnified view of temperature vs time curve of in situ particle PeLEDs.



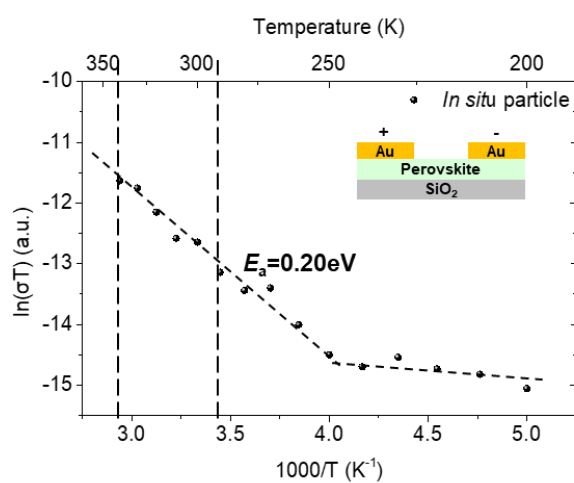


**Figure 4.8** Temperature-dependent ion conductivity of the in situ particle perovskite film.



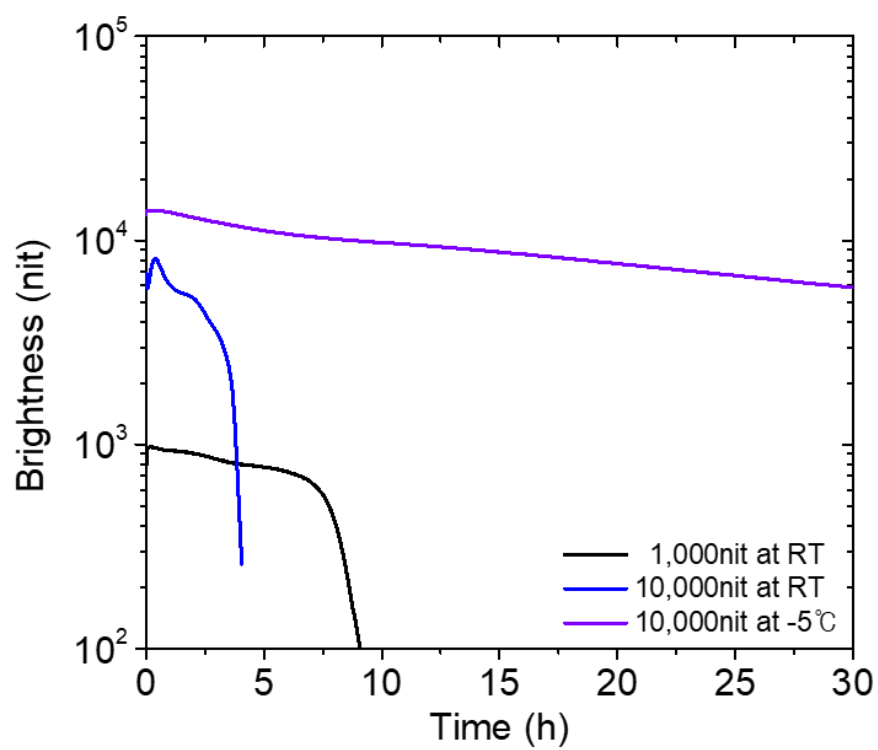


**Figure 4.9 a**, luminance vs time of in situ particle PeLEDs under various brightness at room temperature and controlled low temperature.



### **Photoluminescence characteristics during catastrophic failure process**

Finally, in order to analyze the change in internal radiative efficiency in the catastrophic failure process, photoluminescence (PL) properties were compared for each degradation stage. The steady-state PL spectra of each degradation-progressed active area was measured (Figure 4.10). The in situ particle PeLEDs initially showed rise in PL intensity due to ion-induced trap-filling. After overshoot on PL intensity, it showed a gradual decrease in PL intensity, which was similar with the case in in situ core/shell PeLED. In particular, the in situ particle PeLED did not show an abrupt decrease in the catastrophic failure range of 30% to 50%. Through this, it was confirmed that the internal radiative efficiency did not show an abrupt decrease in the degradation process of PeLEDs and didn't cause catastrophic failure.



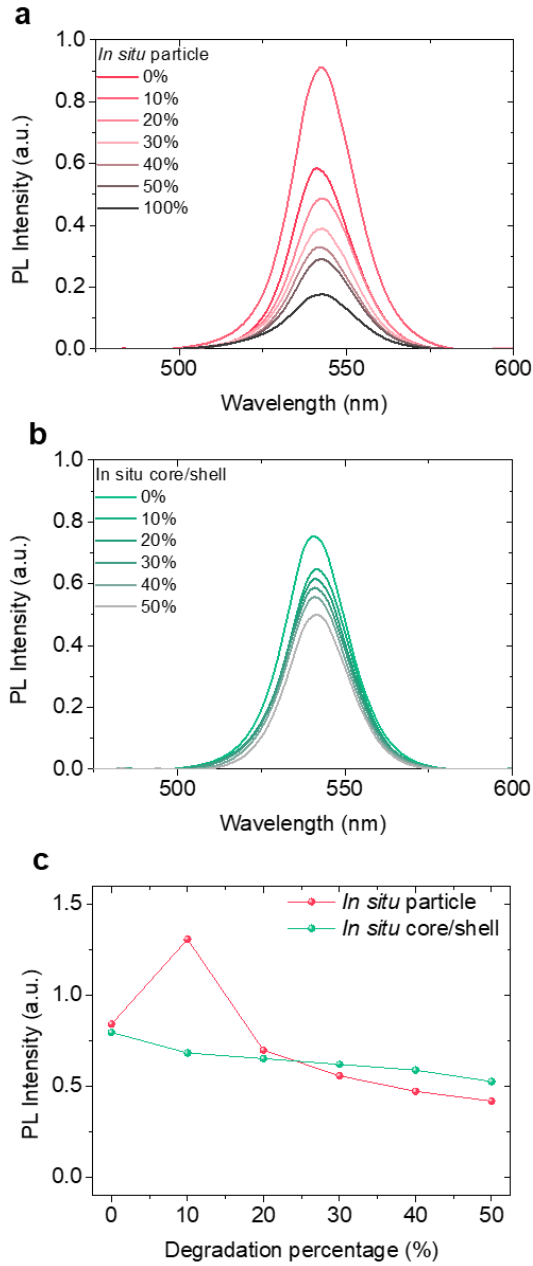


**Figure 4.10** **a**, luminance vs voltage, **b**, EQE vs current density of large-area devices based on *in situ* core/shell perovskites. Photographs of large-area devices (Pixel size: 120 mm<sup>2</sup>) operating at **c**, <10 cd m<sup>-2</sup>, **d**, 1,000 cd m<sup>-2</sup>, **e**, 100,000 cd m<sup>-2</sup>, and **f**, 100,000 cd m<sup>-2</sup> under daylight, showing uniform emission over the pixel.



### **Summarized self-accelerated catastrophic failure in PeLEDs**

Through the above analysis, we could propose a comprehensive scheme for degradation mechanism of PeLEDs during catastrophic failure process. There are many variables that affect device efficiency in the LED lifetime decay process including internal radiative efficiency, charge injection efficiency, charge balance, and outcoupling efficiency; but among them, factor with a rapid decrease in the fastest time scale would be most critical factor for device degradation. In PeLEDs with ion diffusion, unlike OLEDs, there is a degradation process by ionic motion, and it was confirmed that this ion-induced failure cycle causes catastrophic failure by causing rapidly decreasing charge injection efficiency (Figure 4.11). This abruptly occurs on a time scale that is much faster than parameters such as internal quantum efficiency and outcoupling efficiency, making PeLEDs exhibit very short and unpredictable lifetime decay compared to OLEDs. These characteristics can be solved by overcoming phenomena such as ion diffusion, Joule heating, and electrode corrosion.



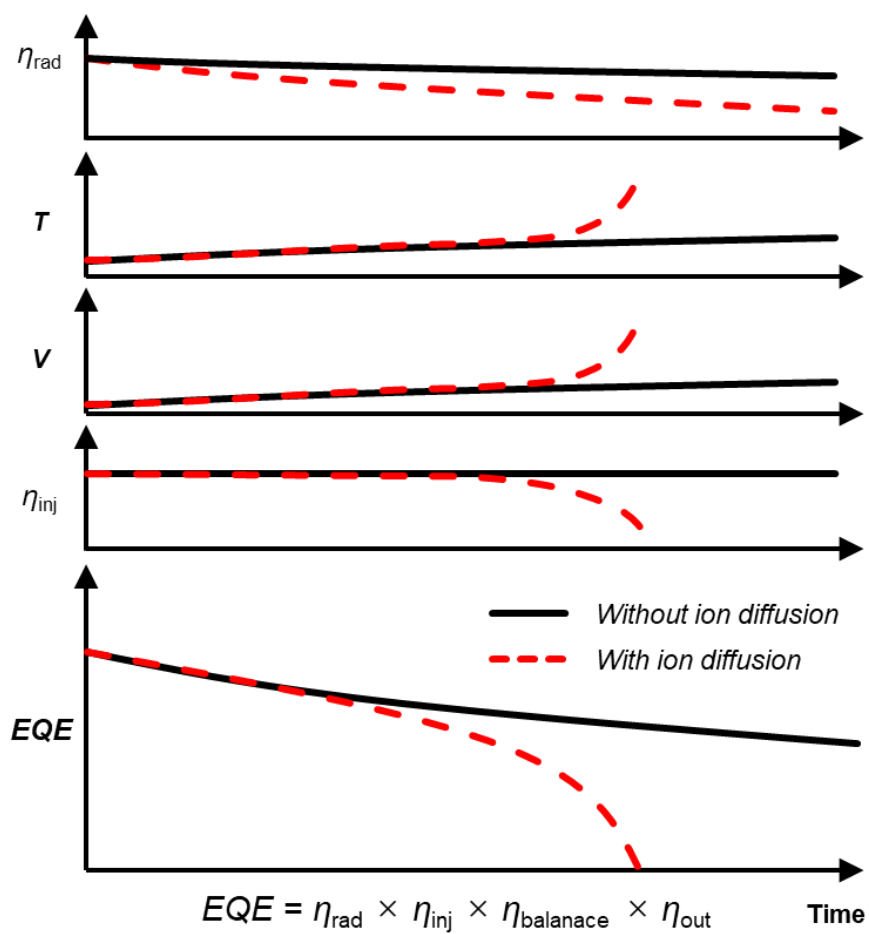


**Figure 4.11** Summarized graph of catastrophic failure process with ion diffusion in PeLEDs.



## 4.4. Conclusion

In conclusion, we could unravel the origin of catastrophic failure that causes abrupt device breakdown in PeLEDs by analyzing and comparing the various parameters affecting the emission characteristics of PeLEDs at each degradation stage. The unique ionic behavior in PeLEDs caused electrochemical corrosion of metallic electrode, increase in driving voltage, and Joule heating, which eventually leads to thermally-activated faster ion diffusion, resulting in a self-accelerated degradation cycle. It was shown that this failure cycle can be overcome by suppressing ion diffusion using stable in situ core/shell structure, and can also be implemented by suppressing Joule heating and using electrochemically robust electrodes. This result suggests that suppressing unpredictable device breakdown of PeLEDs can realize stable long-term applications such as OLEDs.



# Chapter 5. Summary and Conclusion

Perovskite light emitting diodes have been in the limelight as next-generation displays due to their excellent color purity and improved high luminous efficiency within a short period of time, but little research has been conducted to improve their driving stability and reveal the degradation mechanism. In order to overcome the lifespan limit of PeLEDs and reveal the degradation mechanism, we introduced a new core/shell structural material system and conducted a comprehensive degradation analysis. As a result, it was possible to present PeLEDs deterioration mechanism and realize PeLEDs with an excellent drive life that overcomes the deterioration mechanism.

In chapter 2, a long-lifetime PeLEDs with suppressed ion migration was implemented by implementing a 3D/2D core/shell structured perovskite light emitters using a stable 2D perovskite structure. The benzylamine additive was able to form a 2D perovskite through a proton transfer reaction in the perovskite precursor solution and a core/shell structure surrounding the 3D perovskite. As a result, it was possible to implement a perovskite light emitting diode that has a drive lifespan that is 21 times longer than that of conventional 3D perovskite-based light emitting diodes and shows stable device operation unaffected by ion movement.

In chapter 3, a core/shell structured nanocrystalline perovskite was synthesized by introducing an in situ process using post-treatment of a short acidic ligand. Perovskite nanocrystals with a particle size as small as 10 nm and whose surface was surrounded by BPA ligand could simultaneously satisfy a high internal quantum efficiency of 89% and a fast charge mobility similar to that of a 3D



perovskite structure. As a result, we could realize ideal PeLEDs that simultaneously satisfies high luminous efficiency ( $\text{EQE} = 28.9\%$ ), ultra-high brightness ( $>470,000 \text{ cd m}^{-2}$ ), and long device lifetime ( $>30,000 \text{ h}$  at  $100 \text{ cd m}^{-2}$ ).

In chapter 4, we identified the mechanism of catastrophic failure, which shows a rapid decrease in efficiency in the lifetime curve of PeLEDs. By comparing the previously discussed stable in situ core/shell perovskite and 3-dimensional polycrystalline perovskite-based LEDs, we could analyze the mechanism by which ion diffusion rapidly reduces the lifetime of PeLEDs. In particular, the existence of degradation mechanism accelerated by the positive feedback of ion diffusion toward electrodes in perovskite crystals, corrosion of metal electrodes by ions, increase in driving voltage, and subsequent Joule heating was identified.

We believe that the development of core/shell structured perovskite emitters provides a promising direction for improving the stability of PeLEDs. In addition, by revealing that the mechanism of catastrophic failure-which greatly hindered the stability of the PeLEDs-can be eliminated by suppressing the ion diffusion of the perovskite structure, we believe in the possibility of realizing a stable PeLEDs like commercial OLEDs or inorganic QD LEDs. Through this, the perovskite light emitters can be used as an excellent high-color purity display material that can be applied to commercial application, not simply an unstable material at the laboratory level.



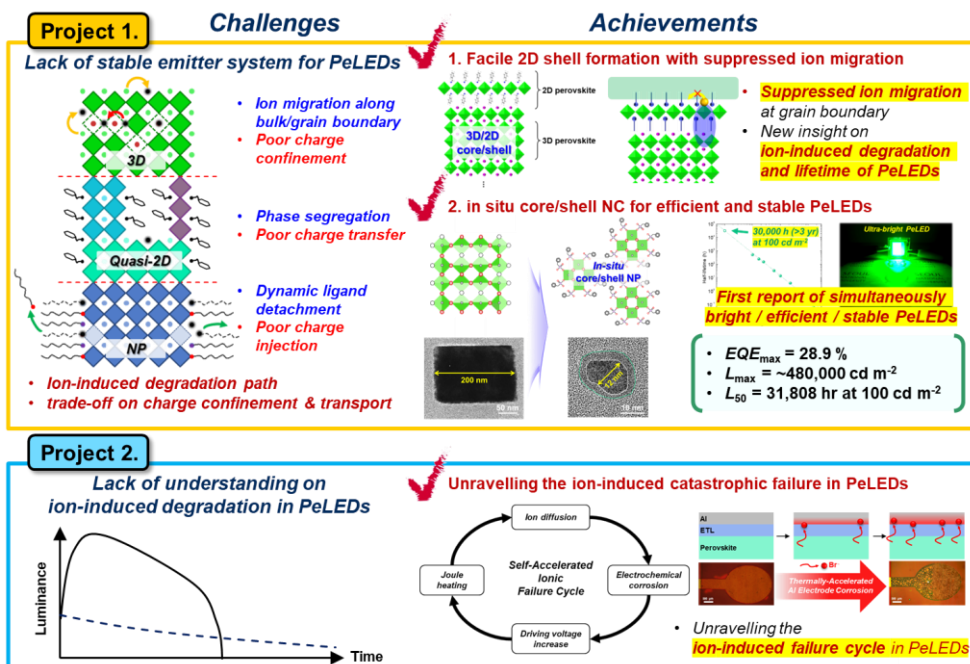


**Figure 5.1** Strategies to overcome the lifetime limitation of perovskite light-emitting diodes.



# Bibliography

1. Tan, Z.-K. *et al.* Bright light-emitting diodes based on organometal halide perovskite. *Nat. Nanotechnol.* **9**, 687–692 (2014).
2. Cho, H. *et al.* Overcoming the electroluminescence efficiency limitations of perovskite light-emitting diodes. *Science* (80-. ). **350**, 1222–1225 (2015).
3. Kim, Y.-H., Cho, H. & Lee, T.-W. Metal halide perovskite light emitters. *Proc. Natl. Acad. Sci. U. S. A.* **113**, 11694–11702 (2016).
4. Xiao, Z. *et al.* Efficient perovskite light-emitting diodes featuring nanometre-sized crystallites. *Nat. Photonics* **11**, 108–115 (2017).
5. Lin, K. *et al.* Perovskite light-emitting diodes with external quantum efficiency exceeding 20 per cent. *Nature* **562**, 245–248 (2018).
6. Yang, X. *et al.* Efficient green light-emitting diodes based on quasi-two-dimensional composition and phase engineered perovskite with surface passivation. *Nat. Commun.* **9**, 2–9 (2018).
7. Zhao, B. *et al.* High-efficiency perovskite–polymer bulk heterostructure light-emitting diodes. *Nat. Photonics* **12**, 783–789 (2018).
8. Kim, Y.-H. *et al.* Comprehensive defect suppression in perovskite nanocrystals for high-efficiency light-emitting diodes. *Nat. Photonics* **15**, 148–155 (2021).
9. Kim, Y.-H., Kim, J. S. & Lee, T. Strategies to Improve Luminescence Efficiency of Metal-Halide Perovskites and Light-Emitting Diodes. *Adv. Mater.* **31**, 1804595 (2019).



10. Park, M.-H. *et al.* Boosting Efficiency in Polycrystalline Metal Halide Perovskite Light-Emitting Diodes. *ACS Energy Lett.* **4**, 1134–1149 (2019).
11. Hassan, Y. *et al.* Ligand-engineered bandgap stability in mixed-halide perovskite LEDs. *Nature* **591**, 72–77 (2021).
12. Cho, H., Kim, Y.-H., Wolf, C., Lee, H.-D. & Lee, T.-W. Improving the Stability of Metal Halide Perovskite Materials and Light-Emitting Diodes. *Adv. Mater.* **30**, 1704587 (2018).
13. Liu, M., Matuhina, A., Zhang, H. & Vivo, P. Advances in the Stability of Halide Perovskite Nanocrystals. *Materials (Basel)*. **12**, 3733 (2019).
14. Dong, Y. *et al.* Bipolar-shell resurfacing for blue LEDs based on strongly confined perovskite quantum dots. *Nat. Nanotechnol.* **15**, 668–674 (2020).
15. Hassan, Y. *et al.* Ligand-engineered bandgap stability in mixed-halide perovskite LEDs. *Nature* **591**, 72–77 (2021).
16. Wehrenfennig, C., Eperon, G. E., Johnston, M. B., Snaith, H. J. & Herz, L. M. High Charge Carrier Mobilities and Lifetimes in Organolead Trihalide Perovskites. *Adv. Mater.* **26**, 1584–1589 (2014).
17. Herz, L. M. Charge-Carrier Mobilities in Metal Halide Perovskites: Fundamental Mechanisms and Limits. *ACS Energy Lett.* **2**, 1539–1548 (2017).
18. Xu, W. *et al.* Rational molecular passivation for high-performance perovskite light-emitting diodes. *Nat. Photonics* **13**, 418–424 (2019).
19. Meggiolaro, D., Mosconi, E. & De Angelis, F. Formation of Surface Defects Dominates Ion Migration in Lead-Halide Perovskites. *ACS Energy Lett.* **4**, 779–785 (2019).



20. Zhang, L. *et al.* Suppressing Ion Migration Enables Stable Perovskite Light-Emitting Diodes with All-Inorganic Strategy. *Adv. Funct. Mater.* **30**, 1–8 (2020).
21. Kim, Y.-H. *et al.* Multicolored Organic/Inorganic Hybrid Perovskite Light-Emitting Diodes. *Adv. Mater.* **27**, 1248–1254 (2015).
22. Cao, Y. *et al.* Perovskite light-emitting diodes based on spontaneously formed submicrometre-scale structures. *Nature* **562**, 249–253 (2018).
23. Zhao, L. *et al.* Electrical Stress Influences the Efficiency of CH<sub>3</sub>NH<sub>3</sub>PbI<sub>3</sub> Perovskite Light Emitting Devices. *Adv. Mater.* **29**, 1605317 (2017).
24. Zhao, L. *et al.* In Situ Preparation of Metal Halide Perovskite Nanocrystal Thin Films for Improved Light-Emitting Devices. *ACS Nano* **11**, 3957–3964 (2017).
25. Yuan, Y. & Huang, J. Ion Migration in Organometal Trihalide Perovskite and Its Impact on Photovoltaic Efficiency and Stability. *Acc. Chem. Res.* **49**, 286–293 (2016).
26. Lin, Y. *et al.* Suppressed Ion Migration in Low-Dimensional Perovskites. *ACS Energy Lett.* **2**, 1571–1572 (2017).
27. Eames, C. *et al.* Ionic transport in hybrid lead iodide perovskite solar cells. *Nat. Commun.* **6**, 7497 (2015).
28. Tress, W. *et al.* Understanding the rate-dependent J-V hysteresis, slow time component, and aging in CH<sub>3</sub>NH<sub>3</sub>PbI<sub>3</sub> perovskite solar cells: The role of a compensated electric field. *Energy Environ. Sci.* **8**, 995–1004 (2015).
29. Yun, J. S. *et al.* Critical role of grain boundaries for ion migration in formamidinium and methylammonium lead halide perovskite solar cells.



- Adv. Energy Mater.* **6**, 1–8 (2016).
30. Shang, Y., Li, G., Liu, W. & Ning, Z. Quasi-2D Inorganic CsPbBr<sub>3</sub> Perovskite for Efficient and Stable Light-Emitting Diodes. (2018) doi:10.1002/adfm.201801193.
  31. Tsai, H. *et al.* Stable Light-Emitting Diodes Using Phase-Pure Ruddlesden-Popper Layered Perovskites. *Adv. Mater.* **30**, 1704217 (2018).
  32. Yantara, N. *et al.* Designing Efficient Energy Funneling Kinetics in Ruddlesden–Popper Perovskites for High-Performance Light-Emitting Diodes. *Adv. Mater.* **30**, 1800818 (2018).
  33. Quan, L. N. *et al.* Tailoring the Energy Landscape in Quasi-2D Halide Perovskites Enables Efficient Green-Light Emission. *Nano Lett.* **17**, 3701–3709 (2017).
  34. Byun, J. *et al.* Efficient Visible Quasi-2D Perovskite Light-Emitting Diodes. *Adv. Mater.* **28**, 7515–7520 (2016).
  35. Park, M.-H. H. *et al.* Unravelling additive-based nanocrystal pinning for high efficiency organic-inorganic halide perovskite light-emitting diodes. *Nano Energy* **42**, 157–165 (2017).
  36. Miyadera, T. *et al.* Crystallization Dynamics of Organolead Halide Perovskite by Real-Time X-ray Diffraction. *Nano Lett.* **15**, 5630–5634 (2015).
  37. Koh, T. M. *et al.* Nanostructuring Mixed-Dimensional Perovskites: A Route Toward Tunable, Efficient Photovoltaics. *Adv. Mater.* **28**, 3653–3661 (2016).
  38. Yuan, M. *et al.* Perovskite energy funnels for efficient light-emitting diodes.



- Nat. Nanotechnol.* **11**, 872–879 (2016).
39. He, C. *et al.* Turn on fluorescence sensing of vapor phase electron donating amines via tetraphenylporphyrin or metallophenylporphyrin doped polyfluorene. *Chem. Commun.* **46**, 7536–7538 (2010).
  40. Bube, R. H. Trap Density Determination by Space-Charge-Limited Currents. *J. Appl. Phys.* **33**, 1733–1737 (1962).
  41. Dong, Q. *et al.* Electron-hole diffusion lengths > 175 um in solution-grown CH<sub>3</sub>NH<sub>3</sub>PbI<sub>3</sub> single crystals. *Science* **347**, 967–970 (2015).
  42. Shi, D. *et al.* Low trap-state density and long carrier diffusion in organolead trihalide perovskite single crystals. *Science* (80-. ). **347**, 519–522 (2015).
  43. Saidaminov, M. I. *et al.* High-quality bulk hybrid perovskite single crystals within minutes by inverse temperature crystallization. *Nat. Commun.* **6**, 7586 (2015).
  44. Lim, K.-G., Choi, M.-R. & Lee, T.-W. Improvement of both efficiency and stability in organic photovoltaics by using water-soluble anionic conjugated polyelectrolyte interlayer. *Mater. Today Energy* **5**, 66–71 (2017).
  45. Kim, H.-S. & Park, N.-G. Parameters Affecting I–V Hysteresis of CH<sub>3</sub>NH<sub>3</sub>PbI<sub>3</sub> Perovskite Solar Cells: Effects of Perovskite Crystal Size and Mesoporous TiO<sub>2</sub> Layer. *J. Phys. Chem. Lett.* **5**, 2927–2934 (2014).
  46. Almora, O. *et al.* Capacitive Dark Currents, Hysteresis, and Electrode Polarization in Lead Halide Perovskite Solar Cells. *J. Phys. Chem. Lett.* **6**, 1645–1652 (2015).
  47. Han, T. H. *et al.* Surface-2D/Bulk-3D Heterophased Perovskite Nanograins for Long-Term-Stable Light-Emitting Diodes. *Adv. Mater.* **32**, 1–10 (2020).



48. Mosconi, E. & De Angelis, F. Mobile Ions in Organohalide Perovskites: Interplay of Electronic Structure and Dynamics. *ACS Energy Lett.* **1**, 182–188 (2016).
49. Strehlow, H. Fundamentale Kinetik: Basic Chemical Kinetics. Von H. Eyring, S. H. Lin and S. M. Lin. John Wiley & Sons, New York - Chichester - Brisbane - Toronto 1980. VU, 493 S., zahlr. Formeln, geb., £ 20,-. *Nachrichten aus Chemie, Tech. und Lab.* **28**, 754–755 (1980).
50. Lee, J. H., Lee, J.-H., Kong, E.-H. & Jang, H. M. The nature of hydrogen-bonding interaction in the prototypic hybrid halide perovskite, tetragonal CH<sub>3</sub>NH<sub>3</sub>PbI<sub>3</sub>. *Sci. Rep.* **6**, 21687 (2016).
51. Bader, R. Atoms in Molecules – A Quantum Theory, Clarendon. (1990).
52. Cho, H. *et al.* High-Efficiency Polycrystalline Perovskite Light-Emitting Diodes Based on Mixed Cations. *ACS Nano* **12**, 2883–2892 (2018).
53. Jeong, S.-H. *et al.* Characterizing the Efficiency of Perovskite Solar Cells and Light-Emitting Diodes. *Joule* **4**, 1206–1235 (2020).
54. Palik, E. D. & Ghosh, G. *Handbook of optical constants of solids.* (Academic Press, 1998).
55. Cho, C. *et al.* The role of photon recycling in perovskite light-emitting diodes. *Nat. Commun.* **11**, 1–8 (2020).
56. Cho, C. & Greenham, N. C. Computational Study of Dipole Radiation in Re-Absorbing Perovskite Semiconductors for Optoelectronics. *Adv. Sci.* **8**, 2003559 (2021).
57. Park, S. M., Abtahi, A., Boehm, A. M. & Graham, K. R. Surface Ligands for Methylammonium Lead Iodide Films: Surface Coverage, Energetics,



- and Photovoltaic Performance. *ACS Energy Lett.* **5**, 799–806 (2020).
58. Wagstaffe, M. *et al.* An Experimental Investigation of the Adsorption of a Phosphonic Acid on the Anatase TiO<sub>2</sub> (101) Surface. *J. Phys. Chem. C* **120**, 1693–1700 (2016).
  59. Li, F., Zhong, H., Zhao, G., Wang, S. & Liu, G. Adsorption of  $\alpha$ -hydroxyoctyl phosphonic acid to ilmenite/water interface and its application in flotation. *Colloids Surfaces A Physicochem. Eng. Asp.* **490**, 67–73 (2016).
  60. Xuan, T. *et al.* Highly stable CsPbBr<sub>3</sub> quantum dots coated with alkyl phosphate for white light-emitting diodes. *Nanoscale* **9**, 15286–15290 (2017).
  61. Choi, M.-R. *et al.* Soluble self-doped conducting polymer compositions with tunable work function as hole injection/extraction layers in organic optoelectronics. *Angew. Chemie - Int. Ed.* **50**, 6274–6277 (2011).
  62. Jeong, S.-H. *et al.* Universal high work function flexible anode for simplified ITO-free organic and perovskite light-emitting diodes with ultra-high efficiency. *NPG Asia Mater.* **9**, e411 (2017).
  63. Kim, H. *et al.* Proton-transfer-induced 3D/2D hybrid perovskites suppress ion migration and reduce luminance overshoot. *Nat. Commun.* **11**, 3378 (2020).
  64. Pazos-Outon, L. M. *et al.* Photon recycling in lead iodide perovskite solar cells. *Science (80-. ).* **351**, 1430–1433 (2016).
  65. Stranks, S. D., Hoyer, R. L. Z., Di, D., Friend, R. H. & Deschler, F. The Physics of Light Emission in Halide Perovskite Devices. *Adv. Mater.* **31**,



- 1803336 (2019).
66. Song, J. *et al.* Over 30% External Quantum Efficiency Light-Emitting Diodes by Engineering Quantum Dot-Assisted Energy Level Match for Hole Transport Layer. *Adv. Funct. Mater.* **29**, 1808377 (2019).
  67. Dai, X. *et al.* Solution-processed, high-performance light-emitting diodes based on quantum dots. *Nature* **515**, 96–99 (2014).
  68. Woo, S.-J., Kim, J. S. & Lee, T.-W. Characterization of stability and challenges to improve lifetime in perovskite LEDs. *Nat. Photonics* **15**, 630–634 (2021).
  69. Fakharuddin, A. *et al.* Perovskite light-emitting diodes. *Nat. Electron.* **5**, 203–216 (2022).
  70. Han, T.-H. *et al.* A roadmap for the commercialization of perovskite light emitters. *Nat. Rev. Mater.* **0123456789**, (2022).
  71. Back, H. *et al.* Achieving long-term stable perovskite solar cells: Via ion neutralization. *Energy Environ. Sci.* **9**, 1258–1263 (2016).
  72. Back, H. *et al.* Achieving long-term stable perovskite solar cells via ion neutralization. *Energy Environ. Sci.* **9**, 1258–1263 (2016).
  73. FAIRBROT, F. & Frith, C. The Hydration and Hydrolysis of Anhydrous Aluminium Bromide. *J. Chem. Soc.* 2975–2982 (1953).
  74. Zhao, L. *et al.* Redox Chemistry Dominates the Degradation and Decomposition of Metal Halide Perovskite Optoelectronic Devices. *ACS Energy Lett.* **1**, 595–602 (2016).
  75. Vinogradov, N. A. *et al.* Hole doping of graphene supported on Ir(111) by AlBr<sub>3</sub>. *Appl. Phys. Lett.* **102**, (2013).



76. Xiao, X. *et al.* Capacitance–voltage characteristics of perovskite light-emitting diodes: Modeling and implementing on the analysis of carrier behaviors. *Appl. Phys. Lett.* **120**, 243501 (2022).
77. Zhao, L., Lee, K. M., Roh, K., Khan, S. U. Z. & Rand, B. P. Improved Outcoupling Efficiency and Stability of Perovskite Light-Emitting Diodes using Thin Emitting Layers. *Adv. Mater.* **31**, 1805836 (2019).
78. García-Batlle, M. *et al.* Mobile Ion-Driven Modulation of Electronic Conductivity Explains Long-Timescale Electrical Response in Lead Iodide Perovskite Thick Pellets. *ACS Appl. Mater. Interfaces* **13**, 35617–35624 (2021).



## 초록

금속 할라이드 페로브스카이트 재료는 좁은 반치폭과 높은 광발광 효율, 우수한 전하 수송 특성, 색조절의 용이성 등으로 인해 차세대 고색순도 디스플레이 구현을 위한 물질로써 각광받고 있다. 이러한 페로브스카이트 발광체 기반 페로브스카이트 발광 다이오드는 20% 이상의 높은 외부 양자 효율을 보이며 디스플레이 분야에서의 가능성을 보이고 있다. 그러나 페로브스카이트 결정은 근본적으로 약한 이온결정으로 이루어져 있어 열, 수분, 산소, 그리고 광전소자 구동 시에 인가된 전압에 의해 쉽게 열화되며 낮은 안정성을 보이는 문제가 있다. 이로 인해 페로브스카이트 발광 다이오드는 수십 시간 이내의 매우 짧은 수명과 불안정한 소자 거동을 보인다는 한계점이 있어, 페로브스카이트 발광 다이오드의 상용화를 위해서는 페로브스카이트 발광체의 불안정성 극복이 필요하다고 할 수 있다. 본 논문에서는 코어-셸 구조 도입을 통한 안정한 페로브스카이트 발광체의 구현과, 페로브스카이트 발광 다이오드 내에서 일어나는 이온 이동에 의한 열화 메커니즘의 규명에 대한 주제를 다뤘다.

제2장에서는 안정한 2차원 페로브스카이트 구조를 활용한 3차원-2차원 코어-셸 구조의 페로브스카이트 발광체 개발에 대한 내용을 다룬다. 페로브스카이트 전구체 용액 내에서의 양성자 이동 반응을 촉진 시킴으로써 안정한 2차원 페로브스카이트 구조를 합성하고, 이들이 결정화 단계에서 3차원 페로브스카이트를 감싸는 혼합 구조를 형성시킴으로



써 3차원 페로브스카이트 결정의 표면에 위치하는 결함을 억제할 수 있었다. 기존의 3차원 페로브스카이트 구조는 결정 표면의 결함에서 일어나는 전하 소실로 인한 낮은 발광 효율과, 결함에서 일어나는 이온 이동으로 인해 매우 낮은 안정성을 보이는 단점이 있었다. 이러한 한계는 2차원 페로브스카이트 구조로 표면을 안정화시킴으로써 해결되어 보다 높은 발광 효율과 우수한 구동 수명을 보이는 페로브스카이트 발광 다이오드를 구현할 수 있었다. 또한 발광 다이오드 구동시 소자의 불안정한 거동의 원인이 이온 이동에 의한 것이라는 것을 증명했다.

제3장에서는 인시츄 공정을 통한 코어-셸 나노결정 구조의 페로브스카이트 발광체 합성에 대한 내용을 다룬다. 기존에 보고된 3차원 구조, 콜로이드 나노입자 페로브스카이트 구조는 본질적으로 높은 전하 이동도와 높은 전하 구속 효과를 동시에 만족하지 못한다는 한계점이 있었다. 본 연구에서는 페로브스카이트 3차원 다결정 페로브스카이트 박막 표면에 짧은 리간드 처리를 진행함으로써, 수백 나노미터 수준의 큰 결정을 나노입자 수준의 크기로 잘게 쪼개면서도 표면을 짧은 리간드로 감싸는 코어-셸 구조를 형성하였다. 이러한 인시츄 코어-셸 구조는 소량의 짧은 리간드를 사용하여 기존 3차원 구조의 높은 전하 이동도가 유지될 뿐만 아니라, 나노입자의 우수한 전하 구속 효과를 갖는 이상적인 발광 특성을 보였다. 그 결과 페로브스카이트 발광 다이오드로 제작하였을 때에 최대 400,000니트 이상의 휘도, 최대 28.9%의 외부 양자 효율, 100니트의 휘도에서 30,000시간 이상의 예측 구동수명을 보이는 우수



한 소자를 구현할 수 있었다.

제4장에서는 페로브스카이트 발광소자에서 특징적으로 나타나는 급격한 고장 현상에 이온 이동이 미치는 영향과 그 열화 메커니즘에 대한 내용을 다룬다. 앞서 3장에서 다루었던 안정한 코어-셸 나노결정 구조 페로브스카이트와 3차원 다결정 구조 페로브스카이트 기반 발광 다이오드를 활용하여, 열화 단계별 전기적, 광학적, 화학적 특성을 분석함으로써 급격한 고장 현상의 원인을 규명하였다. 특히 페로브스카이트 결정에서 전극을 향해 일어나는 이온 확산, 이온에 의한 금속 전극의 부식, 구동 전압의 증가, 뒤따른 줄열 발생이 이루는 양성 피드백에 의해 가속화되는 소자 열화 메커니즘의 존재를 규명하였다.

주요어: 금속 할라이드 페로브스카이트, 발광 다이오드, 코어/셸 구조, 이온 이동, 안정성, 열화 메커니즘

학번: 2017-27320



# Curriculum Vitae

## *Education & Training*

---

- 2017.03– present    Ph.D course in Department of Materials Science and Engineering, Seoul National University (SNU), Seoul, Korea  
(Advisor: Tae-Woo Lee).
- 2012.03– 2015.02    B.S. in Department of Materials Science and Engineering, POSTECH, Pohang, Korea

## *Honors and Awards*

---

- 2018.02    **Best Poster Presentation Award**  
- 2018 The 25<sup>th</sup> Korean Conference on Semiconductors (KCS 2019)
- 2018.08    **2018 Global Ph.D. Fellowship** (2018 ~ )  
- National Research Foundation of Korea
- 2019.03    **2019 1<sup>st</sup> BK21+ Best Paper Award**  
- BK21+ Seoul National University Materials Division for Educating Creative Global Leaders
- 2020.11    **Best Oral Presentation Award**  
- 2020 Materials Research Society (MRS) Fall Meeting
- 2022.12    **Best Poster Presentation Award**  
- 2022 Materials Research Society (MRS) Fall Meeting
- 2022.12    **Best Ph.D Dissertation Award**  
- Department of Materials Science and Engineering, Seoul National University



## ***Publications***

---

1. C. Wolf, **J. S. Kim**, and T.-W. Lee\*, "Structural and Thermal Disorder of Solution-Processed  $\text{CH}_3\text{NH}_3\text{PbBr}_3$  Hybrid Perovskite Thin Films", **ACS Appl. Mater. Interfaces**, 2017, 9(12), 10344-10348

SCI Impact Factor = 10.383

2. H. Cho, C. Wolf, **J. S. Kim**, H.-J. Yun, J.-S. Bae, H. Kim, J.-M. Heo, S. Ahn, T.-W. Lee\*, "High-Efficiency Solution-Processed Inorganic Metal Halide Perovskite Light-Emitting Diodes", **Adv. Mater.**, 2017, 29(31), 1700579

SCI Impact Factor = 32.086

3. M.-H. Park<sup>+</sup>, S.-H. Jeong<sup>+</sup>, H.-K. Seo<sup>+</sup>, C. Wolf, Y.-H. Kim, H. Kim, J. Byun, **J. S. Kim**, H. Cho, T.-W. Lee\*, "Unravelling Additive-based Nanocrystal Pinning for High Efficiency Organic-Inorganic Halide Perovskite Light-Emitting Diodes", **Nano Energy**, 2017, 42, 157–165

SCI Impact Factor = 19.069

4. H. Cho, **J. S. Kim**, Y.-H. Kim, T.-W. Lee\*, "Influence of A-site cation on the thermal stability of metal halide perovskite polycrystalline films", **Journal of Information Display**, 2018, 19, 53–60

SCI Impact Factor = 4.237

5. H. Cho<sup>+</sup>, **J. S. Kim<sup>+</sup> (+: equally contributed to this work)**, C. Wolf, Y.-



H. Kim, H. J. Yun, S.-H. Jeong, A. Sadhanala, V. Venugopalan, J. Choi, C.-L. Lee, R. H. Friend, T.-W. Lee\*, "High-Efficiency Polycrystalline Perovskite Light-Emitting Diodes based on Mixed Cations", **ACS Nano**, 2018, 12 (3), 2883-2892

SCI Impact Factor = 18.027

6. Y. Park, C. Park, **J. S. Kim**, T. K. Ahn, H. S. Lim, T.-W. Lee\*, W. Kwon\*, "Highly Luminescent Organic Nanorods from Air Oxidation of para-Substituted Anilines for Freestanding Deep-Red Color Filters", **Adv. Optical Mater.**, 2018, 1800577

SCI Impact Factor = 10.05

7. **J. S. Kim**, H. Cho, C. Wolf, H. J. Yun, J. Heo, T.-W. Lee\*, "Increased Luminescent Efficiency of Perovskite Light Emitting Diodes Based on Modified Two-Step Deposition Method Providing Gradient Concentration", **APL Mater.** 6, 111101 (2018)

SCI Impact Factor = 6.635

8. Y.-H. Kim, **J. S. Kim**, T.-W. Lee\*, "Strategies to Improve Luminescence Efficiency of Metal-Halide Perovskite and Light-Emitting Diodes", **Adv. Mater.**, 2018, 1804595

SCI Impact Factor = 32.086

9. H.-D. Lee<sup>+</sup>, H. Kim<sup>+</sup>, H. Cho<sup>+</sup>, W. Cha, YS Hong, Y.-H. Kim, A Sadhanala, V. Venugopalan, **J. S. Kim**, J. W. Choi, C.-L. Lee, D Kim, H. Yang, T.-W.



Lee\*, "Efficient Ruddlesden-Popper Perovskite Light-Emitting Diodes with Randomly-Oriented Nanocrystals", **Adv. Funct. Mater.**, 2019, e1901225 (Frontispiece)

SCI Impact Factor = 19.924

10. M.-H. Park<sup>+</sup>, **J. S. Kim<sup>+</sup> (+: equally contributed to this work)**, J.-M. Heo<sup>+</sup>, S. Ahn, S.-H. Jeong, T.-W. Lee\*, "Boosting Efficiency in Polycrystalline Metal Halide Perovskite Light-Emitting Diodes", **ACS Energy Lett.** 2019, 4, 1134-1149

SCI Impact Factor = 23.991

11. H. M. Jang, **J. S. Kim**, J.-M. Heo, T.-W. Lee\*, "Enhancing photoluminescence quantum efficiency of metal halide perovskites by examining luminescence-limiting factors", **APL Mater.**, 2020, 8, 020904

SCI Impact Factor = 6.635

12. H. Kim<sup>+</sup>, **J. S. Kim<sup>+</sup> (+: equally contributed to this work)**, J.-M. Heo<sup>+</sup>, M. Pei, I.-H. Park, Z. Liu, H. J. Yun, M.-H. Park, S.-H. Jeong, Y.-H. Kim, J. Park, O. Emad, S. Nagane, A. Sadhanala, L. Zhang, J. J. Kweon, S. K. Lee, H. Yang, H. M. Jang, R. H. Friend, K. P. Loh, M. K. Nazeeruddin, N.-G. Park, T.-W. Lee\*, "Proton-Transfer-Induced 3D/2D Hybrid Perovskites Suppress Ion Migration and Extremely Reduce Luminance Overshoot",

**Nat. Commun.** 2020, 11, 3378

SCI Impact Factor = 17.694



13. S.-H. Jeong, J. Park, T.-H. Han, F. Zhang, K. Zhu, **J. S. Kim**, M.-H. Park, M. O. Reese, S. Yoo, T.-W. Lee\*, “Characterizing the Efficiency of Perovskite Solar Cells and Light-Emitting Diodes”, **Joule**, 2020, 4 (6), 1206-1235  
SCI Impact Factor = 46.048

14. H. Zhou, J. Park, Y. Lee, J.-M. Park, J.-H. Kim, **J. S. Kim**, H.-D. Lee, S. H. Jo, X. Cai, L. Li, X. Sheng, H. J. Yun, J.-W. Park, J.-Y. Sun, and T.-W. Lee\*, “Water Passivation of Perovskite Nanocrystals Enables Air-Stable Intrinsically Stretchable Color-Conversion Layers for Stretchable Displays”, **Adv. Mater.** 2020, 32, 37, 2001989  
SCI Impact Factor = 32.086

15. H. Kang, S.-R. Choi, Y.-H. Kim, **J. S. Kim**, S. Kim, B.-S. An, C.-W. Yang, J.-M. Myoung, T.-W. Lee, J.-G. Kim\*, and J. H. Cho\*, “Electroplated Silver–Nickel Core–Shell Nanowire Network Electrodes for Highly Efficient Perovskite Nanoparticle Light-Emitting Diodes”, **ACS Appl. Mater. Interfaces**, 2020, 12, 35, 39479–39486  
SCI Impact Factor = 10.383

16. S. Ahn<sup>+</sup>, Y.-H. Kim<sup>+</sup>, S. Kim<sup>+</sup>, J. Park, N. Li, J.-M. Heo, **J. S. Kim**, D. J. Kim, B. H. Hong, J. Y. Lee, and T.-W. Lee\*, "Synergistic molecular engineering of hole-injecting conducting polymers overcomes luminescence quenching in perovskite light-emitting diodes", **Adv. Optical. Mater.** 2021, 9(18), 100646



SCI Impact Factor = 10.05

17. S.-J. Woo, **J. S. Kim** and T.-W. Lee\*, "Characterization of stability and challenges to improve lifetime in perovskite LEDs", **Nat. Photon.**, 15, 630–634 (2021)

SCI Impact Factor = 39.728

18. Y.-H. Kim, S. Ahn, **J. S. Kim** and T.-W. Lee\*, “Halide Perovskite Light-Emitting Diodes” in Multifunctional Organic–Inorganic Halide Perovskite: Applications in Solar Cells, Light-Emitting Diodes, and Resistive Memory, Jenny Stanford Publishing Pte. Ltd. (2021)

19. H. Kang<sup>+</sup>, **J. S. Kim<sup>+</sup>(<sup>+</sup>: equally contributed to this work)**, S.-R. Choi, Y.-H. Kim, D. H. Kim, J.-G. Kim, T.-W. Lee, J. H. Cho\* “Electroplated Core–Shell Nanowire Network Electrodes for Highly Efficient Organic Light-Emitting Diodes”, **Nano Converg.**, 9, 1 (2022)

SCI Impact Factor = 10.038

20. Y.-H. Kim<sup>+</sup>, J. Park<sup>+</sup>, S. Kim<sup>+</sup>, **J. S. Kim**, H. Xu, S.-H. Jeong, B. Hu, and T.-W. Lee\*, “Exploiting the full advantages of colloidal perovskite nanocrystals for large-area efficient light-emitting”, **Nat. Nanotech.** 17, 590-597 (2022)

SCI Impact Factor = 40.523



21. J.-M. Heo<sup>+</sup>, H. Cho<sup>+</sup>, S.-C. Lee<sup>+</sup>, M.-H. Park, **J. S. Kim**, H. Kim, J. Park, Y.-H. Kim, E. Yoon, S. Ahn, S.-J. Kwon, T.-W. Lee\*, “Bright Lead-Free Inorganic CsSnBr<sub>3</sub> Perovskite Light-Emitting Diodes”, **ACS Energy Lett.** 7, 8, 2807-2815 (2022)  
SCI Impact Factor = 23.991

21. **J. S. Kim**<sup>+</sup>, J.-M. Heo<sup>+</sup>, G.-S. Park, S.-J. Woo, H. J. Yun, C. Cho, D.-H. Kim, J.-W. Park, S.-C. Lee, S.-H. Park, E. Yoon, N. C. Greenham, and T.-W. Lee\*, “Ultra-Bright, Efficient and Stable Perovskite Light-Emitting Diodes”, **Nature**, 611, 688-694 (2022)  
SCI Impact Factor = 69.504



## ***Conference Presentations (Poster)***

---

1. **J. S. Kim**, C. Wolf, H. Cho, and T.-W. Lee\*, "Highly Efficient and Stable Perovskite Light-Emitting Diodes Using Amino Acid Passivation", International Conference on Electronic Materials and Nanotechnology for Green Environment (ENGE 2016), Ramada Plaza Hotel, Jeju, Korea, November 6-9, 2016 (Poster).

2. **J. S. Kim**, H. Cho, and T.-W. Lee\*, "Defect Passivation of Perovskite Light-Emitting Diodes with Improved Device Efficiency and Operating Stability", The 25th Korean Conference on Semiconductors (KCS 2018), Highone Resort Convention Hotel, Kangwondo, Korea, February 5 –7, 2018 (Poster).

3. **J. S. Kim**, H. Cho, and T.-W. Lee\*, "Efficient and Stable Perovskite Light-Emitting Diodes Using Defect Passivation by Amine Additives", 2018 MRS Spring Meeting & Exhibit, Phoenix, Arizona, April 2-6, 2018 (Poster).

4. **J. S. Kim**, H. Cho, C. Wolf, H. J. Yun, J.-M. Heo, and Tae-Woo Lee\*, "Increased luminescent efficiency of perovskite light emitting diodes based on modified two-step deposition method providing gradient concentration", 2019 A3 Joint Symposium, Atami, Japan, Jan. 18-20, 2019 (Poster).

5. **J. S. Kim**, H. Cho, C. Wolf, H. J. Yun, J.-M. Heo, and Tae-Woo Lee\*, "Modified Sequential Deposition Method Providing Gradient Concentration for Efficient Perovskite Light Emitters", The 26th Korean Conference on



Semiconductors (KCS 2019), Wellhillipark Convention Hotel, Kangwondo, Korea, February 13-15, 2019 (Poster).

6. **J. S. Kim**<sup>+</sup>, J.-M. Heo<sup>+</sup>, G.-S. Park, S.-J. Woo, H. J. Yun, C. Cho, D.-H. Kim, J.-W. Park, S.-C. Lee, S.-H. Park, E. Yoon, N. C. Greenham, and T.-W. Lee\*, “Ultra-Bright, Efficient and Stable Perovskite Light-Emitting Diodes”, 2022 MRS Spring Meeting & Exhibit, Boston, Massachusetts, November 27-December 2, 2022 (Poster).



## ***Conference Presentations (Oral)***

---

1. **J. S. Kim**, H. Kim, J.-M. Heo, and T.-W. Lee\*, "3D/2D Hybrid Perovskites Suppress Ion Migration and Extremely Reduce Luminance Overshoot", 2019 MRS Fall Meeting & Exhibit, Boston, Massachusetts, December 1-6, 2019 (Oral).

2. H. Kim <sup>+</sup>, **J. S. Kim<sup>+</sup> (+: equally contributed to this work)**, J.-M. Heo<sup>+</sup>, and T.-W. Lee\*, "Overcoming instability of metal halide perovskite emitters and their display applications", SPIE Optics + photonics 2020, August 23-27, 2020 (Oral).

3. **J. S. Kim**, H. Kim, J.-M. Heo, M.-H. Park, T.-W. Lee\*, "Core/Shell Structured Metal Halide Perovskites for High-Efficiency Light-Emitting Diodes", nanoGe Fall Meeting 2020, October 19-23, 2020 (Oral).

4. H. Kim <sup>+</sup>, **J. S. Kim<sup>+</sup> (+: equally contributed to this work)**, J.-M. Heo<sup>+</sup>, and T.-W. Lee\*, "Proton-Transfer-Induced 3D-2D Hybrid Perovskite for Stable Light-Emitting Diodes", ACOE 2020, November 8-10, 2020 (Poster).

5. H. Kim <sup>+</sup>, **J. S. Kim<sup>+</sup> (+: equally contributed to this work)**, J.-M. Heo<sup>+</sup>, M. Pei, I.-H. Park, Z. Liu, H. J. Yun, M.-H. Park, S.-H. Jeong, Y.-H. Kim, J. Park, O. Emad, S. Nagane, A. Sadhanala, L. Zhang, J. J. Kweon, S. K. Lee, H. Yang, H. M. Jang, R. H. Friend, K. P. Loh, M. K. Nazeeruddin, N.-G. Park, T.-W. Lee\*, "Proton-Transfer-Induced 3D/2D Hybrid Perovskites Suppress



Ion Migration and Extremely Reduce Luminance Overshoot”,  
2020 MRS Fall Meeting & Exhibit, Boston, Massachusetts, November 27 -  
December 4, 2020 (Oral).



## ***Patents (Domestic)***

---

### **Application**

1. 이태우, 조승현, 김주성, 주환우, '압전성 및 발광성이 동기화된 유기 하이브리드 페로브스카이트 결정 박막, 이의 제조방법 및 이를 포함하는 소자', Application No.: 1020180058327, (2018.05.23).
2. 이태우, 김주성, 김호범, '양성자 이동 반응에 의해 유도된 다차원 결정 구조의 페로브스카이트 필름, 이의 제조방법 및 이를 발광층으로 포함하는 발광소자', Application No.: 1020180163461, (2018.12.17).
3. 이태우, 김주성, '점진적인 유사-2차원 페로브스카이트 필름의 제조 방법 및 이로부터 제조된 유사-2차원 페로브스카이트 필름을 발광층으로 포함하는 발광소자', Application No.: 1020180163582, (2018.12.17).
4. 이태우, 김주성, 권성주, 안소영, 김호범, '금속 할라이드 페로브스카이트 발광소자 및 이의 제조방법', Application No.: 1020190168360, (2019.12.16).
5. 이태우, 김주성, 김성진, 허정민, 김영훈, 박진우, '중형 1가 유기 양이온을 이용하여 결점이 제어된 금속 할라이드 페로브스카이트 발광 입자', Application No.: 1020190168361, (2019.12.16).
6. 이태우, 김주성, 권성주, 안소영, 김호범, '금속 할라이드 페로브스카이트 발광소자 및 이의 제조방법', Application No.: 1020190168480, (2019.12.17).
7. 이태우, 김주성, 유승협, 박재혁, '페로브스카이트 발광 다이오드의 효율 및 발광특성 측정 장치', Application No.: 1020200177406,



(2020.12.17).

8. 이태우, 김주성, 유승협, 박재혁, '발광 소자의 발광특성 측정 장치 및 이의 측정 방법', Application No.: 1020210182111, (2021.12.17).

### **Registration**

1. 이태우, 김주성, 권성주, 안소영, 김호범, '금속 할라이드 페로브스카이트 발광소자 및 이의 제조방법', Registration No.: 10-2259782, (2021-05-27).



## ***Patents (International)***

1. 이태우, 김주성, 김성진, 허정민, 김영훈, 박진우, 'DEFECT SUPPRESSED METAL HALIDE PEROVSKITE LIGHT-EMITTING MATERIAL AND LIGHT-EMITTING DIODE COMPRISING THE SAME', Application No.: US 17/268,462, (2021.02.13).
2. 이태우, 김주성, 권성주, 안소영, 김호범, 'METAL HALIDE PEROVSKITE LIGHT EMITTING DEVICE AND METHOD FOR MANUFACTURING SAME', Application No.: US 17/415,718, (2021.02.17).
3. 이태우, 김주성, 권성주, 안소영, 김호범, 'Perovskite film having multi-dimensional crystalline structure induced by proton transfer, preparation method thereof and light-emitting device comprising the same as light-emitting layer', Application No.: JP 2021-535112, (2021.06.17).

## **PCT**

1. 이태우, 김주성, 권성주, 안소영, 김호범, 'Perovskite film having multi-dimensional crystalline structure induced by proton transfer, preparation method thereof and light-emitting device comprising the same as light-emitting layer', Application No.: PCT/KR2019/017914, (2019.12.17).
2. 이태우, 김주성, 김성진, 허정민, 김영훈, 박진우, 'Defect suppressed metal halide perovskite light-emitting material and light-emitting diode comprising the same', Application No.: PCT/KR2019/018289, (2019.12.23).